Reviews in Mineralogy & Geochemistry
Vol. 82 pp. XXX-XXX, 2017

Iron Isotope Systematics

Nicolas Dauphas

Origins Lab
Department of the Geophysical Sciences and Enrico Fermi Institute
The University of Chicago
5734 South Ellis Avenue
Chicago IL 60637
USA

dauphas@uchicago.edu

Seth G. John

University of Southern California
Department of Earth Science
Marine Trace Element Laboratory
3651 Trousdale Pkwy
Los Angeles, CA 90089
USA

sethjohn@usc.edu

Olivier Rouxel

IFREMER
Department of Physical Resources and Deep-Sea Ecosystems
Plouzané
29280
France
University of Hawaii
Department of Oceanography
1000 Pope Road
Honolulu, HI 96822
USA

orouxel@hawaii.edu

INTRODUCTION

Iron is a ubiquitous element with a rich (i.e., complex) chemical behavior. It possesses three oxidation states, metallic iron (Fe^0), ferrous iron (Fe^{2+}) and ferric iron (Fe^{3+}). The distribution of these oxidation states is markedly stratified in the Earth.

- Metallic iron is primarily present in the core, where it is alloyed with Ni, Co, and light elements such as S, Si or O. Some metallic iron may be present at depth in the mantle because Fe^{2+} in bridgmanite can disproportionate into Fe^{3+} and Fe^0 (Frost et al. 2004). Natural metallic iron also exists at the surface of the Earth in rare occurrences in the form of meteorite falls, metallic iron produced by reduction of lavas through interaction with coal sediments as in Disko Island (Greenland), and Josephinite (awaruite) produced by serpentinization reaction in peridotites.

1529-6466/17/0082-0011$10.00 http://dx.doi.org/10.2138/rmg.2017.82.11

- The main repository of ferrous iron is the mantle, where it is present in two spin states (the manner in which electrons fill the orbitals). At low pressure, mantle minerals contain iron in a high spin electronic state. Under the high-pressure conditions of the lower mantle, iron transitions into a low-spin electronic state (Badro et al. 2003; Lin et al. 2013). This spin transition influences the physical, chemical, and rheological properties of minerals.
- The lower mantle presumably contains significant Fe^{3+} produced by Fe^{2+} disproportionation (Frost et al. 2004). At the pressures relevant to the upper mantle, iron is not disproportionated, yet Fe^{3+} represents ~3% of total iron (Canil et al. 1994). Ferric iron is much more common in surface oxygenated environments and in crustal rocks due to the presence of an oxygen-rich atmosphere. Iron is an essential micronutrient and the low solubility of Fe^{3+} in seawater has a significant influence on biomass productivity in the modern oceans (Falkowski 1997; Mills et al. 2004).

Planetary objects other than Earth show similar stratification, including Mars, which has a metallic iron-rich core, a ferrous iron-rich mantle, and a ferric iron-rich surface, giving Mars its red color through the presence of nano-crystalline hematite. Many questions pertaining to the establishment and implications of such stratification remain unanswered, such as what were the P–T–fO_2 conditions that prevailed during core formation, how did the terrestrial mantle get oxidized, what was the timing of Earth's surface oxygenation, how did Earth's atmosphere become oxic, when did iron-based anoxygenic photosynthesis and dissimilatory iron reduction (a form of respiration) begin, and how did these inventions influence the global geochemical cycle of iron? Progress towards answering these fundamental questions and other related ones has been slow for lack of proxies to unravel the riddles of iron's complex cosmochemical, geochemical and biochemical behaviors.

The situation changed drastically over the past 15 years with the bloom of iron isotope geochemistry. Iron possesses four stable isotopes, ^{54}Fe, ^{56}Fe, ^{57}Fe, and ^{58}Fe, which represent 5.845, 91.754, 2.1191, and 0.2919 atom% respectively of the total (Berglund and Wieser 2011). The isotopic composition of iron is usually reported as $\delta^{56}Fe$, which is the deviation in part per mil of the $^{56}Fe/^{54}Fe$ ratio relative to the IRMM−014 reference standard. The $\delta^{58}Fe$ value is almost never reported because ^{58}Fe is a rare isotope and measurements have shown that it was related to $\delta^{56}Fe$ by mass-dependent fractionation (Dauphas et al. 2008; Tang and Dauphas 2012), except in magnetite produced by some magnetotactic bacteria (Amor et al. 2016). The $\delta^{57}Fe$ value is often reported because it allows one to ensure that there are no unresolved analytical artifacts. As with $\delta^{58}Fe$, it is related to $\delta^{56}Fe$ through mass-dependent fractionation. In the present chapter, we will thus focus on $\delta^{56}Fe$, from which $\delta^{57}Fe$ and $\delta^{58}Fe$ can be derived ($\delta^{57}Fe \approx 1.5 \times \delta^{56}Fe$ and $\delta^{58}Fe \approx 2 \times \delta^{56}Fe$).

Before the advent of MC-ICPMS (Multi Collector Inductively Coupled Plasma Mass Spectrometry) (Maréchal et al. 1999), the method of choice for measuring the isotopic composition of iron was TIMS (Völkening and Papanastassiou 1989; Beard and Johnson 1999; Johnson and Beard 1999), which stands for Thermal Ionization Mass Spectrometry. TIMS instruments have a relatively small bias but that bias is highly unstable and cannot be easily corrected for. Better precision and reproducibility was achieved by MC-ICPMS, which are affected by a large instrumental mass bias but this bias is more stable than in TIMS (Belshaw et al. 2000; Dauphas et al. 2009a; Millet et al. 2012). The relative ease with which the isotopic composition of iron can now be measured by MC-ICPMS has contributed to its widespread use to trace geochemical and biochemical processes involving iron.

Several reviews have been published over the past 15 years covering all aspects of iron isotope geochemistry (Beard and Johnson 2004a; Johnson et al. 2004, 2008a; Dauphas and Rouxel 2006; Anbar and Rouxel 2007). Dauphas and Rouxel (2006) reviewed the literature available in the field up to that date and made an effort to cite every single paper published

on iron isotope geochemistry before 2006. In the present review, we will therefore put more emphasis on developments in iron isotope geochemistry that took place over the past decade, while still highlighting the important discoveries made before that time. The most important developments in the past 10 years include the recognition that igneous rocks and minerals can display iron isotopic variations, a better understanding of the ancient iron marine cycle, and the first extensive use of iron isotope measurements in modern seawater to better understand the modern marine iron cycle. The past decade has also seen a large increase in the number of laboratory experiments aimed at determining equilibrium and kinetic fractionation factors needed to interpret iron isotope variations in natural samples.

METHODOLOGY

The range of iron isotopic variations in natural samples is a few permil (from ~−4 to +2‰; Dauphas and Rouxel 2006). The method of TIMS, which gives a precision of approximately ±0.2‰ on δ^{56}Fe (see Eqn. 1 for a definition of this notation), opened the field of iron isotope systematics to investigation (Beard and Johnson 1999; Beard et al. 1999; Fantle and DePaolo 2004). Subsequent work by MC-ICPMS, which can reach a precision of ±0.03‰ (Dauphas et al. 2009a; Millet et al. 2012), proved that there were significant iron isotope variations hidden in the ±0.2 ‰ uncertainty of early TIMS measurements. Another advantage of MC-ICPMS relative to TIMS is the high sample throughput, as it is possible to measure up to a few tens of samples in a day, depending on the precision needed. MC-ICPMS has thus been established as the method of choice to measure the isotopic composition of iron.

Iron isotope variations are usually defined using the δ^{56}Fe notation as,

$$\delta^{56}\mathrm{Fe} = \left[\frac{\left({}^{56}\mathrm{Fe} / {}^{54}\mathrm{Fe} \right)_{\mathrm{sample}}}{\left({}^{56}\mathrm{Fe} / {}^{54}\mathrm{Fe} \right)_{\mathrm{standard}}} - 1 \right] \times 10^{3} \quad (1)$$

where the standard is usually IRMM−014; a metallic iron standard distributed by the Institute for Reference Materials and Methods. Although this is a synthetic standard, Craddock and Dauphas (2011a) showed that it has an isotopic composition indistinguishable from chondrites, all of which have a relatively uniform iron isotopic composition regardless of their group or petrologic type, defining a mean value of -0.005 ± 0.006‰ relative to IRMM−014. Early on, the isotopic composition of iron was defined relative to the average of terrestrial igneous rocks (Beard and Johnson 1999) but it was subsequently shown that those rocks displayed significant iron isotopic variations and are not necessarily representative of the composition of the terrestrial mantle (Williams et al. 2004a,b; Schoenberg and von Blanckenburg 2006; Weyer and Ionov 2007; Teng et al. 2008; Dauphas et al. 2009b; Teng et al. 2013), which may have a chondritic composition. Most iron isotope data published in the literature now adopt IRMM−014 as reference standard. An issue is that the stock of IRMM−014 has been exhausted and the Institute for Reference Materials and Measurements no longer sells this standard. Craddock and Dauphas (2011a) showed that IRMM-524a, a reference material for neutron dosimetry, has the same Fe isotopic composition as IRMM−014, which is understandable because IRMM−014 was prepared from IRMM-524a. Quoting the IRMM−014 certificate, "IRMM−014 was made up from the neutron dosimetry reference material EC-NRM 524. The cubes were prepared by melting pieces of foil, rolling into a plate and cutting with a diamond wheel. The wires were taken as such from the EC-NRM 524 stock." Until the shortage of IRMM−014 is addressed, we recommend that IRMM-524a be used for normalization in the lab but that δ^{56}Fe values still be expressed relative to IRMM−014.

Rocks and solid samples

Iron is a major rock-forming element whose chemical separation from rock matrices is relatively straightforward (Dauphas et al. 2004a, 2009a). Because iron is so abundant, blanks are usually not an issue provided that clean fluoropolymer vessels and distilled reagents are used. We describe below the measurement protocol as is used at the University of Chicago (Dauphas et al. 2009a) and elsewhere (e.g., WHOI, Ifremer) to measure rock samples. The procedure usually starts by powdering samples to make sure that the material that is analyzed is representative of the bulk rock. A powder aliquot is then sampled (typically up to a few tens of mg) and transferred in a Teflon beaker to be digested by acids, whose composition depends on the nature of the sample studied. The samples are usually cycled through several evaporations to dryness and acid dissolutions to ensure that insoluble fluorides are eliminated and that iron is present in its 3+ oxidation state. The second aspect is usually achieved by using oxidizing reagents in the digestion, such as nitric acid, perchloric acid, hydrogen peroxide, or a combination thereof. The sample is then taken up in acid for passage on the chromatographic column.

All separation chemistries involve anion exchange resins. The nature of the resin can vary, with AG1-X8 200–400 mesh being the most commonly used (Dauphas et al. 2009a) and AG-MP1 coming second when other transition metals such as Cu and Zn have to be recovered for independent isotopic analysis (Liu et al. 2014). The latter resin is used most often with aqueous fluids (Borrok et al. 2007; Conway et al. 2013). The most straightforward chemistry is that based on AG1-X8, which is a rapid and cost-saving stick–non-stick chemical procedure. Its main drawback is that Cu is not separated from Fe, although separation can be achieved by running more matrix-eluting acid through the column (Tang and Dauphas 2012; Sossi et al. 2015). The sample is usually loaded onto the column in concentrated HCl (e.g., 6 M HCl). In that acid, Fe^{3+} is strongly bound to the resin while most of the matrix, except Cu and Mo, is eluted (Strelow 1980). Sometimes H_2O_2 is added to HCl to ensure that iron is not reduced by reaction with the resin, although this may be unnecessary as protocols not involving H_2O_2 still achieve excellent yields and give $\delta^{56}Fe$ values similar to those measured by protocols involving H_2O_2, provided that iron is all oxidized into Fe^{3+} before passage on the column. Iron is then recovered by running dilute HCl (e.g., 0.4 M HCl). The chromatography protocol can be repeated once or more to ensure that a sufficient purity level is achieved. Measurements by MC-ICPMS impose tight constraints on the level of purity required. If the measurements are done by standard-sample bracketing, then two passages through column chemistry may be needed to achieve the highest precision and accuracy (Dauphas et al. 2009a). Double-spike measurements are more forgiving for the presence of matrix elements that can influence instrumental mass bias, as long as there are no direct isobaric interferences on iron isotopes (Millet et al. 2012)

One difficulty intrinsic to iron isotopic analyses by MC-ICPMS is the presence of oxygen and nitrogen argide interferences on iron isotopes. For example, $^{40}Ar^{14}N^+$ can interfere with $^{54}Fe^+$, $^{40}Ar^{16}O^+$ can interfere with $^{56}Fe^+$, and $^{40}Ar^{16}O^1H^+$ can interfere with $^{57}Fe^+$. Several instrumental strategies have been used to deal with these important isobaric interferences: brute force measurements with high iron concentrations (Belshaw et al. 2000), collision cell technology (Beard et al. 2003a; Rouxel et al. 2003; Dauphas et al. 2004a), cold plasma (Kehm et al. 2003), and high-resolution (Weyer and Schwieters 2003; Dauphas et al. 2009a). The second one was implemented on the Micromass Isoprobe and involved filling a hexapole collision cell on the ion beam path with Ar and H_2. That collision cell plays two roles. One is to thermalize the incoming ions, so that their energy dispersion is reduced; the hexapole collision cell plays the role of an energy focusing ion optics component. The second role is to break down and stop molecular ions, so that argide interferences can be reduced to a level that is acceptable for iron isotopic analysis. The Isoprobe and its collision cell have largely been phased out and replaced by high-resolution instruments that partly separate argide interferences from the iron isotope peaks. Those instruments are the Nu Plasma 1700 (a.k.a. Big Nu), Nu Plasma II, and Neptune Plus. The

Nu Plasma 1700 is a large geometry instrument equipped with a large magnet that can achieve high-resolution while maintaining high transmission (Williams et al. 2005). This is seldom used in iron isotope geochemistry; the Nu Plasma II and Neptune Plus are the workhorses of iron stable isotope labs around the world. The discussion hereafter therefore focuses on the operation of those two instruments. The masses of ArN, ArO, and ArOH are sufficiently different from those of Fe isotopes that they can be separated using pseudo medium and high mass resolutions (Weyer and Schwieters 2003; Dauphas et al. 2009a). The word pseudo is used because the interfering isobars are not completely resolved but instead show up as flat top peak shoulders (Fig. 1). A significant difficulty with these measurements is that the width of the flat top peak shoulder is relatively narrow, so high stability is needed for the magnetic field and acceleration voltage. Those are highly sensitive to the temperature of the room, which must be maintained constant. The difficulty is exacerbated when the resolution slit deteriorates, so that the mass resolution decreases and the width of the flat top peak shoulder decreases.

The samples dissolved in dilute nitric acid (e.g., 0.3 or 0.45 M) are introduced into the mass spectrometer using either a desolvating nebulizer like the Apex (ESI) or Aridus II (Cetac), or a standard spray chamber most often made of quartz. Desolvating nebulizers have two advantages; they can significantly increase the overall transmission efficiency by increasing the fraction of atoms in solution that make it into the torch, and they also drastically reduce ArN, ArO, and ArOH peaks by drying down the aerosols and removing the solvent that carries N, O, and H (in the forms of H_2O and HNO_3). The standard quartz spray chamber is less efficient (some aerosols are lost by collision with the walls of the spray chamber) and leads to much higher argide peaks but instrumental mass bias is more stable in a wet plasma than when a desolvating nebulizer is used and wash-out time between samples is also smaller. For standard-sample-bracketing measurements of samples that are relatively rich in iron, the quartz spray chamber gives iron isotopic results that are more precise than when a desolvating nebulizer is used (Dauphas et al. 2009a). The desolvating nebulizer may be better suited for double-spike measurements (Millet et al. 2012) or measurements of low iron concentration samples.

The most commonly used technique for iron isotopic analyses is known as sample-standard-bracketing (SSB). It relies on the fact that while instrumental mass bias (i.e., departure between measured and true ratios) in MC-ICPMS is large, it is relatively stable, so that bracketing sample measurements by standard measurements of known compositions

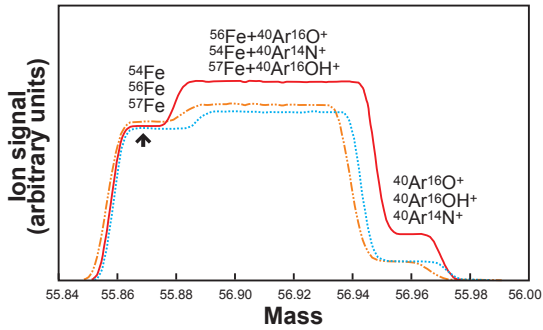

Figure 1. Peak scans of 54, 56, and 57 masses. The measurements were made on a Thermo Scientific Neptune at the University of Chicago. Iron was introduced into the mass spectrometer using the SIS stable introduction system (a dual cyclonic-Scott type spray chamber) and the measurements were made in medium resolution ($m=\Delta m \approx 4000$), where Δm is taken on the peak side between 5 and 95% peak height). The iron concentration was adjusted so that both Fe^+ ions and argide interferences are visible. Iron isotope measurements are performed on the left flat-topped peak shoulders (indicated with an arrow). Iron–58, which is seldom used or reported is not shown.

can correct the measurements for drift in instrumental mass bias. The simplest SSB scheme and the one that seems to give the most reliable results consists in bracketing the sample measurement by two standard measurements in a sequence STD1, SMP_1, STD_2, SMP_2, STD_3, $SMP_3 \ldots SMP_n$, STD_{n+1}. The i^{th} measured $\delta^{56}Fe$ value is simply given by,

$$\delta^{56}Fe_i = \left[\frac{\left({}^{56}Fe / {}^{54}Fe \right)_{SMP,i}}{0.5\left({}^{56}Fe / {}^{54}Fe \right)_{STD,i} + 0.5\left({}^{56}Fe / {}^{54}Fe \right)_{STD,i+1}} - 1 \right] \times 10^3 \quad (2)$$

One could interpolate over more standards using Lagrangian interpolation. However, our experience is that this leads to more noise and simple SSB seems to be the bracketing scheme that gives the best results. The SSB technique has no safeguard to mitigate the influence of matrix elements remaining in solution or other artifacts arising from differences in the composition of the sample and bracketing standards. To achieve the most precise and accurate results, it is important to ensure that (i) iron is well purified, which can involve two passages on ion chromatography columns, (ii) the sample and standard concentrations are well matched, ideally within 5%, and (iii) the acid molarities of the sample and standard solutions are the same, which is most easily achieved by using the same solution to dissolve the standard and purified samples (Dauphas et al. 2009a).

Another approach derived from the SSB technique is the Cu or Ni doping technique (Poitrasson and Freydier 2005; Schoenberg and von Blanckenburg 2005). Copper is more difficult to separate from Fe than Ni, so we will focus below on Ni doping. In this approach, Ni is added to both the sample and standards and the ratio of two Ni isotopes is measured (Poitrasson and Freydier 2005; Rouxel et al. 2005). Iron–58 cannot be analyzed because it has a direct interference from ^{58}Ni. The collector arrays usually allow one to analyze the Ni isotopic ratio $^{62}Ni/^{60}Ni$ (or $^{61}Ni/^{60}Ni$), which we note R_{Ni}. One assumes that the mass fractionation follows the exponential law, $r_{2/1} = R_{2/1}\left(m_2 / m_1\right)^{\beta}$, where $r_{2/1}$ and $R_{2/1}$ are the measured and true ratios of isotopes 2 and 1. One can assume a fixed value for the isotopic ratio of the doping Ni solution and calculate the β-exponent of the exponential mass fractionation law given above,

$$\beta_{Ni} = \ln\left[\left({}^{62}Ni / {}^{60}Ni \right)_{measured} / \left({}^{62}Ni / {}^{60}Ni \right)_{reference} \right] / \ln\left(M_{{}^{62}Ni} / M_{{}^{60}Ni} \right) \quad (3)$$

The iron isotopic composition corrected for this instrumental mass fractionation is denoted with a * superscript and calculated as follows,

$$\left({}^{56}Fe / {}^{54}Fe \right)^{*}_{measured} = \left(\frac{{}^{56}Fe}{{}^{54}Fe} \right)_{measured} \left(M_{{}^{56}Fe} / M_{{}^{54}Fe} \right)^{\frac{\ln\left[\left({}^{62}Ni / {}^{60}Ni \right)_{reference} / \left({}^{62}Ni / {}^{60}Ni \right)_{measured} \right]}{\ln\left(M_{{}^{62}Ni} / M_{{}^{60}Ni} \right)}} \quad (4)$$

The corrected iron isotopic ratio is then used in the regular SSB equation given above. The advantage of Ni doping is that it can partially mitigate the influence of matrix elements remaining in the solution that can change the instrumental mass bias. It can also potentially better correct for instrumental drift. Its drawbacks are that ^{58}Fe cannot be measured and the method is sensitive to isobaric interferences on Ni isotopes in addition to Fe. In practice, simple SSB and SSB+Ni-doping can achieve accurate measurements with precisions that are comparable.

A virtue of the SSB bracketing technique is that instrumental stability (and error bars) can be ascribed on the basis of the reproducibility of the standards that are used to bracket the sample measurements. One can, of course, use the standard deviation of the sample measurements to quantify error bars. The number of sample solution measurements is usually limited (typically up to ~10 for high precision measurements but most often just a few), so a large Student *t*-factor has to be applied to calculate the 95% confidence interval and the errors thus calculated are not very robust. In contrast, there are typically tens of standard

measurements during a session, which provide a better estimate of the instrument stability. From the n standard measurements in a session, one can calculate $n-2$ δ-values of the standard bracketed by itself, $(1,2,3)\ldots(i-1,i,i+1)$, $(n-2,n-1,n)$, and use the standard deviation of those $n-2$ values σ_{STD} as a measure of error. If a sample solution is measured k times, one can take the mean of those k measurements and ascribe an error of $\pm 2\sigma_{STD}/\sqrt{k}$. In practice, other sources of errors than mass spectrometry limit error bars to ±0.03‰, regardless of the number of replicate analyses (Dauphas et al. 2009a)

The double-spike (DS) technique is the technique of choice in TIMS. It has gained a renewed attention in MC-ICPMS, in particular for elements that are present at trace levels, are difficult to fully purify, and have low chemical yields. A difficulty with the DS technique is that it is a bit more complicated to implement, as a double-spike solution needs to be calibrated and mixed with the sample in the right proportions. Rudge et al. (2009) recently presented a comprehensive study of the DS method, evaluating mixing proportions to minimize error magnification under the assumption that the total quantity of sample+spike must remain constant, so that increasing the quantity of spike used necessitates using less sample and vice versa. Under this assumption, the smallest error propagation is achieved for a 48% ^{57}Fe+52% ^{58}Fe DS mixture mixed with the sample in a proportion 45% DS+55% sample. However, the assumption that the total quantity of sample+spike cannot vary does not represent realistic conditions and the values calculated by the double-spike toolbox are not preferable. In practice, the quantities of sample and spike can be varied independently, subject only to the quantity of sample available and the maximum signal which can be measured on the detectors. Using a Monte Carlo method, John (2012) found that the DS compositions suggested by Rudge et al. (2009) were a good starting point, but that sample spike mixtures should generally be chosen to maximize the total quantity of sample+spike analyzed. For δ^{56}Fe, when sample quantity is not limited, a mixture of ~33% sample and ~67% spike is preferred because this produces a mixture with similar quantities of ^{56}Fe, ^{57}Fe, and ^{58}Fe which allows for each of these isotopes to be collected near the maximum voltage of the detector (assuming that each detector has the same range). When sample quantity is limited there may be a decrease in the theoretical error by further increasing the proportion of spike used. The overall error in δ^{56}Fe is, however, dominated by the small amount of ^{54}Fe, so there is little additional gain from increasing the proportion of spike above ~67%. In practice, there is no mathematically optimum DS composition and sample-spike mixture which is best for all conditions but a mixture of sample and spike in a 1:2 ratio with a DS composed of equal proportions of ^{57}Fe and ^{58}Fe is a good practical choice because it yields close to the minimum error under a very wide range of analytical conditions (Fig. 2) (John 2012).

Double-spike is always preferred to triple-spike (Millet and Dauphas 2014) because when adding another isotope, the mixture always resembles more the natural composition and the error propagation factor increases (in the limit of a spike with isotopic ratios similar to the sample composition, the double or triple spike acts as an isotope dilutant and provides no constraint on the isotopic composition of the sample; only on its concentration). Dideriksen et al. (2006) first applied the DS to MC-ICPMS measurements of iron. Millet et al. (2012) showed that double-spike measurements could provide precisions on par with the best SSB measurements, often in fewer replicate analyses. In double-spike analysis, a synthetic mixture of isotopes is mixed with the sample and the isotopic composition is measured (Dodson 1963; Albarède and Beard 2004; Rudge et al. 2009). To very high precision, all iron isotope variations in solar system materials are related to the terrestrial (IRMM–014) composition by mass-dependent fractionation (assumed to follow the exponential law below; but the exact form of the law has little influence) (Dauphas et al. 2004a, 2008; Tang and Dauphas 2012), so we can write that the ratio $R_{2/1}^{SMP} = i_2 / i_1$ in the sample is related to the ratio in the IRMM–014 standard through,

$$R_{2/1}^{SMP} = R_{2/1}^{STD} \left(m_2 / m_1 \right)^{\alpha} \quad (5)$$

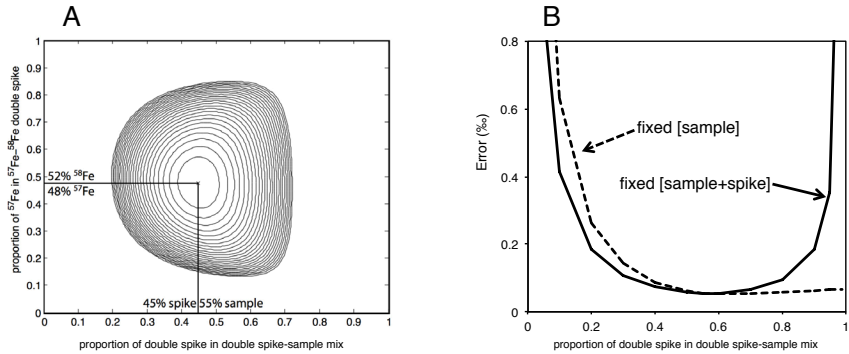

Figure 2. The effect of double-spike composition and mixing proportions on analytical δ^{56}Fe errors. The double-spike toolbox of Rudge et al. (2009) has been used to calculate the optima based on an assumption of a total sample + spike ion beam of 10 V on $10^{11}\,\Omega$ detectors and isotopically pure spikes (A). The contours represent lines of equal errors which are evenly spaced corresponding to intervals of 1% increments relative to the optimal error (cross). The Monte Carlo method of John (2012) was used to calculate the optimum mixing proportions using a similar DS composition, but different assumptions about sample and spike quantities (B). When the total quantity of sample + spike is fixed, the results are similar to those of Rudge et al. (solid black line). With only the concentrations of sample fixed (for example when only a small amount of sample is available) error is minimized with a ~1:2 mixture of sample and spike, and further increases in spike quantity have very little effect on error. When sample quantity is not limited, a 1:2 mixture of sample and spike is also beneficial because ^{54}Fe, ^{56}Fe, and ^{57}Fe are present in similar quantities so that high concentrations of sample can be run without overloading detectors. When sample + spike voltages approach the detector limitations, increasing the proportion of spike higher than ~1:2 is expected to increase error because it requires using less sample (not shown).

where α quantifies the extent to which the sample is fractionated relative to the standard, which is the unknown that must be estimated in the DS data reduction procedure. The sample is mixed with a spike of non-natural composition. We note f_1^{SP} the fraction of isotope i_1 that comes from the spike ($1-f_1^{SP}$ is the fraction that comes from the sample). We have for the mixture,

$$R_{2/1}^{\mathrm{MIX}} = f_1^{\mathrm{SP}} R_{2/1}^{\mathrm{SP}} + \left(1 - f_1^{\mathrm{SP}}\right) R_{2/1}^{\mathrm{SMP}} = f_1^{\mathrm{SP}} R_{2/1}^{\mathrm{SP}} + \left(1 - f_1^{\mathrm{SP}}\right) R_{2/1}^{\mathrm{STD}} \left(m_2 / m_1\right)^{\alpha} \tag{6}$$

The mixture is fractionated during chemical processing and isotopic analysis. We note β the exponent of the exponential law corresponding to this fractionation. We have for the measured ratio $r_{2/1}^{\mathrm{MIX}}$,

$$r_{2/1}^{\mathrm{MIX}} = \left[f_1^{\mathrm{SP}} R_{2/1}^{\mathrm{SP}} + \left(1 - f_1^{\mathrm{SP}}\right) R_{2/1}^{\mathrm{STD}} \left(m_2 / m_1\right)^{\alpha} \right] \left(m_2 / m_1\right)^{\beta} \tag{7}$$

There are three unknowns in this equation, α, β, and f_1^{SP}. If one assumes that all mass-fractionations can be related to the terrestrial standard composition by a mass-dependent law (here exponential), then one can write the same equation for 3 isotope pairs (e.g., ^{56}Fe/^{54}Fe, ^{57}Fe/^{54}Fe, and ^{58}Fe/^{54}Fe) and solve the system as α, β, and f_1^{SP} are the same for all these ratios. Instrumental mass fractionation in MC-ICPMS is large and the law describing it is not always precisely known, although it is well approximated by the exponential law (Maréchal et al. 1999). The absolute isotopic ratios after double-spike data reduction are variable from session-to-session and can show drifts within a session. In MC-ICPMS, the double-spike approach is therefore often used in tandem with the SSB technique, meaning that samples and standards are spiked at the same level and the δ-values are calculated from the isotopic ratios of the sample and bracketing standards after DS data reduction.

To properly use the double-spike technique, one should dope the sample with the spike as early as possible in the procedure (i.e., before digestion), to ensure that iron in the sample

and spike are completely equilibrated, and more importantly to account for any lab-induced isotopic fractionation. Such fractionations could arise during dissolution if some analyte is lost as precipitate and more importantly during chromatographic separation if the yield is not 100%. Iron is a major rock-forming element and even when digesting a few mg of samples, the amount of spike needed to spike the sample at that stage would be prohibitively expensive. Therefore, the double-spike technique as it has been applied in iron isotope geochemistry (Dideriksen et al. 2006; Millet et al. 2012) departs from the golden standard DS approach, as iron is first purified from the sample by chromatography and the DS is then added just before mass spectrometry to correct for instrumental mass fractionation. Iron DS measurements as they have been applied so far thus suffer from some of the same shortcomings as the SSB method, meaning that a high yield is needed to ensure that the measurements are accurate. The DS technique can also suffer from the fact that more isotopes are involved in the reduction and high washout times are needed as the isotopic ratios can vary significantly from sample to sample. Finally, use of the double-spike technique does not allow one to investigate easily mass fractionation laws and potential isotopic anomalies.

To summarize, various strategies exist for measuring the isotopic composition in rocks at high precision that all have advantages and shortcomings. A very reassuring fact is that geostandards are routinely measured in all laboratories practicing iron isotope geochemistry and the results obtained by the various methods agree, even down to precisions of ±0.03‰ on δ^{56}Fe (Fig. 3). This, together with extensive testing performed in laboratories practicing iron isotope geochemistry, gives confidence that iron isotope measurements are accurate at those levels and minute iron isotope variations can be discussed with confidence. New practitioners of iron isotope geochemistry should run well-documented geostandards with a range of δ^{56}Fe values (e.g., BCR–2, BHVO–1, BHVO–2, BIR–1, AC-E, AGV–2, IF-G; Craddock and Dauphas 2011) to ensure that their results are accurate.

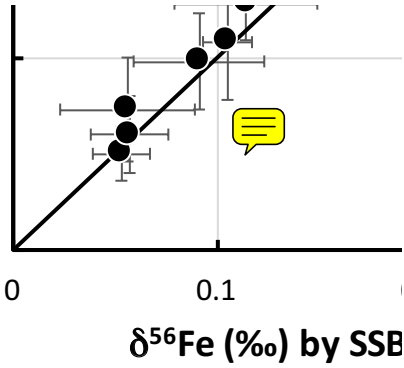

Figure 3. Comparison between Fe isotopic analyses of geostandards (BHVO–2, BCR–2, JB2, BIR–1, AGV–2, JA1, GSP–1, RGM–1) by Sample Standard Bracketing –SSB (Weyer et al. 2005; Craddock and Dauphas 2011a; Liu et al. 2014) and double-spike –DS (Millet et al. 2012). The excellent agreement between SSB and DS, which are sensitive to different analytical pitfalls, supports the accuracy of these measurements. Accurate Fe isotopic analyses can be routinely performed with precisions of ~±0.03‰ on δ^{56}Fe.

Water samples

The analysis of Fe isotopes in water samples presents unique challenges. In liquids where Fe concentrations are high (~μM), such as hydrothermal fluids, sediment porewaters, and river waters, it is generally possible to dry down the liquid and redissolve the residue in concentrated HCl for anion exchange purification using the same procedures as utilized for solid and rock samples. For liquid samples where Fe concentrations are much lower, such as seawater, additional methods are used to concentrate iron and remove it from high concentrations of matrix elements before proceeding with anion exchange purification and analysis.

Seawater δ^{56}Fe analyses present a great challenge because of the very low concentrations of Fe in seawater and the high concentration of dissolved salts which must be removed from the sample before analysis. Away from particular Fe sources such as hydrothermal vents or reducing sediments, the concentrations of Fe in seawater typically range from as low as 0.02 nM in the surface ocean to around 1 nM in the deep ocean, corresponding to roughly 1–50 ng of Fe per L of seawater. Analytical developments have made it possible to accurately measure δ^{56}Fe on a few ng of Fe, but it is still necessary to extract iron from liters of seawater to make a measurement. Simply drying down this seawater is not an option because this is impractical, and large amounts of HCl and resin would be needed for redissolution and iron purification, at which point the blank would overwhelm the quantity of Fe present in the sample.

Analyses of δ^{56}Fe in seawater and other dilute liquid matrices therefore require a preconcentration step before anion exchange purification. Early efforts concentrated Fe from seawater by coprecipitating Fe with $Mg(OH)_2$ after increasing the pH by ammonia addition (de Jong et al. 2007), though this method still results in relatively high salt concentrations after preconcentration which seem to interfere with subsequent analyses. More recently, seawater Fe has been pre-concentrated from seawater onto resins with organic chelating moieties that have a very high affinity for Fe and can bind Fe even at pH as low as 2. A resin with NTA (nitroloacetic acid) functional groups has been used for extracting Fe from seawater in both batch and column processes (John and Adkins 2010; Lacan et al. 2010; Rouxel and Auro 2010). A similar resin with ethylenediaminetriacetic acid (EDTriA) functional groups has been used in batch form and has been found to have slightly lower blank, and has the additional benefit of being able to simultaneously preconcentrate Fe, Zn, and Cd from the same seawater samples (Conway et al. 2013). Further purification and analysis of samples is achieved using methods similar to those for other geological samples, with modifications to increase analytical sensitivity and minimize contamination. For example, anion exchange chromatography is typically performed on smaller columns in order to reduce blank, with some methods using as little as 35 μL of resin (Conway et al. 2013). A typical MC-ICPMS setup includes several changes to increase sensitivity such as the use of an Apex desolvating inlet system, the use of larger hole-diameter cones (e.g., Jet sampler cones and X skimmer cones for the Neptune), and the use of higher impedance resistors (John and Adkins 2010; John 2012; Lacan et al. 2010; Rouxel and Auro 2010; Conway et al. 2013).

In situ analyses

The focus of the first *in situ* (i.e., spatially resolved) stable iron isotope analyzes, by either secondary ion mass spectrometry (SIMS) or MC-ICPMS, was on samples that displayed large fractionations such as banded-iron formations (BIFs). The δ^{56}Fe value of those samples range between approximately –1.5 and +2‰, so that the precisions of *in situ* techniques (±0.1 to ±0.4‰) were sufficient to detect those variations (Horn et al. 2006; Whitehouse and Fedo 2007). The scope of *in situ* analyses of iron isotopes has significantly expanded over the past 10 years, as the analytical capabilities and methodological approaches have improved.

One important difficulty of *in situ* analyses is the evaluation of accuracy. Indeed, the matrix standards used for correction of instrumental artifacts are ideal model compositions that fail to capture the chemical and structural complexity of a natural system. Micromilling can help bridge the gap between bulk and *in situ* analyses. Sampling by micromilling is done by depositing a drop of water on the sample and drilling the sample surface through that water droplet (Charlier et al. 2006; Sio et al. 2013). The sample slurry thus produced can be retrieved using a fine pipette. The powder retrieved can then be processed through chemistry like regular bulk samples. The hole size made by the tungsten carbide milling tip can be ~300 μm in diameter and ~300 μm depth.

Iron isotopic analyses by SIMS have targeted several matrices, most notably sulfides, magnetite, and olivine. The instrument of choice for *in situ* SIMS iron isotopic analysis has been the Cameca–1270 or 1280. Whitehouse and Fedo (2007) measured the iron isotopic compositions of magnetite and seconday pyrite in >3.7 Ga old BIFs from Isua (southwestern Greenland). The quoted precision of those measurements is ±0.4‰ and the authors reported variations of up to 2‰ in δ^{56}Fe for magnetite grains a few millimeters apart. These BIFs are highly metamorphosed (to amphibolite facies) and no such variation was found in equivalent samples from Isua and Nuvvuaggituq when measured by micromilling, wet chemistry and MC-ICPMS (Dauphas et al. 2007a,b). Kita et al. (2011) reported SIMS analyses of iron isotopes in magnetite for which they achieved a precision of ±0.2‰ on δ^{56}Fe. They found some grain-to-grain variability of 0.6‰ but reported a correlation between $^{56}Fe^{+}$ ion yield and δ^{56}Fe values. They suggested that it could be a crystallographic orientation effect, meaning that the instrumental mass fractionation depends on the crystallographic orientation of the magnetite grain relative to the incident beam, which could explain the discrepancy between previous SIMS (Whitehouse and Fedo 2007) and micromilling measurements (Dauphas et al. 2007a; 2007b). Marin-Carbonne et al. (2011) presented the most extensive technical study of *in situ* iron isotopic analyses by SIMS. In particular, they explained in detail how an unresolvable ^{54}Cr interference on ^{54}Fe could be corrected for by monitoring the intensities of ^{52}Cr and ^{53}Cr. They reported precisions of ±0.3‰. More emphasis was put on magnetite analyses but instrumental mass fractionation was also reported for metallic iron, siderite, hematite, and pyrite. The technique was applied in a subsequent paper to the analysis of pyrite in 2.7 Gyr old shales (Marin-Carbonne et al. 2014). Through combined δ^{56}Fe and Δ^{33}S analyses, the authors showed that the pyrite nodules could not have formed solely by dissimilatory iron reduction and sulfate reduction (two respiration modes that use oxidized forms of iron and sulfur in place of O_2 as electron acceptors) but must have involved a complex diagenetic history and source mixing.

SIMS measurements were also used to address questions relevant to high-temperature geochemistry and cosmochemistry. In these fields, the temperatures involved are high enough that no equilibrium isotopic fractionation is expected to be measurable by SIMS. Kinetic effects can still impart large fractionation at magmatic temperatures (Richter et al. 2009a). One such process is evaporation/condensation. *In situ* measurements by SIMS of Fe–Ni zoned metal grains from CBb chondrites have revealed large iron isotopic fractionation spanning ~10‰ on δ^{56}Fe that is correlated with Ni isotopic fractionation (Alexander and Hewins 2004; Richter et al. 2014a). Those large effects were also found by laser-ablation MC-ICPMS (Zipfel and Weyer 2007). They are interpreted to reflect kinetic isotopic fractionation associated with partial condensation of metallic Fe and Ni in the aftermath of a vapor-forming impact in the early solar system. Another kinetic process that can impart significant isotopic fractionation at high temperature is diffusion. Sio et al. (2013) measured a zoned olivine xenocryst from Kilauea Iki lava lake by SIMS (Fig. 4). They found large iron isotopic fractionation that corresponds to what is expected for diffusion in olivine, meaning opposite to that measured for Mg isotopes and corresponding to a light iron isotope enrichment in the core of the xenocryst. SIMS instrumental isotopic fractionation for iron in olivine is large and highly sensitive to the forsterite content (spanning almost 10‰ in δ^{56}Fe between Fo_0 and Fo_{100}). Nevertheless, this can be well corrected for, yielding accurate iron isotopic analyses with precisions of ~0.3‰.

Laser-ablation (LA) MC-ICPMS has been used quite extensively in iron isotope systematics. The natural samples that were targeted for isotopic analysis by this method are the same as the ones that were measured by SIMS, namely samples formed in low-*T* aqueous environments and high-*T* samples where transport processes (diffusion, evaporation, condensation) fractionated iron isotopes. The equipment used to carry out those measurements is diverse, as various lasers can be used with various ablation cells to feed different types of MC-ICPMS. The 193 nm ArF Excimer nanosecond lasers are efficient at ablating a large variety of matrices but their main

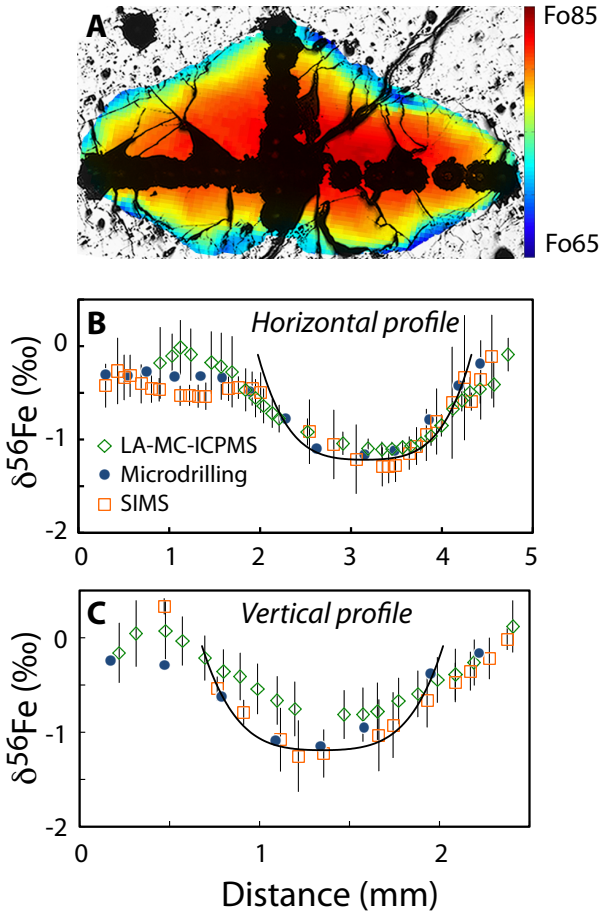

Figure 4. Fe isotopic compositions across a zoned olivine phenocryst from Kilauea Iki lava lake (Sio et al. 2013). The top image (A) is a false color image of the olivine (the colors [online] indicate the Fo content). The middle (B) and bottom (C) panels show comparisons of the measurements made by LA-MC-ICPMS, microdrilling, and SIMS. The continuous curve is a model calculation for isotopic fractionation driven by diffusion. Mg is more compatible than Fe in olivine. During magmatic evolution, Mg will diffuse out while Fe will diffuse in because the melt is becoming progressively more Fe-rich and Mg-poor. The light Fe isotopes diffuse faster than the heavy ones, which explains why the olivine core has negative δ^{56}Fe. Isotopic profiles can help tease apart zoning due to crystal growth from zoning due to diffusion.

drawback is that significant energy is converted into heat, which can effectively vaporize and melt the target sample, inducing significant iron isotopic fractionation that is matrix-dependent. Femtosecond lasers deposit energy over a very brief pulse duration, so the sample ablation is associated with less collateral heating and attendant melting and vaporization. The degree of isotopic fractionation imparted by the laser ablation in femtosecond measurements is consequently smaller than with Excimer lasers. The aerosols produced by laser ablation are carried into the mass spectrometer by a flow of Ar+He. Helium yields the best transport efficiency but it has to be mixed with argon for plasma stability (Günther and Heinrich 1999). The efficiency with which the ablated aerosols are carried to the torch also depends on the ablation cell construction and geometry. The two-volume cell technology (e.g., Laurin Technic) is particularly well suited for MC-ICPMS (Müller et al. 2009). It indeed allows measuring samples exposed over large

surface areas while keeping the ablation volume to a minimum, thus promoting fast washout between samples and efficient aerosol transport. The mass-spectrometer plays a lesser role than the nature of the laser, ablation cell, and ablation parameters used. Data acquisition in LA-MC-ICPMS is a bit different than using more standard sample introduction systems because the signal can be recorded constantly, so the beginning and end of a measurement are defined in post-processing by examining (either manually or through an automated algorithm) signal increase and decrease associated with sample introduction and washout.

Horn et al. (2006), and Horn and von Blanckenburg (2007) pioneered the use of LA-MC-ICPMS in iron isotope analyses. They used a 196 nm UV-femtosecond laser with a pulse width of ~100–200 femtosecond on a variety of mineral matrices: iron metal, sulfides, hematite, siderite, goethite, and magnetite. The IRMM–014 metal reference material was used as bracketing standard. They showed that with this setup, matrix matching was not critical and that precisions of better than ~0.1‰ could be achieved for an ablation hole size of 35 μm. Comparison of LA-MC-ICPMS results with values measured by solution MC-ICPMS after chemical purification validated the method. As with SIMS, Cr and Ni isobaric interferences cannot be resolved in mass from iron peaks, so these interferences are corrected for by monitoring masses ^{52}Cr and ^{60}Ni. Steinhoefel et al. (2009a) expanded this work to the analysis of silicates, which can contain significant amounts of Cr and Ni, so that the correction for isobaric interferences can become unreliable and δ^{56}Fe is calculated as $2 \times \delta^{57/56}$Fe, meaning that ^{54}Fe is not involved in this calculation. The precision achievable for silicates is similar to that reported for metals, oxides, hydroxides, sulfides and carbonates (i.e., ±0.1‰ on δ^{56}Fe) and the measurements appear to be accurate even when a mismatched standard matrix is used for bracketing the samples. Steinhoefel et al. (2009b, 2010) measured the Fe isotopic compositions of minerals in BIFs of low metamorphic grades and found significant Fe isotopic fractionation between layers. They also found that δ^{56}Fe values of bulk BIF layers correlate coarsely with the Si isotopic composition of those layers, the explanation of which is still unclear. Dziony et al. (2014) applied the same technique to the analysis of ilmenite and magnetite in basalt and gabbros, and found significant fractionation between those two minerals, inconsistent with high temperature equilibrium. Those fractionations must reflect kinetic isotope effects associated with interactions between magmas and surrounding hydrothermal fluids. Oeser et al. (2014) reported *in situ* measurements of reference glasses BIR-1G, BCR-2G, BHVO-2G, KL2-G, ML3B-G, GOR128-G, and GOR132-G, by femtosecond laser mass spectrometry. They showed that the glasses have uniform Fe isotopic compositions, so they can be used as secondary bracketing standards in *in situ* analyses for analytical techniques that require matrix matched standards. Building on ideas of Poitrasson and Freydier (2005) and O'Connor et al. (2006), Oeser et al. (2014) also showed that using Ni as an external mass bias monitor (which is introduced as a Ni standard solution into the plasma along with the ablation aerosol) can significantly improve the accuracy and reproducibility of *in situ* Fe isotope analyses by LA-MC-ICPMS.

Horn et al. (2006) used a UV femtosecond laser but equally good results can be obtained by near-infrared (NIR) femtosecond laser (Nishizawa et al. 2010). Specifically, Nishizawa et al. (2010) used a NIR 780 nm femtosecond (227 fs pulse length 20 Hz repetition rate) to measure the Fe isotopic composition of pyrite grains. The measurements were done by rastering a 40 × 40 μm surface with a 10 μm laser beam, and excavating sample material over a depth of ~10 μm. The sample measurements were bracketed by standard pyrite measurements and the authors were able to achieve a precision of ±0.3‰ on δ^{56}Fe. They applied this technique to the analysis of pyrite grains associated with shallow marine carbonates.

d'Abzac et al. (2013) found significant isotopic fractionation between different aerosol size fractions produced by femtosecond laser. This fractionation depends on the mineral analyzed and is close to zero for pyrite but can reach 2‰ for magnetite. This probably results from kinetic isotopic fractionation during condensation. To minimize mass fractionation in femtosecond

laser ablation, it is thus important to ensure that no size sorting can occur during transport to the plasma torch or that all aerosol sizes are efficiently ionized. Different ablation cells (e.g., single vs. two-volume) and laser wavelengths can influence the extent of this fractionation. A two volume cell seems to yield the most stable and best isotopic results (d'Abzac et al. 2014).

Recently, nanosecond lasers have taken a back seat relative to femtosecond lasers. The reason is that nanosecond lasers impart more variable isotopic fractionation that is matrix dependent (Graham et al. 2004; Košler et al. 2005; Sio et al. 2013; Toner et al. 2016). By exercising some care in matching the matrix well and assessing positional effects, it is nevertheless possible to generate high precision measurements. Sio et al. (2013) measured the isotopic composition of Fe in olivine using a 193 nm Excimer laser ablation system with a relatively large single cell ablation setup. Between Fo_{55} and Fo_{95}, the degree of instrumental mass fractionation changed by ~0.8‰. By bracketing the measurements with standards matched in Fo content, that bias was corrected for. Another bias was present that depended on the position of the laser spot in the ablation cell. To correct for this positional effect, Sio et al. (2013) measured the same profile after rotating the sample. Assuming that the bias introduced by the ablation varies linearly with position in the cell, then doing the same measurement at zero angle and rotating the sample by 180° around the center of the mount should eliminate this effect. Sio et al. (2013) measured the same sample by laser ablation ICPMS, SIMS and microdrilling and the isotopic profile generated by these three independent techniques are in excellent agreement, lending confidence to each of these techniques (Fig. 4).

Isotopic anomalies and mass-fractionation laws

The methodologies outlined above focus on the mass-dependent component of the isotopic variations. By mass-dependent, we mean that the isotopic variations scale, within the precision of the measurements, with the difference in mass of the isotopes involved. For example, $\delta^{56}Fe \simeq \delta^{57}Fe \times (56-54)/(57-54)$. Isotopic variations can depart from a reference mass fractionation law (e.g., the exponential law) for two reasons: nucleosynthetic anomalies could be present, or the mass-fractionation law controlling the isotopic variations may differ from the reference law that is used (Dauphas and Schauble 2016). Isotopic anomalies or departures from a reference mass fractionation law are usually calculated by internal normalization. This consists of fixing an isotopic ratio to a constant value and correcting mass fractionation accordingly using the reference law. The $^{57}Fe/^{54}Fe$ ratio and exponential law are most often used for internal normalization (Dauphas et al. 2004a; 2008; Tang and Dauphas 2012). The exponent parameter of the exponential law is given by (Eqn. 3; $M_{^{i}Fe}$ is the mass of isotope ^{i}Fe),

$$\beta^{*} = \frac{\ln\left[\left(^{57}Fe/^{54}Fe\right)_{measured} / \left(^{57}Fe/^{54}Fe\right)_{reference}\right]}{\ln\left(M_{^{57}Fe}/M_{^{54}Fe}\right)} \tag{8}$$

The $^{56}Fe/^{54}Fe$ and $^{58}Fe/^{54}Fe$ ratios corrected by internal normalization (noted R^{*}) are given by,

$$\left(\frac{^{56}Fe}{^{54}Fe}\right)^{*} = \left(\frac{^{56}Fe}{^{54}Fe}\right)_{measured} \left(M_{^{56}Fe}/M_{^{54}Fe}\right)^{\frac{\ln\left[\left(^{57}Fe/^{54}Fe\right)_{reference}/\left(^{57}Fe/^{54}Fe\right)_{measured}\right]}{\ln\left(M_{^{57}Fe}/M_{^{54}Fe}\right)}} \tag{9}$$

$$\left(\frac{^{58}Fe}{^{54}Fe}\right)^{*} = \left(\frac{^{59}Fe}{^{54}Fe}\right)_{measured} \left(M_{^{58}Fe}/M_{^{54}Fe}\right)^{\frac{\ln\left[\left(^{57}Fe/^{54}Fe\right)_{reference}/\left(^{57}Fe/^{54}Fe\right)_{measured}\right]}{\ln\left(M_{^{57}Fe}/M_{^{54}Fe}\right)}} \tag{10}$$

The notations used to discuss isotopic anomalies and mass fractionation laws are,

$$\delta' = 1000 \ln\left(R / R_{STD}\right) \simeq 1000\left(R / R_{STD} - 1\right)$$

$$\varepsilon' = 10{,}000 \ln\left(R^* / R^*_{STD}\right) \simeq 10{,}000\left(R^* / R^*_{STD} - 1\right)$$

ε' is the departure in parts per ten thousand of the internally normalized ratio of a sample relative to the internally normalized ratio of a standard. Usually, to define the internally normalized ratio of the standard, the same bracketing approach is used as when measuring mass-dependent fractionation. A standard (IRMM–014, IRMM-524a) is measured between samples, and the composition of the standard goes through the same internal normalization procedure as the sample. If all samples were derived from the same terrestrial Fe isotopic composition by the exponential law, then their ε' value would be zero. Measurements of mass-independent effects are demanding as the expected effects are small and inaccuracy may arise from isobaric interferences.

Isotopic anomalies have been documented in presolar grains (Marhas et al. 2008) as well as some early solar system condensates known as FUN refractory inclusions (FUN stands for Fractionated and Unknown Nuclear effects). In FUN inclusions, anomalies on ^{58}Fe reach ~+300‰ (Völkening and Papanastassiou 1989). The other isotopes do not display marked departures from the terrestrial mass fractionation line. Some effort has also been expanded towards searching for the presence of nucleosynthetic iron isotopic anomalies at a bulk scale but no such anomaly has been detected so far (Dauphas et al. 2004, 2008; Tang and Dauphas 2012).

Departures from mass-dependent fractionation can also arise because the fractionation is either not mass-dependent or it is mass-dependent but follows a different law than exponential (or the reference law adopted) (Matsuhisa et al. 1978; Luz et al. 1999; Young et al. 2002; Dauphas and Schauble 2016). For example, Steele et al. (2011) found small anomalies in Ni purified by the Mond process (an industrial process that involves evaporation of Ni as a nickel tetracarbonyl). No such effect has been documented thus far for iron. Recently, Nie and Dauphas (2015) and Nie et al. (2016) studied iron isotope mass fractionation in products of partial UV-photo-oxidation. The measurements were made at high precision, allowing identification of the underlying mass fractionation law, which was found to be equilibrium. Banded iron formation must have formed by partial iron oxidation in the water column but the exact mechanism for BIF formation is uncertain and three scenarios are usually considered. The first scenario involves partial oxidation by O_2 in oxygen oases. The second scenario is oxidation by anoxygenic photosynthesis, whereby Fe^{2+} is used as an electron acceptor in place of water in photosynthesis. The third scenario is photo-oxidation, whereby the energetic UV photons from the Sun could have induced photo-oxidation of iron. Evidence for and against these various scenarios is circumstantial. Nie and Dauphas (2015) and Nie et al. (2016) measured the extent of iron isotopic fractionation imparted by photo-oxidation and found that it was similar to other oxidation processes, so photo-oxidation remains a viable explanation for iron oxidation in the Archean oceans.

KINETIC AND EQUILIBRIUM FRACTIONATION FACTORS

Over the past several years, some progress has been achieved on the front of mass spectrometry capabilities. These include (1) development of new plasma interfaces that use different cone geometries (Jet cones) and higher capacity vacuum pumps, which increases instrument sensitivity, and (2) development of femtosecond laser capabilities and two volume cells for isotopic analysis by LA-MC-ICPMS. However, those developments have not been complete game changers for iron isotope geochemistry, where sensitivity is not an issue and most geological questions can be addressed by macro-scale measurements. Where significant progress was made is in documenting iron isotope variations in nature, as well as developing the framework for interpreting iron isotope variations in rock and water samples.

By framework, we mean establishing the kinetic and equilibrium fractionation factors that control iron isotopic variations in natural systems. This was achieved through a combination of ab initio calculations, experimental studies, synchrotron measurements of iron bond strengths, and studies of well-constrained natural case studies.

Kinetic processes

Diffusion. Diffusive processes are very efficient at fractionating isotopes. The light isotopes diffuse faster than the heavier ones, such that in diffusive processes, the source reservoir gets enriched in the heavy isotopes while the sink reservoir gets enriched in the light isotopes. The manner in which diffusion-driven isotopic fractionation is empirically parameterized in isotope geochemistry is,

$$\frac{D_2}{D_1} = \left(\frac{m_1}{m_2}\right)^{\beta} \tag{11}$$

where D_1 and D_2 are the diffusivities of isotopes 1 and 2, and β is a parameter that can vary between 0 (no isotopic fractionation) and 0.5 (equipartition of energy in a monoatomic gas). Note that the β notation here is not the same as the one used to describe the exponential mass fractionation law (e.g., Eqn. 3) or the β-factor (reduced partition function ratio) used in stable isotope geochemistry to calculate equilibrium isotopic fractionation between phases.

Some of the earliest iron isotope diffusion experiments were carried out on metals to learn about the diffusion mechanism (LeClaire and Lidiard 1956; McCracken and Love 1960; Pell 1960; Mullen 1961). Dauphas (2007) and Richter et al. (2009a) provide extensive compilations of β exponents for diffusion in metals. Those early experiments (e.g., Mullen 1961) used radioactive iron isotopes ^{55}Fe and ^{59}Fe as sources, let them diffuse in metal, and measured the ^{55}Fe/^{59}Fe ratio in metal after diffusion. All the experiments give β exponents of around 0.25 (Dauphas 2007), with little influence of the crystalline structure (α, γ or δ) or the nature of the metal (Fe in Cu, Ag, V, FeCo). More recently, Roskosz et al. (2006) also measured the β exponent of Fe in Pt by mass spectrometry and reported a value of ~0.27; close to the values estimated in the 60s and 70s in other metals. Such a large β exponent means that diffusion in metal is very efficient at fractionating iron isotopes, a feature that has important consequences for interpreting iron isotopic variations in iron meteorites (Dauphas 2007).

Iron diffusion in silicate melts of relevance to geological processes was studied by mass spectrometry. In that case, one has to specify what redox state is concerned, as Fe^{2+} and Fe^{3+} can be present in any proportions in silicate melts synthesized in the laboratory. Richter et al. (2009b) studied diffusion of iron in silicate by juxtaposing basaltic and rhyolitic melts. Iron in those experiments was most likely present as both Fe^{2+} and Fe^{3+} as the oxygen fugacity was probably between WM and FMQ (Richter, personal communication). Richter et al. (2009b) found a β-exponent of 0.030; much lower than in metal. A controlling factor on the degree of isotopic fractionation imparted by diffusion in silicate melts seems to be the contrast in diffusivity between the solute and the solvent, i.e., D_{Fe}/D_{Si}. Elements with lower solute/solvent contrast tend to display lower isotopic separation by diffusion (they are more strongly bound to the network) (Watkins et al. 2011).

Diffusive fractionation of Mg and Fe isotopes in olivine has been discussed in the context of the establishment of forsterite zoning in that mineral (Fig. 4). No clear laboratory experiment has been performed so far to establish this value but studies of natural olivines provide useful bounds on this fractionation. Dauphas et al. (2010) and Teng et al. (2011) showed that the inverse correlation between Mg and Fe isotopic compositions required that β_{Fe}/β_{Mg} be ~2. Subsequent work by Sio et al. (2013) and Oeser et al. (2015) constrained the β exponent (Eqn. 11) between 0.16 and 0.25; i.e., much higher than the value inferred for silicate melt. Further work is clearly needed to ascertain this value but it is clear that the β_{Mg} and β_{Fe} values for diffusion in olivine are large.

Diffusive fractionation of iron isotopes was also documented for both Fe^{2+} and Fe^{3+} in aqueous medium. Rodushkin et al. (2004) let Fe diffuse in a solution of 0.33 mol/L HNO_3 (pH 0.5). The authors seem to infer that Fe is present as Fe^{2+} but given the relatively oxidizing conditions, it is likely that some Fe would be oxidized into Fe^{3+}. Regardless of this complication, Rodushkin et al. (2004) finds β exponents of around 0.0015 and 0.0025 for Zn and Fe, respectively. Note that Zn is present as 2+ and has similar diffusive properties as Fe^{2+}. The β exponent for diffusion of iron in aqueous solutions is thus very low and it is likely that diffusion in natural aqueous systems played a negligible role in governing iron isotopic fractionation (Dauphas and Rouxel 2006). The reason why the β exponent is so small probably stems from the fact that Fe or Zn do not diffuse as free ions but are instead surrounded by a large solvation shell (e.g., hexaaqua ions; Fe^{2+} or Fe^{3+} surrounded by a first hydration shell composed of 6 water molecules with the oxygen atoms pointing towards iron), so that the difference in mass of the effective diffusing molecule must be small when iron isotopes are substituted. As with silicates, the contrast $D_{solute}/D_{solvent}$ (D_{Fe}/D_{H_2O} with D_{H_2O} the self-diffusion coefficient of H_2O) seems to correlate with the degree of isotopic fractionation imparted by diffusion (Watkins et al. 2011).

Soret Diffusion. Soret or thermal diffusion is the process by which elements when placed in a thermal gradient can concentrate at the hot or cold ends. Bowen (1928) recognized almost 100 years ago that the timescale for heat transport is always much faster than the timescale for chemical diffusion, such that any thermal gradient would be erased before atoms can move significantly. This means that a thermal gradient must be actively sustained for Soret diffusion to occur in a natural setting. Lundstrom (2009) and Zambardi et al. (2014) have argued that Soret diffusion (or a more sophisticated version of this process that they named thermal migration zone refining) could be responsible for the differentiation of some granitoids. The past 10 years has seen some renewed interest in the Soret process, in large part due to the experimental work that showed that silicate melts placed in a thermal gradient develop chemical zoning, as is expected for Soret effect, but more surprisingly that this is accompanied by large isotopic zoning (Kyser et al. 1998; Richter et al. 2008; Huang et al. 2009). Iron isotopes are indeed fractionated by this process (Huang et al. 2009; Richter et al. 2009b). In Soret diffusion in silicate melts, the cold end gets enriched in the heavy isotopes of iron while the hot end gets enriched in the light isotopes of iron. The same is true for all isotope systems investigated, regardless of whether the elements themselves tend to concentrate at the cold or hot ends. Richter et al. (2009b) found that for each 100 °C contrast between the cold and hot ends, the $\delta^{56}Fe$ value will be fractionated by 2.2‰ (corresponding to 2 amu difference between ^{56}Fe and ^{54}Fe). Huang et al. (2009) reported a somewhat similar value of ~4‰/100 °C. Several attempts have been made to describe those fractionations using parameterized equations or simple models (Huang et al. 2010; Dominguez et al. 2011; Lacks et al. 2012; Li and Liu 2015), some of which have been subsequently questioned (Richter et al. 2014b). Even for gases, describing the Soret effect is quite involved and it depends on details of the interaction potential. Isotopic ratios are a very powerful approach by which one can test whether Soret diffusion is present in natural samples such as komatiites (Dauphas et al. 2010) or granitoids (Telus et al. 2012).

Evaporation/condensation. Evaporation and condensation played important roles in establishing the chemical and isotopic compositions of planets, meteorites, and their constituents. Condensation is difficult to investigate experimentally, so more attention has been paid to iron isotopic fractionation associated with evaporation. During either vaporization or condensation, the degree of isotopic fractionation is influenced by the degree of over- or under-saturation. Applying the Hertz-Knudsen equation to the evaporation and condensation processes, one can show that the isotopic ratio i/j will be fractionated according to (Richter et al. 2002, 2007; Richter 2004; Dauphas et al. 2015),

$$\Delta_{\text{Evaporation}} = \Delta_{\text{Equilibrium}} - \left(1 - \frac{P}{P_{\text{sat}}}\right)\Delta_{\text{Kinetic}} \tag{12}$$

$$\Delta_{\text{Condensation}} = \frac{P_{\text{sat}}}{P}\Delta_{\text{Equilibrium}} + \left(1 - \frac{P_{sat}}{P}\right)\Delta_{\text{Kinetic}} \tag{13}$$

where $\Delta_{\text{Evaporation}}$ is the isotopic fractionation between the condensed phase and the evaporating gas that is leaving the surface, $\Delta_{\text{Condensation}}$ is the fractionation between the solid/liquid that is condensing and the overlying vapor, P is the vapor partial pressure of the element of interest, P_{sat} is the saturation vapor pressure for that element, $\Delta_{\text{Equilibrium}}$ is the equilibrium isotopic fractionation between the condensed phase and the gas, and $\Delta_{\text{Kinetic}} = 1000\left(\frac{\gamma_i}{\gamma_j}\sqrt{\frac{m_j}{m_i}} - 1\right)$ is the kinetic fractionation factor, that depends on the evaporation coefficients γ and masses m of the isotopes involved. The experiments done so far for iron are free evaporation experiments, meaning that $\frac{P}{P_{\text{sat}}} = 0$ (Wang et al. 1994; Dauphas et al. 2004a). At the high temperatures relevant to iron evaporation in the nebula, the equilibrium fractionation factor is negligible and the fractionation, if any, is almost entirely kinetic. If the evaporation coefficients γ of the different isotopes are identical, then the fractionation is given by the inverse square root of the isotopes involved. This assumption is often made when investigating new isotopic systems but experiments have shown that this is not necessarily the case. The square root law for $^{56}Fe/^{54}Fe$ gives a kinetic isotope fractionation factor of 1.835‰ between condensed phase and vapor. During vacuum evaporation experiments, Dauphas et al. (2004a) and Wang et al. (1994) measured a fractionation of 1.877‰ for FeO evaporation, while Dauphas et al. (2004a) reported a value of 1.322‰ for a solar-like mixture of oxides. The evaporation coefficients of ^{54}Fe and ^{56}Fe seem to be approximately identical for FeO but they differ for the solar oxide mixture. Wiesli et al. (2007) also investigated equilibrium iron isotopic fractionation of iron pentacarbonyl between liquid and vapor and found very limited equilibrium iron isotopic fractionation of ~0.05‰ on $\delta^{56}Fe$.

Reaction kinetics. Of the isotope fractionation processes discussed here, chemical reaction kinetics is perhaps the most poorly understood. Firstly, chemical kinetic isotope effects lack a well-developed theoretical framework of the sort which is available for equilibrium processes and other kinetic processes such as diffusion. Secondly, reaction kinetic isotope effects are experimentally challenging to measure because it is difficult to design experiments where reaction occurs in a single step. Nonetheless, fractionation of Fe isotopes driven by reaction kinetics has been studied in a number of different ways.

So far, electron transfer is the only reaction kinetic isotope effect that has been studied theoretically. Using experimental results from the 2-electron reduction of Fe(II) to metallic Fe, Kavner et al. (2005) developed a theoretical framework for isotope fractionation during electroplating based on Marcus's theory for the kinetics of electron transfer (Marcus 1965). While this theory provides a valuable starting point for understanding isotope reaction kinetics, it lags behind theoretical studies of equilibrium isotope effects in two key respects. First, this theory has only been developed for redox kinetics, specifically for electroplating. Second, this theory has not yet been developed to make quantitative predictions of isotope fractionation. Subsequent work on Fe electrochemistry revealed that the observed $\delta^{56}Fe$ fractionations were not based on reaction kinetics alone. Instead, the observed isotope fractionation was the result of an interplay between the isotope effect of the reduction reaction at the electrode, the isotope effect of diffusion towards the electrode, and closed-system isotope effects due to Fe depletion within the boundary layer

next to the electrode (Black et al. 2010). While these experiments highlighted the complex way in which various kinetic isotope effects may interact, the simplicity of electroplating means that these processes are relatively well constrained compared to many other experimental conditions. It is likely that most experiments which seek to measure 'pure' reaction kinetic isotope effects are similarly confounded by a mixture of processes such as diffusion limitation, multiple reaction steps, and closed-system isotope fractionation of the reactants.

Still, with careful experimentation it may be possible to measure reaction kinetic isotope effects. Matthews et al. (2001) found large Fe isotope fractions between Fe(III) chloride complexes and Fe(II) bipyridine complexes, which they ascribe to a ~6.6‰ kinetic isotope effect during degradation of the $[Fe(II)(bipy)_3]^{2+}$. Skulan et al. (2002) measured the isotopic offset between aqueous Fe(III) and hematite under both equilibrium and kinetically dominated conditions, finding that while the equilibrium fractionation was close to 0, the kinetic isotope effect was −1.3‰. In addition to these experiments which have sought to explicitly measure reaction kinetic isotope effects, the result of reaction kinetic isotope effects are observed indirectly in many experimental systems such as during biological Fe oxidation (Croal et al. 2004; Balci et al. 2006) and during biological and abiotic mineral dissolution (Brantley et al. 2004; Wiederhold et al. 2006, 2007a; Chapman et al. 2009; Kiczka et al. 2010; Revels et al. 2015), and in natural systems such as the precipitation of Fe from seawater (John et al. 2012a) and the biological uptake of Fe from seawater (Ellwood et al. 2015). In these more complex systems, however, the isotope fractionation associated with a single-step chemical reaction cannot be deconvoluted from the overall observed isotope fractionation.

Equilibrium processes

When two or more phases are juxtaposed, iron isotopes can exchange until the system has reached thermodynamic equilibrium. Under those conditions, isotopes are not distributed uniformly among those phases. The manner in which isotopes are partitioned between coexisting phases is related to the free energy of the isotope exchange reaction, which depends on the strength of the iron bonds (Bigeleisen and Mayer 1947; Urey 1947). Phases that form stronger bonds with iron will be enriched in the heavy isotopes of iron at equilibrium. Because higher valence state and lower coordination tend to be associated with stronger, stiffer bonds, Fe^{3+} in low coordination usually has heavier Fe isotopic composition than Fe^{2+} or Fe^0 in high coordination. Equilibrium fractionation between phases is usually expressed using the α notation,

$$\alpha_{B-A} = R_B / R_A \tag{14}$$

or in Δ notation,

$$\Delta_{B-A} = \left(\delta_B - \delta_A\right)_{eq} \simeq 1000\left(\alpha_{B-A} - 1\right) \simeq 1000 \ln \alpha_{B-A} \tag{15}$$

The fractionation factors reflect differences in bond strength and can be related to the reduced partition function ratio β through,

$$\Delta_{B-A} = 1000\left(\ln\beta_B - \ln\beta_A\right) \tag{16}$$

β is the equilibrium fractionation factor between a given phase and the reference state of monoatomic vapor Fe. Knowing β-factors is advantageous relative to α values because equilibrium fractionation factors between any coexisting phases can be calculated from β-factors while α is only concerned with the fractionation between two specific phases. Note that the β-factor discussed here has nothing to do with the β exponent of the exponential mass fractionation law (Eqn. 3) or the β exponent of the diffusive law (Eqn. 11). The β-factors cannot directly be measured experimentally (Fe is only gaseous at high temperature), so one

relies on other methods such as ab initio calculation or, for iron, the synchrotron method of nuclear resonant inelastic X-ray scattering (NRIXS). Series expansions of the kinetic energy (Polyakov and Mineev 2000) or reduced partition function ratio (Dauphas et al. 2012) give a polynomial expression for the β-factors (and α values),

$$1000 \ln \beta = \frac{A_1}{T^2} + \frac{A_2}{T^4} + \frac{A_3}{T^6} \tag{17}$$

where A_1, A_2, and A_3 are constants that do not depend on T but vary between phases or chemical species. This expression will be used hereafter to summarize experimental and theoretical results. At high temperature (above ~400 °C), the higher order terms disappear and the formula is well approximated by the first term $1000 \ln \beta = A_1 / T^2$, or written as a function of the mean force constant of iron bonds, F (Herzfeld and Teller 1938; Bigeleisen and Mayer 1947),

$$1000 \ln \beta = 1000 \left(\frac{1}{m_{54}} - \frac{1}{m_{56}} \right) \frac{\hbar^2}{8k^2T^2} F = 2904 \frac{F}{T^2} \tag{18}$$

where m_{54} and m_{56} are the masses of isotopes ^{54}Fe and ^{56}Fe, $\hbar$ is the reduced Planck constant, k is the Boltzmann constant, and T is the temperature. Below, we review those different approaches and try to build a database of β-factors by cross-calibrating the different techniques.

Mineral–mineral and mineral–melt fractionation. To experimentally determine equilibrium fractionation factors involving solids, the main difficulty is that one must ensure that equilibrium is reached or one must correct the measurements for incomplete equilibration. For solids, equilibration most often involves volume diffusion, which can be particularly slow even at high temperature. To determine equilibrium fractionation factors between mineral–mineral or mineral–melt pairs, three strategies can be used.

The first one consists of running time series experiments. Two phases are juxtaposed and the temperature is usually increased to speed up diffusion kinetics. One runs several such experiments, retrieving the run products at different times. As time goes, the two phases approach equilibrium, at which point the isotopic fractionation between the coexisting phases should not change. The equilibrium fractionation factor is defined as the fractionation when longer experiment duration does not induce any change in the isotopic compositions of the coexisting phases.

The second approach consists of using an isotopic label to trace the equilibration process. If one starts with two phases on the terrestrial mass fractionation line in a three-isotope diagram δ^{57}Fe vs. δ^{56}Fe, the run products stay on this fractionation line as the reaction proceeds. However, if one dopes one of the reactants with a specific isotope, the two reactants will plot off the mass fraction line. As the reaction proceeds, they will move towards a mass-dependent isotopic fractionation relationship with each other, so one can tell that equilibrium has been achieved. This is known as the three-isotope technique.

The third approach consists of using natural samples for which the context (closure temperature) is well known and which have all characteristics (chemical, textural, isotopic) consistent with equilibrium. If these conditions are met, one can measure the isotopic compositions of coexisting phases. The virtue of this approach is that the timescales involved in natural systems are much longer than what can be achieved in the laboratory, but the temperature conditions are only indirectly known, so sample selection is critical.

Schuessler et al. (2007a) measured equilibrium iron isotopic fractionation between pyrrhotite (FeS) and peralkaline rhyolitic melt containing 62% Fe^{3+} and 38% Fe^{2+}. The authors investigated the exchange kinetics using an isotope doping experiment and ran a time series, allowing them to conclude that the fractionations at 840 and 1000 °C were both ~+0.35‰.

As discussed above, equilibrium iron isotopic fractionation is expected to scale as $1/T^2$, so that if the fractionation at 840 °C was +0.35‰, then the fractionation at 1000 °C should have been $0.35\times\left(840+273\right)^2/\left(1000+273\right)^2=0.27$‰. This is at the limit of detection and as a first approximation, the experimental results can be accounted for by a melt-pyrrhotite fractionation of $50\times10^4/T^2$ for the $^{56}Fe/^{54}Fe$ ratio. How much of this fractionation is due to different β-factors between Fe^{2+} in the rhyolite melt and pyrrhotite vs. the presence of large amount of Fe^{3+} in rhyolite melt is unknown.

Metal–silicate equilibrium isotopic fractionation has also been the subject of much work. Poitrasson et al. (2009) studied Fe isotopic fractionation between silicate and metal. By running a time series experiment, the authors were able to estimate the fractionation between ultramafic silicate liquid and molten Fe–Ni alloy at or near equilibrium to be +0.03 ± 0.04‰ at 2000 °C. Hin et al. (2012) also studied experimentally iron isotopic fractionation between liquid metal and silicate. They used a centrifuge piston cylinder to separate completely metal from silicate, so that their Fe isotopic compositions could be subsequently analyzed by MC-ICPMS. They ran a time series experiment and measured a metal–silicate fractionation factor of +0.01 ± 0.04 at 1300 °C. Shahar et al. (2015) reported measurements of liquid metal–silicate equilibrium isotopic fractionation in experiments that used the 3 isotope technique and found a fractionation of +0.08 ± 0.03‰ for $\delta^{56}Fe$ at 1650 °C. They also found that dissolving S in metal had an important effect of iron equilibrium isotopic fractionation, reaching ~+0.3‰ for 25% atomic S. To summarize, 3 studies have investigated experimentally the equilibrium fractionation factor between metal and silicate. Although the measurements were performed at different temperatures, some of these studies seem to disagree. Shahar et al. (2015) give a fractionation that is higher than that given by Hin et al. (2012) at a similar temperature. Further experiments will be needed to tell which value is correct.

Shahar et al. (2008) studied equilibrium fractionation between fayalite and magnetite using the 3-isotope equilibration technique at temperatures between 600 and 800 °C. They found significant equilibrium fractionation that can be described as $\delta^{56}Fe_{magnetite}-\delta^{56}Fe_{fayalite}=(0.20\pm0.016)\times10^6/T^2$. Equilibrium isotopic fractionation was also studied in natural samples for the mineral pair magnetite–pyroxene. Dauphas et al. (2004b, 2007b) studied quartz–pyroxene banded rocks from the island of Akilia (SW Greeland). These rocks are thought to be metamorphosed chemical sediments of BIF affinity. They were metamorphosed to a peak temperature of 750 °C (granulite facies conditions). The magnetite/pyroxene fractionation documented in these rocks is +0.25 ± 0.08‰ and was interpreted to reflect equilibrium fractionation between these two minerals (Dauphas et al. 2004b, 2007b).

Sossi and O'Neill (2016) used an elegant method to measure equilibrium fractionation between minerals. They equilibrated in piston cylinders at 1073 K and 1 GPa the fluid phase $FeCl_2.4H_2O$ with several minerals: almandine (Fe-bearing garnet), ilmenite, fayalite (Fe-bearing olivine), chromite, hercynite (Fe-bearing spinel) and magnetite. The fluid promotes the formation of large crystals and speeds up mineral equilibration. By taking the differences between pairs of mineral–fluid equilibration experiments, Sossi and O'Neill (2016) were able to estimate mineral–mineral equilibrium fractionation factors, which are difficult to determine otherwise.

Fluid–mineral and fluid–fluid fractionations. Establishing equilibrium fractionation factors at high temperature is fraught with difficulties, as equilibration is difficult to achieve and kinetic isotope effects can also influence the net fractionation. Measuring those values at low temperature in aqueous systems is even more challenging as diffusion is very slow and the exchange process is probably governed by dissolution–precipitation reactions, which may be associated with kinetic isotope effects. Nevertheless, significant work has been done, especially with regard to iron oxides and Fe^{2+} and Fe^{3+} dissolved in water.

Welch et al. (2003) tackled an important and difficult experimental problem, which is to determine the equilibrium fractionation factor between aqueous Fe(II) and Fe(III). The difficulty stems from the fact that those two species are mixed in solution and that to measure how iron isotopes are fractionated between them, one has to separate one from the other, which Welch et al. (2003) achieved by precipitating Fe(III). The difficulties associated with such precipitation is to ensure that no kinetic isotope effects are present during precipitation and that Fe(II) does not exchange isotopically with $Fe(III)_{aq}$ as the latter is precipitating, or one must account and correct for these effects. Two measurements were performed at 0 and 22 °C that yielded an equilibrium fractionation factor for the $^{56}Fe/^{54}Fe$ ratio between aqueous Fe(III) and Fe(II) that can be expressed as $0.334 \times 10^6 / T^2 - 0.88$. The authors calculated the speciation of the Fe in solution and found that, for the compositions considered, they would be hexaaqua-coordinated, i.e., $[FeII(H_2O)_6]^{2+}$, $[FeIII(H_2O)_6]^{3+}$ and $[FeIII(H_2O)_5(OH)]^{2+}$

Much work has also been done on equilibrium isotopic fractionation factors between aqueous species and minerals. Skulan et al. (2002) found that the isotopic fractionation between $[FeIII(H_2O)_6]^{3+}$ and hematite depended on the rate of precipitation of hematite and by extrapolating the experimental results to a precipitation rate of zero, they inferred that the equilibrium fractionation between aqueous Fe(III) and hematite was $-0.1 \pm 0.2‰$ for the $^{56}Fe/^{54}Fe$ ratio at 98 °C. Saunier et al. (2011) measured equilibrium fractionation between hematite and ferrous/ferric chloride iron complexes under hydrothermal conditions. When the fluid is dominated by Fe(III) chloride complexes, the isotopic fractionation between fluid and hematite is small: $+0.01 \pm 0.05‰$ for the $^{56}Fe/^{54}Fe$ ratio at 300 °C. When Fe(II) chloride complexes ($FeCl_2$ and $FeCl^+$) are dominant in the fluid, the fractionations are larger, reaching $-0.36 \pm 0.10‰$ at 300 °C and $+0.10 \pm 0.12‰$ at 450 °C. The experiments of Skulan et al. (2002) and Saunier et al. (2011) were performed at different temperatures and correspond to different fluid speciations, but Saunier et al. (2011) pointed out that they may be difficult to reconcile with each other based on ab initio calculations that can be used to account for differences in the experimental setups. Wu et al. (2010) evaluated the influences of pH, presence of dissolved Si, and $Fe(II)_{aq}$/hematite ratio on $Fe(II)_{aq}$-hematite surface iron isotopic fractionation.

Wu et al. (2011) investigated the equilibrium fractionation between Fe(III)-bearing ferrihydrite (hydrous ferric oxide) and aqueous $Fe(II)_{aq}$. They obtained an equilibrium fractionation factor of $+3.2 \pm 0.1‰$ for the $^{56}Fe/^{54}Fe$ ratio at 25 °C. Wu et al. (2011, 2012a) found that this fractionation was also influenced by the presence of silica. Beard et al. (2010), Friedrich et al. (2014a), and Reddy et al. (2015) reported a much smaller equilibrium fractionation factor of $+1.05 \pm 0.08‰$ for the $^{56}Fe/^{54}Fe$ ratio at 22 °C between goethite and Fe(II). The latter value is puzzling because it is not clear what in the crystal chemistry of goethite would impart and equilibrium fractionation factor of ~+2‰ between hematite or ferrihydrite on the one hand, and goethite on the other hand.

Friedrich et al. (2014b) used the three isotope technique to estimate the extent of equilibrium fractionation between $Fe(II)_{aq}$ and magnetite and obtained a value of $-1.56 \pm 0.20‰$ at 22 °C for the $^{56}Fe/^{54}Fe$ ratio.

Wiesli et al. (2004) measured the fractionation between Fe(II) and siderite. Siderite precipitation induced iron isotopic fractionation that followed a Rayleigh distillation model, from which they could estimate an equilibrium fractionation factor between aqueous Fe(II) and siderite of $+0.48 \pm 0.22‰$ at 20 °C. The extent to which these experiments could have been affected by kinetic effects is unclear.

Dideriksen et al. (2008) measured the equilibrium fractionation factor between aqueous Fe(III) and the siderophore complex Fe(IIII) desferrioxamine B. It is an important fractionation for the modern marine iron cycle as much of iron dissolved in seawater and accessible as

a nutrient is in the form of siderophore complexes. They measured what they inferred to be an equilibrium fractionation factor of $+0.60 \pm 0.15‰$ between the siderophore complex and inorganic Fe(III) species Fe^{3+}_{aq} and $Fe(OH)^{2+}$ (those two species are not expected to be significantly fractionated relative to each other).

Guilbaud et al. (2011a) estimated the equilibrium fractionation factor between Fe(II)$_{aq}$ and mackinawite (FeS) at 25 and 2 °C. They obtained fractionations of -0.52 ± 0.16 and $-0.33 \pm 0.12‰$ at 2 and 25 °C, respectively. They used the three isotope method to correct for incomplete fluid–mineral equilibration. Wu et al. (2012b) studied the same system and obtained a similar fractionation of $-0.32 \pm 0.29‰$ for the $^{56}Fe/^{54}Fe$ ratio between $Fe(II)_{aq}$ and mackinawite at 20 °C, indicating that the results are reproducible.

Syverson et al. (2014) investigated iron isotopic fractionation between vapor, halite, and liquid for application to seafloor hydrothermal vents, where phase separation can take place. The experiments were conducted at relatively high temperature (~420 to 470 °C) and the measured fractionations were small, not exceeding 0.1‰ for the most part. Hill and Schauble (2008) measured and predicted theoretically equilibrium iron isotopic fractionation in ferric aquo-chloro complexes. They equilibrated iron dissolved in aqueous solution of various chlorinities with $FeCl_4^-$ dissolved in immiscible diethyl ether. The immiscible diethyl ether played the role of a spectator phase that allowed them to investigate how iron coordination with chlorine affects its equilibrium isotope fractionation factor. At low chlorinity, the dominant species in the aqueous solution is $FeCl^{2+}$. At high chlorinity, the two dominant phases are $FeCl^{2+}$ and $FeCl_3$. Hill and Schauble (2008) found that the fractionation for $\delta^{56}Fe$ between $FeCl^{2+}$ in aqueous medium and $FeCl_4^-$ in ether is ~0.8‰ while the values goes down to near zero at high chlorinity, when the dominant species in the aqueous medium is $FeCl_3$.

Beta factors from NRIXS and ab initio approaches. The experimental methods outlined above can only provide relative fractionation factors, meaning differences in iron isotopic compositions of coexisting phases at equilibrium. Two approaches give access to absolute β-factors (or reduced partition function ratios).

The first approach is computational and it involves calculations grounded in physical chemistry of the vibration modes of molecules or minerals. Discussing the details of those approaches and their uncertainties is beyond the scope of the present review, so we will focus on discussing the modeling results. The reader is referred to the review paper of Schauble (2004), which provides a comprehensive introduction to this topic. A wide variety of phases have been calculated with this approach. To give a more palatable overview of the work done, we have summarized the results of those calculations in Table 1. Sometimes, the β-factor is only given at one or a few temperature values. In those cases, we used a similar approach to Dauphas et al. (2012) to calculate the coefficients of the polynomial that gives the temperature dependence of the β-factor. The β-factor can be written as a function of the force constant of iron bonds as,

$$1000 \ln \beta = B_1 \frac{F}{T^2} - B_2 \frac{F^2}{T^4} + B_3 \frac{F^3}{T^6} \quad (19)$$

where $B_1 = 2904\ \mathrm{m.N^{-1}.K^2}$ is a true constant and the two other coefficients B_2 and B_3 depend on the shape of the phonon density of states of the iron sublattice (PDOS; energy distribution of lattice vibrations; through statistical mechanics, this distribution relates to the thermodynamics of the mineral). For a Debye PDOS, $B_2 = 37538\ \mathrm{m^2.N^{-2}.K^4}$. In practice, the coefficients vary little from phase to phase or their variations have little influence on the calculated β-factors because these are higher order terms. To express the temperature dependence of β given a few T values, we can write,

Table 1. Iron β-factors ($^{56}Fe/^{54}Fe$) from ab-initio and NRIXS studies (high-*P* phases are not included).

			$1000 \times \ln\beta\ (^{56}Fe/^{54}Fe) = A_1/T^2 + A_2/T^4 + A_3/T^6$			$10^3 \ln\beta$				
Phase	**Note**	**Method**	A_1 ($\times 10^6$)	A_2 ($\times 10^9$)	A_3 ($\times 10^{12}$)	**22 °C**	**100 °C**	**500 °C**	**1200 °C**	**References**
Fe(gas)			0	0	0	0.0	0.0	0.00	0.00	
Magnetite		NRIXS	0.64943	−3.2094	2.76200	7.0	4.5	1.08	0.30	Polyakov et al. (2007)
FeO (Wüstite)		NRIXS	0.45569	−1.5357	9.89950	5.0	3.2	0.76	0.21	Polyakov et al. (2007)
Troilite		NRIXS	0.29735	−0.6693	0.30274	3.3	2.1	0.50	0.14	Polyakov et al. (2007)
Fe_3S		NRIXS	0.32109	−0.5830	0.18086	3.6	2.3	0.54	0.15	Polyakov et al. (2007)
Chalcopyrite		NRIXS	0.48888	−1.7631	0.95290	5.4	3.4	0.81	0.22	Polyakov and Soultanov (2011)
Magnetite		NRIXS	0.65756	−3.0366		7.1	4.6	1.09	0.30	Dauphas et al. (2012)
Troilite		NRIXS	0.29101	−0.6353		3.3	2.1	0.49	0.13	Dauphas et al. (2012)
Fe_3S		NRIXS	0.34150	−0.7702		3.8	2.4	0.57	0.16	Dauphas et al. (2012)
Chalcopyrite		NRIXS	0.41654	−1.2068		4.6	2.9	0.69	0.19	Dauphas et al. (2012)
Orthoenstatite		NRIXS	0.50403	−2.0501		5.5	3.5	0.84	0.23	Dauphas et al. (2012)
Hematite		NRIXS	0.69649	−3.2728		7.6	4.8	1.16	0.32	Dauphas et al. (2012)
$(Mg_{0.75}Fe_{0.25})O$		NRIXS	0.51354	−1.7475		5.7	3.6	0.85	0.24	Dauphas et al. (2012)
α–Fe (bcc)		NRIXS	0.49970	−1.1424		5.6	3.5	0.83	0.23	Dauphas et al. (2012)
α–Fe (bcc)		NRIXS	0.52781	−1.2747		5.9	3.7	0.88	0.24	Dauphas et al. (2012)
$\alpha–Fe_{0.525}Cr_{0.475}$ (bcc)		NRIXS	0.44507	−0.8841		5.0	3.2	0.74	0.20	Dauphas et al. (2012)
$\sigma–Fe_{0.525}Cr_{0.475}$		NRIXS	0.44792	−0.9808		5.0	3.2	0.75	0.21	Dauphas et al. (2012)
γ–Fe (fcc) 80nm particles		NRIXS	0.39657	−0.6982		4.5	2.8	0.66	0.18	Dauphas et al. (2012)

			$1000 \times \ln\beta\ (^{56}Fe/^{54}Fe) = A_1/T^2 + A_2/T^4 + A_3/T^6$			$10^3 \ln\beta$				
Phase	**Note**	**Method**	A_1 ($\times 10^6$)	A_2 ($\times 10^9$)	A_3 ($\times 10^{12}$)	**22 °C**	**100 °C**	**500 °C**	**1200 °C**	**References**
Goethite		NRIXS	0.76590	−5.3010	93.18000	8.2	5.3	1.27	0.35	Blanchard et al. (2015)
H–Jarosite		NRIXS	0.79790	−5.4750	72.57000	8.5	5.5	1.32	0.37	Blanchard et al. (2015)
K–Jarosite		NRIXS	0.82870	−6.2890	117.30000	8.9	5.7	1.37	0.38	Blanchard et al. (2015)
Olivine		NRIXS	0.56100	−2.5900	30.40000	6.1	3.9	0.93	0.26	Dauphas et al. (2014)
Fe^{2+} in basalt, andesite, dacite		NRIXS	0.56990	−3.7024	66.68200	6.2	3.9	0.94	0.26	Dauphas et al. (2014)
Fe^{3+} in basalt, andesite, dacite		NRIXS	1.00159	−8.9240	172.49790	10.6	6.8	1.65	0.46	Dauphas et al. (2014)
Fe^{2+} in rhyolite		NRIXS	0.68297	−5.3311	82.01470	7.3	4.7	1.13	0.31	Dauphas et al. (2014)
Fe^{3+} in rhyolite		NRIXS	1.10381	−9.8285	173.90380	11.6	7.5	1.82	0.51	Dauphas et al. (2014)
Fe^{2+} in MgFeAl spinel		NRIXS	0.54341	−3.7432	75.89850	5.9	3.7	0.90	0.25	Roskosz et al. (2015)
Fe^{3+} in MgFeAl spinel		NRIXS	0.86294	−6.3164	102.77160	9.2	5.9	1.43	0.40	Roskosz et al. (2015)
Troilite	*	NRIXS	0.27674	−0.5821	3.47588	3.1	2.0	0.46	0.13	Krawczynski et al. (2014)
γ–Fe–Ni (fcc)	*	NRIXS	0.41939	−1.3368	12.09765	4.7	2.9	0.70	0.19	Krawczynski et al. (2014)
Ilmenite	*	NRIXS	0.44507	−1.5054	14.45849	4.9	3.1	0.74	0.20	Williams et al. (2016)
Pyrite		ab initio	0.82913	−3.2161	17.88867	9.1	5.8	1.38	0.38	Blanchard et al. (2009)
Hematite		ab initio	0.66267	−3.1255	24.75800	7.2	4.6	1.10	0.30	Blanchard et al. (2009)
Siderite		ab initio	0.38180	−1.5765	24.56000	4.2	2.7	0.63	0.18	Blanchard et al. (2009)
Goethite		ab initio	0.68320	−3.9026	45.41467	7.4	4.7	1.13	0.31	Blanchard et al. (2015)
Hematite	*	ab initio	0.67790	−3.4926	51.09130	7.4	4.7	1.12	0.31	Rustad and Dixon (2009)

			$1000 \times \ln \beta\ (^{56}Fe/^{54}Fe) = A_1/T^2 + A_2/T^4 + A_3/T^6$			$10^3 \ln \beta$				
Phase	**Note**	**Method**	A_1 (×10^6)	A_2 (×10^9)	A_3 (×10^{12})	**22 °C**	**100 °C**	**500 °C**	**1200 °C**	**References**
Fe^{3+}_{aq}	*	ab initio	0.76983	−4.5128	75.25849	8.4	5.3	1.28	0.35	Rustad and Dixon (2009)
Fe^{2+}_{aq}	*	ab initio	0.46976	−1.6877	17.32170	5.2	3.3	0.78	0.22	Rustad and Dixon (2009)
$[FeII(CN)_6]^{4-}$	*	ab initio	1.72962	−22.7506	850.21972	18.1	11.6	2.83	0.79	Schauble et al. (2004)
$[FeIII(CN)_6]^{3-}$	*	ab initio	1.36547	−14.1740	417.86430	14.4	9.2	2.25	0.63	Schauble et al. (2004)
$[FeIIIBr_4]^-$	*	ab initio	0.59811	−2.7188	35.08997	6.6	4.2	0.99	0.28	Schauble et al. (2004)
α-Fe (bcc)	*	ab initio	0.49377	−1.8531	19.74768	5.5	3.5	0.82	0.23	Schauble et al. (2004)
Fe^{3+}_{aq}	*	ab initio	1.10968	−9.3586	224.09873	11.8	7.6	1.83	0.51	Schauble et al. (2004)
Fe^{2+}_{aq}	*	ab initio	0.57054	−2.4741	30.46468	6.3	4.0	0.95	0.26	Schauble et al. (2004)
$[FeIII(H_2O)_4Cl_2]^+$	*	ab initio	0.83044	−5.2414	93.93647	9.0	5.7	1.38	0.38	Schauble et al. (2004)
$[FeIII(H_2O)_3Cl_3]^0$	*	ab initio	0.72793	−4.0275	63.27410	7.9	5.0	1.21	0.33	Schauble et al. (2004)
$[FeIIICl_4]^-$	*	ab initio	0.66964	−3.4080	49.24720	7.3	4.7	1.11	0.31	Schauble et al. (2004)
$[FeIICl_4]^{2-}$	*	ab initio	0.36518	−1.0135	7.98695	4.1	2.6	0.61	0.17	Schauble et al. (2004)
$[FeIIICl_6]^{3-}$	*	ab initio	0.35579	−0.9626	7.39929	4.0	2.5	0.59	0.16	Schauble et al. (2004)
Fe^{3+}_{aq}	*	ab initio	0.88735	−5.9850	114.63554	9.6	6.1	1.47	0.41	Anbar et al. (2005)
Fe^{2+}_{aq}	*	ab initio	0.62685	−2.9874	40.43608	6.9	4.4	1.04	0.29	Anbar et al. (2005)
$[FeII(H_2O)_6]^{2+}$		ab initio	0.49264	−2.6344	23.86742	5.3	3.4	0.82	0.23	Ottonello and Zuccolini (2009)
$[FeII(H_2O)_{18}]^{2+}$		ab initio	0.52897	−3.9712	60.78421	5.6	3.6	0.87	0.24	Ottonello and Zuccolini (2009)

			$1000 \times \ln\beta\ (^{56}Fe/^{54}Fe) = A_1/T^2 + A_2/T^4 + A_3/T^6$			$10^3 \ln\beta$				
Phase	**Note**	**Method**	A_1 (×10^6)	A_2 (×10^9)	A_3 (×10^{12})	**22 °C**	**100 °C**	**500 °C**	**1200 °C**	**References**
$[FeII(H_2O)_5(OH)]^+$		ab initio	0.56994	−4.8733	65.98762	6.0	3.9	0.94	0.26	Ottonello and Zuccolini (2009)
$[FeII(H_2O)_4(OH)]^+$		ab initio	0.55521	−4.8825	61.46983	5.8	3.8	0.92	0.25	Ottonello and Zuccolini (2009)
$[FeII(H_2O)_4(OH)_2]^0$		ab initio	0.64249	−6.5575	96.42366	6.7	4.3	1.06	0.29	Ottonello and Zuccolini (2009)
$[FeII(H_2O)_2(OH)_2]^0$		ab initio	0.65228	−7.4150	105.04000	6.7	4.3	1.07	0.30	Ottonello and Zuccolini (2009)
$[FeII(H_2O)_3(OH)_3]^-$		ab initio	0.71362	−7.4312	96.50000	7.4	4.8	1.17	0.33	Ottonello and Zuccolini (2009)
$[FeII(OH)_3]^-$		ab initio	0.70670	−7.4079	88.35000	7.3	4.7	1.16	0.32	Ottonello and Zuccolini (2009)
$[FeIII(H_2O)_6]^{3+}$		ab initio	0.84274	−6.8500	84.66667	8.9	5.7	1.39	0.39	Ottonello and Zuccolini (2009)
$[FeIII(H_2O)_5(OH)]^{2+}$		ab initio	0.93316	−11.6355	180.31175	9.5	6.2	1.53	0.43	Ottonello and Zuccolini (2009)
$[FeIII(H_2O)_4(OH)]^{2+}$		ab initio	0.96969	−12.4540	196.00000	9.8	6.4	1.59	0.44	Ottonello and Zuccolini (2009)
$[FeIII(H_2O)_4(OH)_2]^+$		ab initio	0.96685	−12.8868	202.29194	9.7	6.4	1.58	0.44	Ottonello and Zuccolini (2009)
$[FeIII(H_2O)_3(OH)_2]^+$		ab initio	1.00359	−13.2628	202.20000	10.1	6.6	1.64	0.46	Ottonello and Zuccolini (2009)
$[FeIII(H_2O)_3(OH)_3]^0$		ab initio	0.96638	−11.5614	167.14000	9.8	6.4	1.59	0.44	Ottonello and Zuccolini (2009)
$[FeIII(OH)_3]^0$		ab initio	1.01056	−15.3823	237.31089	9.9	6.6	1.65	0.46	Ottonello and Zuccolini (2009)
$[FeIII(H_2O)_2(OH)_4]^-$		ab initio	1.00662	−11.0661	145.07086	10.3	6.7	1.65	0.46	Ottonello and Zuccolini (2009)
$[FeIII(OH)_4]^-$		ab initio	1.06690	−11.8236	147.36411	10.9	7.1	1.75	0.49	Ottonello and Zuccolini (2009)
$[FeIII(H_2O)_6]^{3+}$	*	ab initio	0.87065	−5.7610	108.23681	9.4	6.0	1.44	0.40	Hill and Schauble (2008)
$[FeIIICl(H_2O)_5]^{2+}$	*	ab initio	0.78359	−4.6664	78.90463	8.5	5.4	1.30	0.36	Hill and Schauble (2008)
$FeIIICl(H_2O)_4]^+$	*	ab initio	0.73282	−4.0814	64.54233	8.0	5.1	1.21	0.34	Hill and Schauble (2008)
$FeCl_3(H_2O)_3]^0$ octahedral fac	*	ab initio	0.64815	−3.1928	44.65530	7.1	4.5	1.08	0.30	Hill and Schauble (2008)
$FeCl_3(H_2O)_3]^0$ octahedral mer	*	ab initio	0.66164	−3.3270	47.50126	7.2	4.6	1.10	0.30	Hill and Schauble (2008)

			$1000 \times \ln \beta\ (^{56}Fe/^{54}Fe) = A_1/T^2 + A_2/T^4 + A_3/T^6$			$10^3 \ln \beta$				
Phase	**Note**	**Method**	A_1 ($\times 10^6$)	A_2 ($\times 10^9$)	A_3 ($\times 10^{12}$)	**22 °C**	**100 °C**	**500 °C**	**1200 °C**	**References**
$FeCl_3(H_2O)_3]^0$ trigonal bipyramidal	*	ab initio	0.70194	−3.7447	56.72098	7.7	4.9	1.16	0.32	Hill and Schauble (2008)
$[FeCl_4]^-$	*	ab initio	0.67188	−3.4308	49.74153	7.3	4.7	1.11	0.31	Hill and Schauble (2008)
$[FeCl_5(H_2O)]^{2-}$	*	ab initio	0.45918	−1.6025	15.87837	5.1	3.2	0.76	0.21	Hill and Schauble (2008)
$[FeCl_5]^{2-}$	*	ab initio	0.47729	−1.7313	17.83183	5.3	3.3	0.79	0.22	Hill and Schauble (2008)
$[FeCl_6]^{3-}$	*	ab initio	0.32724	−0.8139	5.74701	3.7	2.3	0.55	0.15	Hill and Schauble (2008)
$[Fe(H_2O)_6]^{2+}$	*	ab initio	0.53168	−2.1484	24.64819	5.9	3.7	0.88	0.24	Hill and Schauble (2008)
$[Fe(H_2O)_6]^{3+} \cdot 12(H_2O)$	*	ab initio	0.94089	−6.7281	136.60294	10.1	6.5	1.56	0.43	Hill and Schauble (2008)
$[FeCl_4]^- .12(H_2O)$	*	ab initio	0.68395	−3.5552	52.47019	7.5	4.7	1.13	0.31	Hill and Schauble (2008)
$[FeIII(H_2O)_6]^{3+}$	*	ab initio	0.80447	−4.9193	85.42416	8.7	5.6	1.33	0.37	Domagal–Goldman and Kubicki (2008)
$[FeII(H_2O)_6]^{2+}$	*	ab initio	0.53143	−2.1466	24.61976	5.9	3.7	0.88	0.24	Domagal–Goldman and Kubicki (2008)
$[FeIII(O_x)_3]^{3-}$	*	ab initio	0.73720	−4.1304	65.71121	8.0	5.1	1.22	0.34	Domagal–Goldman and Kubicki (2008)
$[FeII(O_x)_3]^{4-}$	*	ab initio	0.45825	−1.5959	15.78170	5.1	3.2	0.76	0.21	Domagal–Goldman and Kubicki (2008)
$[FeIII(Cat)_3]^{3-}$	*	ab initio	0.67939	−3.5088	51.46783	7.4	4.7	1.13	0.31	Domagal–Goldman and Kubicki (2008)
$[FeII(Cat)_3]^{4-}$	*	ab initio	0.41094	−1.2835	11.38358	4.6	2.9	0.68	0.19	Domagal–Goldman and Kubicki (2008)
$FeII(H_2O)_6^{2+}$	*	ab initio	0.47192	−1.6927	17.23970	5.2	3.3	0.78		Fujii et al. (2014)
$FeIICl(H_2O)^{5+}$	*	ab initio	0.45038	−1.5417	14.98583	5.0	3.2	0.75		Fujii et al. (2014)
$FeIICl_2(H_2O)_4$	*	ab initio	0.42797	−1.3921	12.85772	4.7	3.0	0.71		Fujii et al. (2014)
$FeIISO_4(H_2O)_5$	*	ab initio	0.50398	−1.9310	21.01328	5.6	3.5	0.84		Fujii et al. (2014)

			$1000 \times \ln\beta\ (^{56}Fe/^{54}Fe) = A_1/T^2 + A_2/T^4 + A_3/T^6$			$10^3 \ln\beta$				
Phase	**Note**	**Method**	A_1 ($\times 10^6$)	A_2 ($\times 10^9$)	A_3 ($\times 10^{12}$)	**22 °C**	**100 °C**	**500 °C**	**1200 °C**	**References**
$FeIIOH(H_2O)^{5+}$	*	ab initio	0.51383	−2.0075	22.27952	5.7	3.6	0.85		Fujii et al. (2014)
$FeII(OH)_2(H_2O)_4$	*	ab initio	0.50772	−1.9608	21.52108	5.6	3.6	0.84		Fujii et al. (2014)
$FeII_2(OH)_6^{2-}$	*	ab initio	0.50268	−1.9206	20.83898	5.5	3.5	0.84		Fujii et al. (2014)
$FeIIHCO_3(H_2O)^{4+}$	*	ab initio	0.48936	−1.8202	19.22527	5.4	3.4	0.81		Fujii et al. (2014)
$FeIICO_3(H_2O)_4$	*	ab initio	0.54274	−2.2392	26.23650	6.0	3.8	0.90		Fujii et al. (2014)
$FeIIHS(H_2O)^{5+}$	*	ab initio	0.40735	−1.2612	11.08847	4.5	2.9	0.68		Fujii et al. (2014)
$FeII(HS)_2(H_2O)_4$	*	ab initio	0.36475	−1.0112	7.96105	4.1	2.6	0.61		Fujii et al. (2014)
$FeII_2S_2(H_2O)_4$	*	ab initio	0.44661	−1.5160	14.61071	4.9	3.1	0.74		Fujii et al. (2014)
$FeIIH_2PO_4(H_2O)^{5+}$	*	ab initio	0.49486	−1.8613	19.88031	5.5	3.5	0.82		Fujii et al. (2014)
$FeIIHPO_4(H_2O)_5$	*	ab initio	0.54965	−2.2965	27.24806	6.0	3.8	0.91		Fujii et al. (2014)
$FeIIH_4(PO_4)_2(H_2O)_4$	*	ab initio	0.49161	−1.8369	19.48944	5.4	3.4	0.82		Fujii et al. (2014)
$FeIIH_3(PO_4)_2(H_2O)^{4-}$	*	ab initio	0.48697	−1.8027	18.95237	5.4	3.4	0.81		Fujii et al. (2014)
$FeIIH(cit)(H_2O)_3$	*	ab initio	0.48664	−1.8000	18.90732	5.4	3.4	0.81		Fujii et al. (2014)
$FeII(cit)(H_2O)^{3-}$	*	ab initio	0.48896	−1.8174	19.18295	5.4	3.4	0.81		Fujii et al. (2014)
$FeIIH(cit)_2^{3-}$	*	ab initio	0.42467	−1.3707	12.56175	4.7	3.0	0.71		Fujii et al. (2014)
$FeII(cit)_2^{4-}$	*	ab initio	0.35424	−0.9537	7.29000	4.0	2.5	0.59		Fujii et al. (2014)
$FeII(cit)_2OH^{5-}$	*	ab initio	0.62871	−3.0047	40.77936	6.9	4.4	1.04		Fujii et al. (2014)
$FeIII(H_2O)_6^{3+}$	*	ab initio	0.76263	−4.4209	72.77484	8.3	5.3	1.26		Fujii et al. (2014)
$FeIIICl(H_2O)_5^{2+}$	*	ab initio	0.68879	−3.6060	53.60719	7.5	4.8	1.14		Fujii et al. (2014)

			$1000\times\ln\beta\ (^{56}Fe/^{54}Fe) = A_1/T^2+A_2/T^4+A_3/T^6$			$10^3\ln\beta$				
Phase	**Note**	**Method**	A_1 ($\times10^6$)	A_2 ($\times10^9$)	A_3 ($\times10^{12}$)	**22 °C**	**100 °C**	**500 °C**	**1200 °C**	**References**
$FeIIISO_4(H_2O)^{5+}$	*	ab initio	0.80033	–4.8696	84.15302	8.7	5.5	1.33		Fujii et al. (2014)
$FeIIIOH(H_2O)_5^{2+}$	*	ab initio	0.86462	–5.6852	106.21067	9.3	6.0	1.43		Fujii et al. (2014)
$FeIII(OH)_2(H_2O)^{4+}$	*	ab initio	0.89166	–6.0474	116.55276	9.6	6.1	1.48		Fujii et al. (2014)
$FeIII(OH)_3(H_2O)_3$	*	ab initio	0.89990	–6.1582	119.72347	9.7	6.2	1.49		Fujii et al. (2014)
$FeIIIHCO_3(H_2O)_4^{2+}$	*	ab initio	0.73461	–4.1018	65.03534	8.0	5.1	1.22		Fujii et al. (2014)
$FeIIICO_3(H_2O)^{4+}$	*	ab initio	0.74190	–4.1840	67.01201	8.1	5.1	1.23		Fujii et al. (2014)
$FeIIIH_3PO_4(H_2O)_5^{3+}$	*	ab initio	0.79978	–4.8619	83.92847	8.7	5.5	1.32		Fujii et al. (2014)
$FeIIIH_2PO_4(H_2O)_5^{2+}$	*	ab initio	0.81651	–5.0680	89.33434	8.8	5.6	1.35		Fujii et al. (2014)
$FeIIIHPO_4(H_2O)^{5+}$	*	ab initio	0.86912	–5.7426	107.76645	9.4	6.0	1.44		Fujii et al. (2014)
$FeIIIH_5(PO_4)_2(H_2O)_4^{2+}$	*	ab initio	0.81892	–5.0977	90.11474	8.9	5.7	1.36		Fujii et al. (2014)
$FeIIIH_4(PO_4)_2(H_2O)^{4+}$	*	ab initio	0.82966	–5.2326	93.72130	9.0	5.7	1.37		Fujii et al. (2014)
$FeIIIH_3(PO_4)_2(H_2O)_4$	*	ab initio	0.84821	–5.4693	100.15822	9.2	5.8	1.40		Fujii et al. (2014)
$FeIIIH_7(PO_4)_3(H_2O)^{3+}$	*	ab initio	0.82181	–5.1337	91.06875	8.9	5.7	1.36		Fujii et al. (2014)
$FeIIIH_6(PO_4)_3(H_2O)_3$	*	ab initio	0.85591	–5.5683	102.86933	9.2	5.9	1.42		Fujii et al. (2014)
$FeIII(cit)(H_2O)_3$	*	ab initio	0.84780	–5.4635	99.98582	9.2	5.8	1.40		Fujii et al. (2014)
$FeIII(cit)OH(H_2O)^{2-}$	*	ab initio	0.81552	–5.0560	89.02412	8.8	5.6	1.35		Fujii et al. (2014)
$FeIIIH(cit)_2^{2-}$	*	ab initio	0.80178	–4.8859	84.54333	8.7	5.5	1.33		Fujii et al. (2014)
$FeIII(cit)_2^{3-}$	*	ab initio	0.68018	–3.5161	51.61026	7.4	4.7	1.13		Fujii et al. (2014)
$FeIII(cit)_2OH^{4-}$	*	ab initio	0.65511	–3.2623	46.13236	7.2	4.6	1.09		Fujii et al. (2014)

*For studies that report equilibrium fractionation at just a few temperatures or just give a force constant, the coefficients were calculated by writing (with $x=A_1/T^2$):
$1000\times\ln\beta\ (^{56}Fe/^{54}Fe) = x-7.6\times10^{-3}x^2+164\times10^{-6}x^3$ where the coefficients were determined by regressing A_2 vs A_1^2 and A^3 vs A_1^3 for the data that have all three coefficients reported.

$$1000\ln\beta = \frac{A_1}{T^2} + C\frac{A_1^2}{T^4} + D\frac{A_1^3}{T^6} \quad (20)$$

The coefficients C and D were obtained by regressing A_2 vs. A_1^2 and A_3 vs. A_1^3 from Equation (17), for the phases for which the full polynomial expansion was provided in either NRIXS or ab initio studies. The one-parameter formula to calculate the temperature dependence of $1000\ln\beta$ given as little as one data point is (Fig. 5 ; note that a similar approach can be used for other isotope systems),

$$1000\ln\beta = \frac{A_1}{T^2} - 7.6\times10^{-3}\frac{A_1^2}{T^4} + 164\times10^{-6}\frac{A_1^3}{T^6} \quad (21)$$

Much of the early work to calculate β-factors focused on aqueous species. With modern softwares, calculating β-factors is relatively straightforward and a significant fraction of the work involves validating the calculations by comparing the results with existing spectroscopic data and equilibration experiments. Not all studies do that and the reader should exercise caution in using indiscriminately calculated β-factors from the litterature. Schauble et al. (2001) calculated the β-factors of $[FeII(CN)_6]^{4-}$, $[FeIII(CN)_6]^{3-}$, $[FeIII(H_2O)_6]^{3+}$,

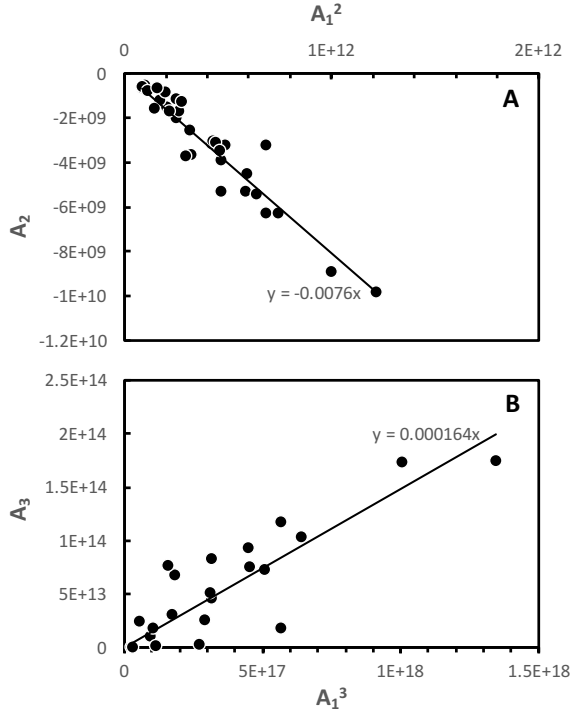

Figure 5. Correlations between the coefficients of the polynomial expansion of β equilibrium fractionation factors. The values of the coefficients of the temperature expansion to the 3rd order are available for some phases from NRIXS and ab initio studies; $1000\ln\beta = A_1/T^2 + A_2/T^4 + A_3/T^6$. To a good approximation (see Dauphas et al. 2012 for a theoretical justification), this can be written as $1000\ln\beta = A_1/T^2 + CA_1^2/T^4 + D\,A_1^3/T^6$ (Eqn. 20), with C and D constant. The values of C and D are calculated by regressing A_2 vs. A_1^2 and A_2 vs. A_1^3, respectively.

$[FeIII(H_2O)_4Cl_2]^+$, $[FeIII(H_2O)_3Cl_3]^0$, $[FeIIICl_4]^-$, $[FeIIIBr_4]^-$, $[FeII(H_2O)_6]^{2+}$, α-Fe metal, $[FeIICl_4]^{2-}$, $[FeIIICl_6]^{3-}$. Anbar et al. (2005) and Jarzecki et al. (2004) calculated the β-factors of $[FeIII(H_2O)_6]^{3+}$ and $[FeII(H_2O)_6]^{2+}$, paying attention to the treatment of the solvation shell. Ottonello and Zuccolini (2009) also studied those two important species as well as many other hydrous complexes, $[Fe(II)(H_2O)_{18}]^{2+}$, $[Fe(II)(H_2O)_5(OH)]^+$, $[Fe(II)(H_2O)_4(OH)]^+$, $[Fe(II)(H_2O)_4(OH)_2]^0$, $[Fe(II)(H_2O)_2(OH)_2]^0$, $[Fe(II)(H_2O)_3(OH)_3]^-$, $[Fe(II)(OH)_3]^-$, $[Fe(III)(H_2O)_6]^{3+}$, $[Fe(III)(H_2O)_5(OH)]^{2+}$, $[Fe(III)(H_2O)(OH)]^{2+}$, $[Fe(III)(H_2O)_4(OH)_2]^+$, $[Fe(III)(H_2O)_3(OH)_2]^+$, $[Fe(III)(H_2O)_3(OH)_3]^0$, $[Fe(III)(OH)_3]^0$, $[Fe(III)(H_2O)_2(OH)_4]^-$, $[Fe(III)(OH)_4]^-$. Hill and Schauble (2008) calculated the β-factors of ferric aquo-chloro compounds $[FeIII(H_2O)_6]^{3+}$, $[FeIIICl(H_2O)_5]^{2+}$, $[FeIII(H_2O)_4Cl_2]^+$, $[FeIII(H_2O)_3Cl_3]^0$, $[FeIII(H_2O)_2Cl_3]^0$, $[FeIIICl_4]^-$, $[FeIIICl_5]^{2-}$, $[FeIIICl_6]^{3-}$ to evaluate the influence of the coordination environment of iron. Hill et al. (2009) compared those results with laboratory experiments that they performed. Domagal-Goldman and Kubicki (2008) studied iron equilibrium fractionation factors involving redox changes and organic complexation. They specifically estimated the β-factors of $[FeIII(H_2O)_6]^{3+}$, $[FeII(H_2O)_6]^{2+}$, $[FeIII(Ox)_3]^{3-}$, $[FeII(Ox)_3]^{4-}$, $[FeIII(Cat)_3]^{3-}$, $[FeII(Cat)_3]^{4-}$, where those last 4 molecules refer to iron trisoxalate and triscatecholate. Moynier et al. (2013) also studied the β-factors of iron bound to organic molecules, namely Fe(II)-citrate, Fe(III)-citrate, Fe(II)-nicotianamine, and Fe(III)-phytosiderophore. Fujii et al. (2006) studied the β-factors of $[Fe(III)Cl_4]$- and $[Fe(III)Cl_2(H_2O)_4]^+$. Rustad and Dixon (2009) calculated the β-factors of $Fe(II)_{aq}$, $Fe(IIII)_{aq}$. Fujii et al. (2014) calculated the β-factors of various Fe(II) iron complexes relevant to geochemical and biological systems, namely $Fe(H_2O)_6^{2+}$, $FeCl(H_2O)^{5+}$, $FeCl_2(H_2O)_4$, $FeSO_4(H_2O)_5$, $FeOH(H_2O)_5^+$, $Fe(OH)_2(H_2O)_4$, $Fe_2(OH)_6^{2-}$, $FeHCO_3(H_2O)_4^+$, $FeHCO_3(H_2O)_4$, $FeHS(H_2O)_5^+$, $FeHS(H_2O)_5^+$, $Fe(HS)_2(H_2O)_4$, $Fe_2S_2(H_2O)_4$, $FeH_2PO_4(H_2O)_5^+$, $FeHPO_4(H_2O)_5$, $FeH_4(PO_4)_2(H_2O)_4$, $FeH_3(PO_4)_2(H_2O)_4^-$, $FeH(cit)(H_2O)_3$, $Fe(cit)(H_2O)_3^-$, $FeH(cit)_2^{3-}$, $Fe(cit)_2^{4-}$, and $Fe(cit)_2OH^5$-. They also studied Fe(III) species, namely $Fe(H_2O)_6^{3+}$, $FeCl(H_2O)_5^{2+}$, $FeCl_2(H_2O)_4^+$, $FeSO_4(H_2O)_5^+$, $FeOH(H_2O)_5^{2+}$, $Fe(OH)_2(H_2O)_4^+$, $Fe(OH)_3(H_2O)_3$, $FeHCO_3(H_2O)_4^{2+}$, $FeCO_3(H_2O)_4^+$, $FeH_3PO_4(H_2O)_5^{3+}$, $FeH_2PO_4(H_2O)_5^{2+}$, $FeHPO_4(H_2O)^{5+}$, $FeH_5(PO_4)_2(H_2O)_4^{2+}$, $FeH_4(PO_4)_3(H_2O)_4^+$, $FeH_3(PO_4)_2(H_2O)_4$, $FeH_7(PO_4)_3(H_2O)^{3+}$, $FeH_6(PO_4)_3(H_2O)_3$, $Fe(cit)(H_2O)_3$, $Fe(cit)OH(H_2O)_2^-$, $FeH(cit)_2^{2-}$, $Fe(cit)_2^{3-}$, $Fe(cit)_2OH^{4-}$.

Calculating β-factors of minerals is more involved than for aqueous species, and as a result, the database is much less extensive and the number of independent studies is also much lower. Rustad and Dixon (2009) calculated the β-factors of $Fe(II)_{aq}$, $Fe(III)_{aq}$, and hematite. Blanchard et al. (2009) calculated the β-factors of pyrite, hematite, and siderite. Blanchard et al. (2010) also evaluated the effect of Al_2O_3 substitution in hematite on the β-factor of iron. Blanchard et al. (2015) calculated the β-factor of goethite and compared the predictions with estimates from the NRIXS method. Rustad and Yin (2009) calculated β-factors of ferropericlase and ferroperovskite (bridgmanite) in *P–T* conditions relevant to Earth's lower mantle.

The β-factors can also be measured experimentally by using methods that rely on the fact that iron possesses a Mössbauer isotope. Polyakov and Mineev (2000) used the second order Doppler shift measured in conventional Mössbauer spectroscopy to derive the kinetic energy of the iron atoms, from which they could calculate iron fractionation factors for a variety of minerals based on literature data: aegirine, akakenite, ankerite, bernalite, celadonite, chloritoid, diopside, enstatite, ferrite, ferrochromite, ferrocyanide, goethite, grandidierite, hedenbergite, hematite, ilmenite, lepidocrocite, magnetite, metallic iron, magnesium oxide, nickel sulfide, nitroprusside, olivine, pyrite, and siderite. This study revealed some of the fundamental crystal chemical controls on iron stable isotope variations. Polyakov et al. (2007) subsequently reported β-factors for iron metal, hematite, pyrite, and marcasite. Polyakov and Soultanov (2011) calculated β-factors for mackinawite using conventional Mössbauer data. While sound theoretically, determining the second order Doppler shift is fraught with difficulties and some of the β-factors reported in that publication were later shown to be erroneous when better quality Mössbauer data were acquired

(Polyakov et al. 2007). Another, more robust approach to this problem is to use a synchrotron technique known as Nuclear Resonant Inelastic X-ray Scattering (NRIXS) (Polyakov et al. 2007; Dauphas et al. 2012). The Mössbauer isotope ^{57}Fe has a low lying nuclear excited state that can be reached by X-ray photons of 14.4125 keV, the nominal resonance energy. In NRIXS, the energy of the incoming beam is changed in small steps within an energy range as large as −200 to +200 meV around the nominal resonance energy. The energy resolution of the incoming beam can be reduced to 1.3 meV full width at half maximum, which requires the use of sophisticated X-ray monochromators. At each energy, the scattered X-rays induced by the nuclear transition are analyzed. The prompt X-rays scattered by electrons are discarded by imposing some time discrimination, as electronic scattering is almost instantaneous, while nuclear scattering is delayed due to the finite lifetime (141 ns) of the excited ^{57}Fe nucleus.

When the energy of the incoming X-rays is lower than the nominal resonance energy, some nuclear transitions can still occur because lattice vibrations can fill the gap by providing energy in the form of phonons (the particle-like equivalent of interatomic vibrations). Conversely, when the energy is higher than the nominal resonance energy, some of that extra energy can be absorbed by the solid lattice and the transition can still take place. The first process is known as phonon annihilation while the second process is known as phonon creation. By measuring the flux of the scattered X-rays for various values of the incident X-ray energy, one can thus probe the vibrational properties of the target material, which govern equilibrium fractionation factors (Bigeleisen and Mayer 1947; Urey 1947; Kieffer 1982; Dauphas et al. 2012). Two approaches exist to retrieve β-factors from NRIXS spectra. Polyakov et al. (2007) used the kinetic energy and first order perturbation theory to calculate the β-factor from the PDOS of the iron sublattice $g(E)$. The PDOS is calculated using a Log Fourier transform of the raw signal $S(E)$. Dauphas et al. (2012) used a different approach based on the determination of the force constant of iron bonds and other higher order moments of the raw spectrum $S(E)$. The two approaches are mathematically equivalent (Dauphas et al. 2012). A virtue of the second approach is that the error bars are easy to calculate and one knows how data processing affects the results.

Polyakov et al. (2007) originally used published PDOS (sometimes digitized) to calculate β-factors. However, the β-factor calculation in NRIXS depends on high moments of $S(E)$: the 3rd moment for the force constant and higher order moments for the other coefficients of the polynomial expansion (Dauphas et al. 2012; Hu et al. 2013). Most work done on materials of geological relevance was originally done to determine the Debye velocity, from which compression and shear velocities can be derived (Hu et al. 2003; Sturhahn and Jackson 2007). The Debye velocity is determined by the low energy part of the spectrum, where the signal is high. Not much attention was paid to the high energy part of the spectrum, which influences the β-factor dramatically. Published spectra are often very noisy at high energies and sometimes the measurements are truncated before the signal reaches zero. One should therefore exercise caution when using NRIXS data acquired with other objectives than iron isotope geochemistry. Using previously published data, Polyakov et al. (2007) reported β-factors of magnetite, FeO (wüstite), troilite, and Fe_3S. Polyakov (2009) calculated the β-factors at high pressure-temperature for metallic iron, ferropericlase, perovskite and post-perovskite compositions. Those data were acquired in diamond anvil cells and are quite uncertain, with NRIXS spectra that are sometimes truncated. Polyakov and Soultanov (2011), calculated the β-factors of chalcopyrite, troilite, and Fe_3S. Dauphas et al. (2012), also using previously published data calculated the β-factors of myoglobin, cytochrome f, orthoenstatite, hematite, magnetite, troilite, FeS (MbP-type), FeS (monoclinic), chalcopyrite, Fe_3S, $(Mg_{0.75}Fe_{0.25})O$, α-Fe, γ-Fe, ε-Fe, and σ-Fe.

A difficulty with NRIXS data that was not fully appreciated until 2014 is that the signal does not seem to always reach a background value (Dauphas et al. 2014). Sometimes, the low or high energy ends are above background and are different from each other. This has led to the erroneous determination of the β-factors of goethite and jarosite (Dauphas et al. 2012), that

were later corrected based on a new data reduction procedure that yielded more reproducible results from session to session (Blanchard et al. 2015). The new data reduction uses a new software, SciPhon, which has a routine to adequately subtract a non-constant baseline. The database of high quality NRIXS data is rapidly expanding and there are now good estimates of iron β-factors for goethite and jarosite (Blanchard et al. 2015), olivine, Fe^{2+} and Fe^{3+} in glasses of basaltic, andesitic, dacitic, and rhyolitic compositions (Dauphas et al. 2014), and spinels (Roskosz et al. 2015). Krawczynski et al. (2014a) reported force constant measurements for troilite and fcc Fe–Ni metal alloy. Williams et al. (2016) measured the force constant of iron in ilmenite and glasses with compositions relevant to lunar petrology.

Shahar et al. (2016) recently reported NRIXS measurements of high-pressure alloys FeO, FeH_x, and Fe_3C. Liu et al. (2016) also measured the mean force constants of basaltic glass, metallic iron, and iron-rich alloys of Fe–Ni–Si, Fe–Si, and Fe–S up to 206 GPa. Those studies were done specifically for the purpose of deriving β-factors and used extended energy ranges and the SciPhon software to do the data reduction. They thus do not suffer from some of the shortcomings of early NRIXS studies whose aims were to derive seismic velocities.

Comparisons of ab initio, NRIXS, and experimental studies. To compare the different methods, in particular to compare α-values determined experimentally with absolute β-factors determined by ab initio calculations or NRIXS, the easiest method is probably to convert all α-values to β-factors (Eqns. 15, 16) using a mineral that has been extensively studied. Polyakov et al. (2007) proposed to use hematite as there is reasonably good agreement between the β-factors estimated by conventional Mössbauer (Polyakov et al. 2007), NRIXS (Polyakov et al. 2007; Dauphas et al. 2012), and ab initio calculations (Blanchard et al. 2009). We concur with this assessment.

In Figure 6, we compare the experimentally determined fractionation factors between $Fe(III)_{aq}$–$Fe(II)_{aq}$ (Welch et al. 2003) and $Fe(III)_{aq}$–hematite (Skulan et al. 2002) with the predictions from ab initio and NRIXS studies (Table 1). The ab initio studies (Anbar et al. 2005; Domagal-Goldman and Kubicki 2008; Hill and Schauble 2008; Ottonello and Zuccolini 2009; Rustad and Dixon 2009; Fujii et al. 2014) can reproduce the equilibrium fractionation factor for $Fe(III)_{aq}$-$Fe(II)_{aq}$ (Welch et al. 2003). However, ab initio (Anbar et al. 2005; Domagal-Goldman and Kubicki 2008; Hill and Schauble 2008; Ottonello and Zuccolini 2009b; Rustad and Dixon 2009b; Fujii et al. 2014; Blanchard et al. 2009) and NRIXS studies (Dauphas et al. 2012) fail to reproduce the measured fractionation between $Fe(III)_{aq}$–hematite (Skulan et al. 2002). The β-factor of hematite agrees well between different techniques (Polyakov et al. 2007; Rustad and Dixon 2009; Blanchard et al. 2009; Dauphas et al. 2012) while the β-factors of $Fe(III)_{aq}$ can be quite variable from study to study, giving values at 22 °C of +8.4‰ (Rustad and Dixon 2009), +11.8‰ (Schauble et al. 2001), +9.6‰ (Anbar et al. 2005), +8.9‰ (Ottonello and Zuccolini 2009), +9.4‰, +10.1‰ (Hill and Schauble 2008), and +8.3‰ (Fujii et al. 2014). Regardless of this complication, all calculations predict a $Fe(III)_{aq}$-hematite isotopic fractionation that is larger than what is measured. This problem was recognized by Rustad and Dixon (2009) and more recent estimates have not solved the discrepancy. It is currently unknown whether the issue is with the calculation or if kinetic effects were present in the experiments.

To try to go around the issue that comparing β-factors for aqueous species and minerals may introduce biases, we have used the fluid–mineral equilibration experiments to recalculate equilibrium fractionation factors between mineral pairs at low temperature. For the reasons outlined above, we use hematite as the reference mineral against which other minerals are compared. The results of NRIXS/ab initio studies and experimentally determined mineral-mineral fractionation factors at 22 °C are compared in Figure 7. The measured ferrihydrite–hematite (Skulan et al. 2002; Welch et al. 2003; Wu et al. 2011) and

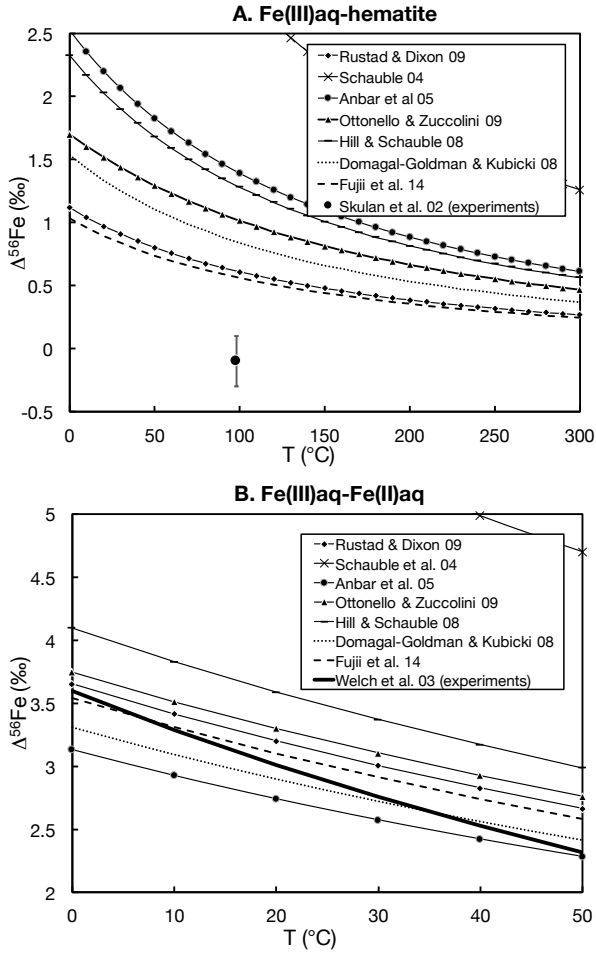

Figure 6. Comparison between experimentally measured and predicted (based on NRIXS data and/or ab initio calculations) equilibrium fractionation factors between $Fe(III)_{aq}$–hematite (A) and $Fe(III)_{aq}$–$Fe(II)_{aq}$ (B). The most recent ab initio calculations can reproduce well the equilibrium fractionation factor between $Fe(III)_{aq}$ and $Fe(II)_{aq}$. However, the calculations predict a larger $Fe(III)_{aq}$–hematite fractionation than is measured. The data sources are indicated on the figure and the β-factors used for the calculation are compiled in Table 1. For hematite in the top panel, the average value of several NRIXS and ab initio studies was used (Rustad and Dixon 2009; Blanchard et al. 2009; Dauphas et al. 2012).

siderite–hematite (Skulan et al. 2002; Welch et al. 2003; Wiesli et al. 2004) fractionation factors agree well with the predictions for goethite–hematite and siderite–hematite (Blanchard et al. 2009, 2014; Rustad and Dixon 2009; Dauphas et al. 2012). Figure 7 also shows a comparison between measured mackinawite–$Fe(II)_{aq}$ fractionation (Guilbaud et al. 2011; Wu et al. 2012b) converted to mackinawite–hematite using the relevant fractionation factors and predicted troilite–hematite fractionation (Polyakov et al. 2007; Rustad and Dixon 2009; Dauphas et al. 2012; Blanchard et al. 2015). There is a ~1‰ disagreement at 22 °C but it is unsure to what extent troilite can be taken as a proxy for mackinawite. For

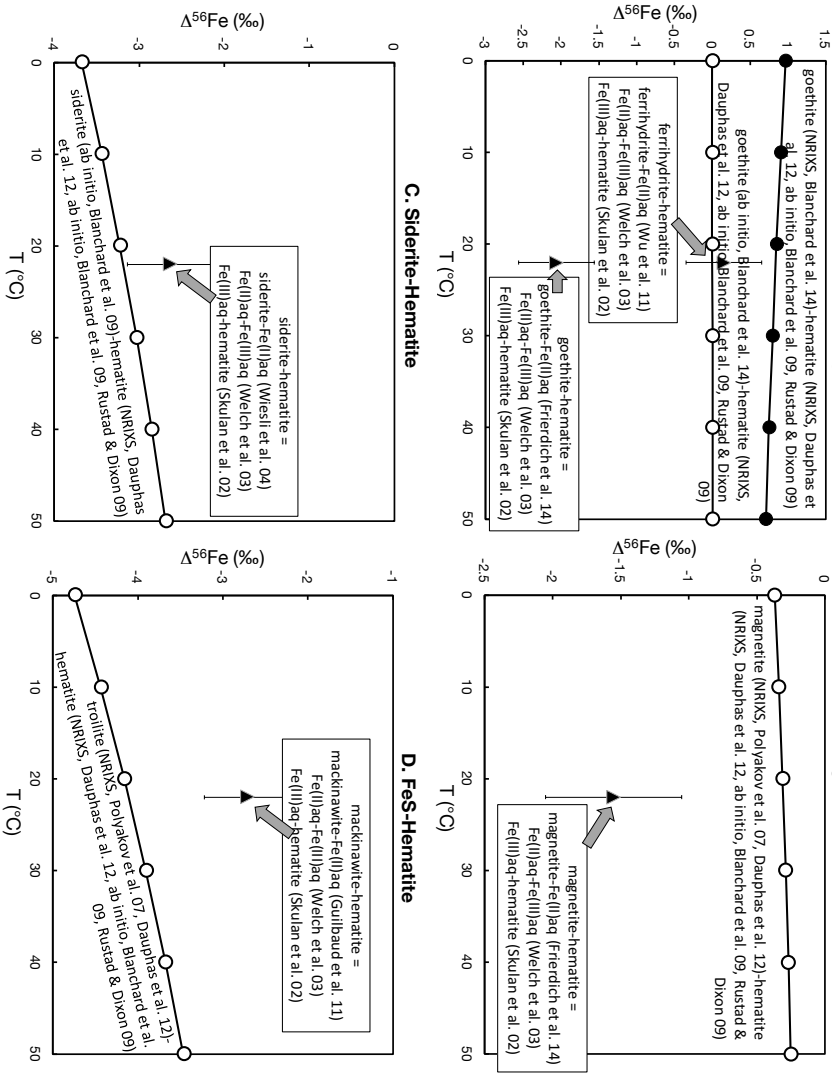

Figure 7. Equilibrium fractionation between mineral pairs based on fluid–mineral equilibration experiments (recalculated to a common temperature of 22 °C) and comparison with predictions from NRIXS and ab initio studies. Hematite was taken as a reference because the equilibrium fractionation factor between $Fe(III)_{aq}$ and hematite was measured experimentally (Skulan et al. 2002) and the β-factor of hematite estimated by NRIXS (Dauphas et al. 2012) and ab initio calculations (Blanchard et al. 2009a; Rustad and Dixon 2009) agree well. As an example of how the mineral–mineral fractionation factors were calculated, goethite–hematite fractionation was calculated as follows: The experimentally determined fractionation for $Fe(III)_{aq}$–hematite at 98 °C is –0.1 ± 0.2‰ (Skulan et al. 2002). At 22 °C, this corresponds to a fractionation of $-0.1\times(273+98)^2/(273+22)^2=-0.16\pm0.32$‰. At 22 °C, laboratory experiments give a $Fe(III)_{aq}$–$Fe(II)_{aq}$ equilibrium fractionation of +2.95 ± 0.38‰ (Welch et al. 2003). Experiments also give a goethite–$Fe(II)_{aq}$ fractionation of +1.05 ± 0.08‰ (Frierdich et al. 2014a). The net goethite–hematite fractionation is thus 1.05 – 2.95 – 0.15 = –2.05 ± 0.50‰. Note that the FeS–hematite panel compares the measured fractionation between mackinawite and hematite against predictions for troilite and hematite. The data sources are indicated on the figure and the β-factors used for the calculation are compiled in Table 1.

the pair magnetite–hematite, the experimentally determined (Skulan et al. 2002; Welch et al. 2003; Frierdich et al. 2014b) and NRIXS predicted (Polyakov et al. 2007; Dauphas et al. 2012) fractionation factors are also off by ~1‰. The β-factor of magnetite by NRIXS is uncertain and Roskosz et al. (2015) suggested that it may need to be revised upwards, which would exacerbate the discrepancy. The most striking discrepancy is for the pair goethite-hematite, where experiments (Skulan et al. 2002; Welch et al. 2003; Beard et al. 2010; Frierdich et al. 2014a) are off from NRIXS and ab initio predictions (Blanchard et al. 2009, 2015; Rustad and Dixon 2009; Dauphas et al. 2012) by ~2‰. Experiments also indicate that there would be a 2‰ equilibrium fractionation between ferrihydrite and goethite (Beard et al. 2010; Wu et al. 2011; Frierdich et al. 2014a), which is difficult to explain from a crystal chemical point of view.

In Fig. 8, we compare measured high-temperature equilibrium fractionation factors with predictions from NRIXS measurements for 3 systems. The fractionation measured by Schuessler et al. (2007) for the system FeS–rhyolitic melt is relatively well reproduced by NRIXS predictions (Polyakov et al. 2007; Dauphas et al. 2012, 2014) (Fig. 8a). The fractionations measured by Hin et al. (2012) and Poitrasson et al. (2009) for silicate–metal are marginally consistent with the fractionation predicted by NRIXS for basaltic glass–bcc iron (Dauphas et al. 2012, 2014) but are lower than the predicted fractionation for basaltic glass–fcc iron (Dauphas et al. 2012, 2014; Krawczynski et al. 2014a) (Fig. 8b). The results of Shahar et al. (2015) are, however, much lower than the NRIXS predictions for both basaltic glass–bcc and basaltic glass–fcc iron (Fig. 8b). The experiments were done on molten systems, and it is unknown to what extent some of these discrepancies are due to the fact that the solid (glass or crystal) systems measured by NRIXS are imperfect proxies for melt β-factors. The measured fractionation between magnetite and olivine (Shahar et al. 2008; Sossi and O'Neill 2016) is significantly higher than the prediction from NRIXS measurements for magnetite-olivine (Polyakov et al. 2007; Dauphas et al. 2012, 2014) (Fig. 8c). This could be due to the fact that the β-factor of magnetite as measured by NRIXS is not accurate (it was not measured for the purpose of estimating β-factors), as a more recent study of the spinel solid solution predicted an equilibrium fractionation factor at a Fe^{3+}/Fe_{tot} relevant to magnetite more in line with what is measured (Roskosz et al. 2015).

IRON ISOTOPES IN COSMOCHEMISTRY

Nucleosynthetic anomalies and iron-60

Chondrites are undifferentiated meteorites whose compositions are thought to represent the composition of the solar system at one point in time and space. During their formation, they incorporated dust formed in the outflows of stars that lived and died before the solar system was formed. The composition of those presolar grains is representative of the star from which they formed. They are thus invaluable tools to study stellar nucleosynthesis and the chemical evolution of the Galaxy. Mahras et al. (2008) measured the Fe isotopic compositions of presolar silicon carbide (SiC) grains of mostly AGB-star (Asymptotic Giant Branch) and type II supernova origins (those origins are ascribed on the basis of isotopic analyses of C, N and Si). Most supernova grains show large excesses in ^{57}Fe while AGB grains have more subdued anomalies. The measurements were done with a NanoSIMS, which does not allow one to resolve the peaks of the low abundance isotope ^{58}Fe and the high abundance ^{58}Ni, so ^{58}Fe was not reported. The compositions of the supernova grains could be reproduced by arbitrarily mixing material from the He/N and He/C zones of supernova simulations. Outstanding questions at the present time are: how was such fine-scale mixing achieved and why did SiC grains preferentially sample those regions? Progress may be achieved by measuring the Fe and Ni isotopic compositions

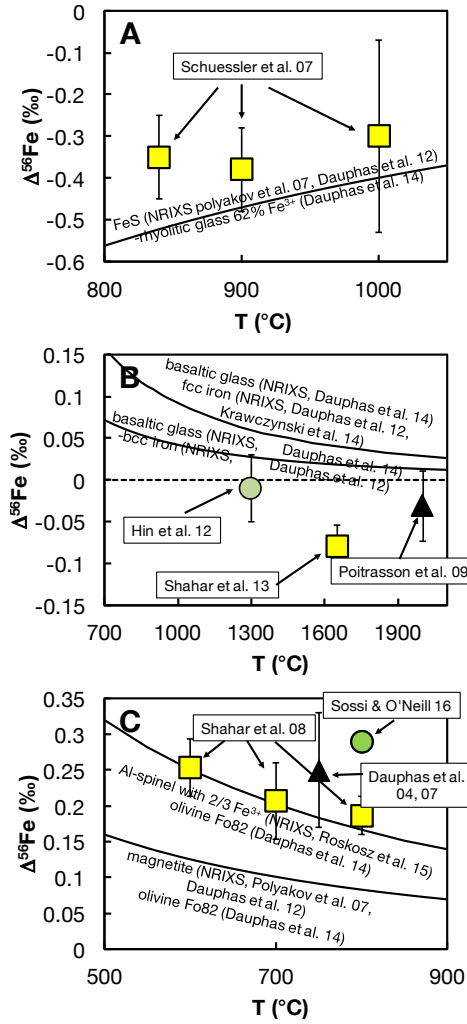

Figure 8. Comparisons between experimentally determined and calculated (from NRIXS measurements) equilibrium fractionation factors between high temperature phases (pyrrhotite–peralkaline rhyolitic melt with 2/3 Fe^{3+} in panel A; silicate–metal in panel B; magnetite–olivine in panel C). The data sources are indicated on the figure and the β-factors used for the calculation are compiled in Table 1.

of X-grains (SiC presolar grains that are thought to come from supernovae) using resonant ionization mass spectrometry, which allows one to measure the isotopic composition of iron, including ^{58}Fe, even in the presence of large quantities of Ni (Trappitsch et al. 2016).

FUN (fractionated and unknown nuclear effects) refractory inclusions are other significant carriers of nucleosynthetic anomalies in meteorites (Dauphas and Schauble 2016, and references therein). Völkening and Papanastassiou (1989) discovered large excesses in the neutron-rich isotope of iron (^{58}Fe) in a FUN inclusion named EK-1-4-1 from the Allende CV chondrite. This nucleosynthetic excess in ^{58}Fe of ~+30‰ is consistent with enrichments in other neutron-rich isotopes such as ^{48}Ca and ^{50}Ti found in the same

refractory inclusion. For some elements like Ti, isotopic anomalies are pervasive in all kinds of refractory inclusions, while only one such inclusion has revealed such a large ^{58}Fe excess. One reason for that may be that iron is a relatively volatile element that is not expected to have condensed quantitatively, so most iron found in refractory inclusions is probably of secondary origin, having been introduced by aqueous alteration

The abundance of the short-lived radionuclide ^{60}Fe ($t_{1/2}$=2.62 Myr) has been the subject of much discussion over the past couple of years. Measurements of ^{60}Ni, the decay product of ^{60}Fe, in bulk meteorites and mineral separates by MC-ICPMS gives a ^{60}Fe/^{56}Fe ratio of ~1×10^{-8} (Tang and Dauphas 2012, 2014, 2015) (Fig. 9). In situ measurements by SIMS give a much higher initial ^{60}Fe/^{56}Fe ratio of ~7×10^{-7} (Mishra and Goswami 2014; Mishra and Chaussidon 2014; Mishra and Marhas 2016). It was argued that this discrepancy could be due to heterogeneous distribution of ^{60}Fe in solar system materials (Quitté et al. 2010). One way to test that idea is to measure the ^{58}Fe isotopic composition, because ^{58}Fe and ^{60}Fe are produced in the same stellar environments by the same neutron-capture reactions, so those two nuclides should be very well coupled. Therefore, if ^{60}Fe was heterogeneously distributed in meteorites, one would expect to detect collateral isotope effects on ^{58}Fe (Dauphas et al. 2008). Such collateral effects were not detected, which led Tang and Dauphas (2012, 2015) to conclude that the initial abundance of ^{60}Fe was low and uniform (^{60}Fe/^{56}Fe ~1×10^{-8}). This ratio is low compared to the prediction for supernova injection if the short-lived radionuclide ^{26}Al ($t_{1/2}$=0.7 Myr) shared such a supernova origin. The reason for this low abundance is debated but one possibility is that ^{26}Al was ejected in the interstellar medium in the form of stellar winds, which contained little ^{60}Fe as this nuclide

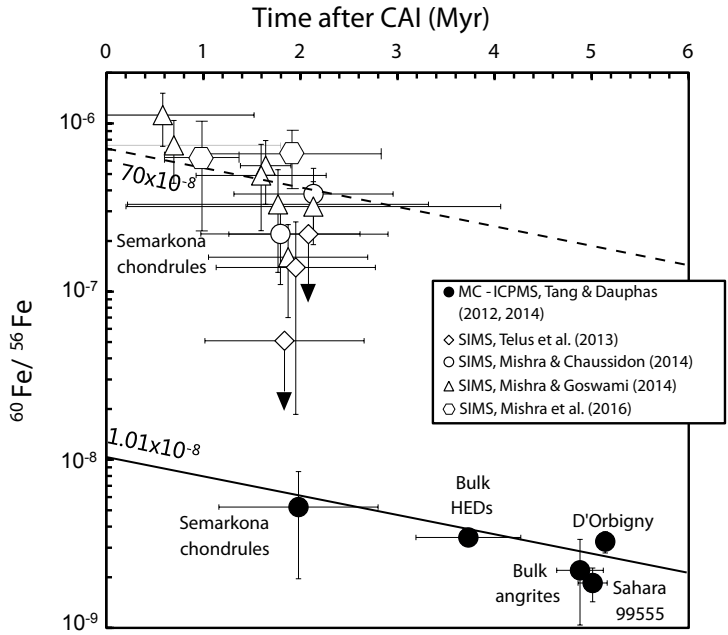

Figure 9. Inferred initial ^{60}Fe/^{56}Fe ratio (^{60}Fe decays into ^{60}Ni with a half-life of 2.6 Myr) of various meteoritic materials (from Tang and Dauphas 2015; updated with the data of Mishra and Marhas 2016). MC-ICPMS measurements detected ^{60}Fe in various materials (Semarkona chondrules, bulk HED meteorites, bulk angrites, mineral separates in D'Orbigny and Sahara 99555 angrites) corresponding to an intial ^{60}Fe/^{56}Fe ratio of ~10^{-8} (Tang and Dauphas 2012a, 2015). In situ measurements by SIMS gave variable initial ^{60}Fe/^{56}Fe ratios that reach 10^{-6} (Mishra and Goswami 2014; Mishra and Chaussidon 2014; Mishra and Marhas 2016). Downward pointing vertical arrows correspond to upper-limits. The weight of evidence supports a low ^{60}Fe/^{56}Fe ratio at solar system formation (see text for details).

was produced in more internal regions of the star. Iron–60 was ejected in the interstellar medium at a later time by the supernova explosion that ended the life of the massive star (Tang and Dauphas 2012). Further work will be needed to assess the likelihood of this scenario.

Overview of iron isotopic compositions in extraterrestrial material

Chondrites and their components. A characteristic feature of most chondrites is the presence of chondrules, which are quenched beads of silicate whose origin is still very much debated. During the heat event that melted the chondrules (shockwaves, planetary collisions, and lightning have been proposed), some of the iron, which is relatively volatile, could have volatilized. An important question in this respect is whether iron-poor type I chondrules could have formed from iron-rich type II chondrule material by iron evaporation. Alexander and Wang (2001) measured the Fe isotopic compositions of chondrules from Chainpur, a LL3.4 chondrite (the 3.4 grading means that the meteorite was not much heated and the Fe isotopic signature was not disturbed by parent-body metamorphism). They found no detectable variations in the isotopic composition of iron with a precision of ~2‰ (the measurements were acquired by ion probe). Mullane et al. (2005), Needham et al. (2009), and Hezel et al. (2010) also measured the Fe isotopic compositions of chondrules from various meteorite groups (CV, H, L, and LL) by MC-ICPMS. The precision of those measurements was significantly better than SIMS and isotopic variations were resolved but the variations were limited. The δ^{56}Fe values of most chondrules fall within ±0.2‰ of the bulk chondrite composition and the average chondrule δ^{56}Fe value is indistinguishable from the bulk chondrite value. If significant Fe was evaporated under vacuum conditions, then large Fe isotopic fractionation would be expected (Wang et al. 1994; Dauphas et al. 2004a). The lack of detectable Fe isotopic fractionation can be explained if iron was not lost by evaporation, or significant iron vapor pressure built up around the chondrules, which suppressed the kinetic fractionation (as P/P_{sat} approaches 1, the system approaches equilibrium between gas and condensed phase; Eqn. 12). Evaporation in a closed system is supported by the fact that highly volatile potassium shows little isotopic fractionation in chondrules (Alexander et al. 2000; Alexander and Grossman 2005). It is also supported by the fact that another volatile element, sodium, is present in the cores of zoned olivines, meaning that even at the highest temperatures reached during chondrule heating, significant Na was still present in molten chondrules, which is only explainable if the chondrule density was sufficiently high for vapor to build up and partially suppress evaporation (Alexander et al. 2008).

The Urey–Craig diagram (Urey and Craig 1953) groups chondrites according to their total iron content and the fraction of iron as metal vs. silicate or sulfide. Despite these variations in the Fe/Si ratio and redox state of iron, chondrites have very constant Fe isotopic compositions, at least given present analytical precision (Fig. 10). Craddock and Dauphas (2011a) measured the Fe isotopic compositions of 10 carbonaceous chondrites, 15 ordinary chondrites, and 16 enstatite chondrites. Except for Kelly (a LL4) and high metamorphic grade EL6 chondrites, all samples have the same Fe isotopic composition, defining an average δ^{56}Fe value of -0.005 ± 0.006‰. This composition is indistinguishable from that of the reference material IRMM–014/524a (δ^{56}Fe = 0 by definition). This is purely coincidental but is another argument for the general adoption of this reference material as standard in iron isotope geochemistry, as it is representative of an important geochemical reservoir (the chondritic composition).

Mars, Vesta, and the Angrite parent-body. SNC (Shergottite-Nakhlite-Chassignite) and HED (Howardite, Eucrite, Diogenite) achondrite meteorites have Fe isotopic compositions that are almost indistinguishable from the chondritic composition (Poitrasson et al. 2004; Weyer et al. 2005; Anand et al. 2006; Schoenberg and von Blanckenburg 2006; Wang et al. 2012; Sossi et al. 2016) (Fig. 11). SNC and HED meteorites are magmatic rocks that, as several lines of evidence indicate, come from Mars and Vesta, respectively. Among HEDs, there seems to be some isotopic variations, in particular with Stannern group eucrites that are enriched in

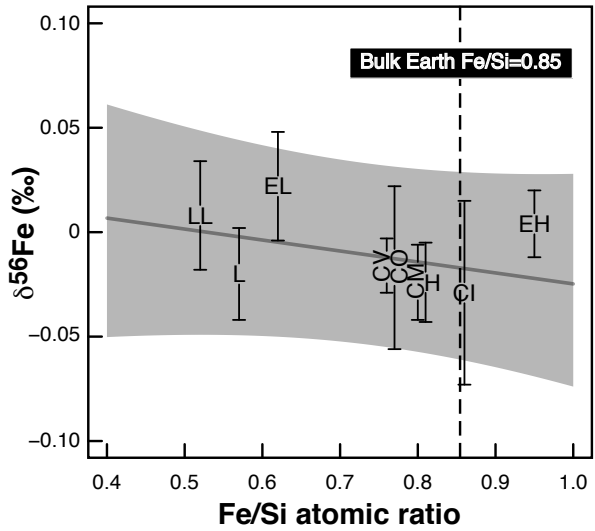

Figure 10. Iron isotopic compositions of chondrite groups as a function of Fe/Si ratios (Dauphas et al. 2009b). Even if chondrites have variable iron contents (Fe/Si ratios) and redox states, the δ^{56}Fe values are relatively constant. The grey band is the 95% confidence for the regression.

heavy Fe isotopes by ~+0.03‰ in δ^{56}Fe (Wang et al. 2012). Stannern eucrites are enriched in incompatible elements relative to main group eucrites, which was explained by smaller degree of partial melting or, more likely, by assimilation of differentiated crustal material (Barrat et al. 2007). The enrichment in the heavy isotopes of iron can be understood in the context of the crust assimilation model if the bulk of Vesta crust has heavy Fe isotopic composition or if assimilation took place in a non-modal manner, so that isotopically heavy minerals such as ilmenite were preferentially incorporated in the parental magma to Stannern group eucrites.

Martian samples also have on average chondritic Fe isotopic composition with a hint for heavier Fe isotopic compositions in Nakhlites but the total range in δ^{56}Fe values is small with most samples within −0.03 and +0.03‰ (Poitrasson et al. 2004b; Weyer et al. 2005a; Anand et al. 2006; Wang et al. 2012). The slightly heavy Fe isotopic composition of nakhlites and evolved shergottites can be explained by magmatic differentiation (Sossi et al. 2016).

Angrites, which are a group of basaltic meteorites that come from a body that was relatively oxidized (~IW+1), have heavy δ^{56}Fe values similar to terrestrial basalts, i.e., δ^{56}Fe values of ~+0.1‰ (Wang et al. 2012) (Fig. 11). On Earth, it was suggested that the presence of Fe^{3+} in significant quantities could affect the Fe isotopic composition of igneous rocks. While angrites are more oxidized than other achondrites, they are significantly more reduced than terrestrial basalts (~IW+1 vs. ~IW+2.5) and Fe^{3+} is not expected to directly influence the Fe isotopic composition of the angrite parent body. Impact volatilization (Poitrasson et al. 2004; Wang et al. 2012) is also unlikely because for bodies of the size of the angrite parent-body, the energy available from collisional accretion is thought to be small compared to the latent heat of vaporization (Dauphas et al. 2015). It is presently unknown why angrites have heavy Fe isotopic composition, one possibility being that this is a feature inherited from nebular processes, as was suggested for Si (Dauphas et al. 2015). Overall, studies of achondrites show that magmatic processes such as magmatic differentiation and assimilation on planetary bodies can fractionate iron isotopes. Nevertheless, those fractionations are subtle and the mantles of Mars and Vesta have Fe isotopic compositions that are indistinguishable from chondrites to very high precision (Fig. 11).

Barrat et al. (2015) analyzed the Fe isotopic compositions of 30 samples from the Ureilite Parent Body (UPB) including 29 unbrecciated ureilites and one ureilitic trachyandesite (ALM-A). Ureilites are ultramafic achondrites, which are thought to be mantle restites formed after extraction of magmas and S-rich metallic melts. The δ^{56}Fe of the whole rocks fall within a restricted range, from +0.01 to +0.11‰, with an average of +0.056 ± 0.008‰, which is significantly higher than that of chondrites. This difference has been ascribed to the segregation of S-rich metallic melts at low degrees of melting at a temperature close to the Fe–FeS eutectic. These results point to an efficient segregation of S-rich metallic melts during the differentiation of small terrestrial bodies (Barrat et al. 2015).

The Moon. Lunar soils show variations in the isotopic composition of iron that correlate with the maturity of the soils, a measure of the exposure of the soil to space weathering (Wiesli et al. 2003). Those variations are thought to be due to the presence of nanophase Fe metal in the most mature soils. Nanophase Fe metal is produced by vapor deposition by micrometeorite impacts and solar-wind sputtering. Thus, to discuss the Fe isotopic composition of the Moon or other airless bodies, one should stay clear of soils.

Of all the lithologies present at the surface of the Moon, the ones that provide the most insights into the composition of the Moon are mare basalts that fill the maria. These formed relatively late (radiometric dating gives ages of ~3 to 4 Ga) and are thought to sample a deep-seated source in the lunar mantle (150–600 km; Lee et al. 2009). A difficulty with estimating the composition of the Moon is that the lack of plate tectonics like on Earth has allowed the survival of significant heterogeneities in the lunar mantle, presumably inherited from lunar magma ocean differentiation. High- and low-Ti mare basalts have distinct Fe isotopic compositions, with the δ^{56}Fe of high-Ti basalts averaging +0.191 ± 0.020‰ compared to +0.073 ± 0.018‰ for low-Ti basalts (Wiesli et al. 2003; Poitrasson et al. 2004; Weyer et al. 2005; Liu et al. 2010) (Fig. 11). A difference between low- and high-Ti basalts was also found for the isotopic compositions of O (Liu et al. 2010) and Mg (Sedaghatpour et al. 2013). For Fe, this contrast is unlikely to reflect shallow magma differentiation processes and reflects instead differences in the source region composition or the mode of melting (Liu et al. 2010). The δ^{26}Mg and δ^{56}Fe values of lunar samples are negatively correlated; the low-Ti basalts have δ^{26}Mg indistinguishable from the terrestrial composition of −0.25 ± 0.10‰ whereas high-Ti basalts have more negative δ^{26}Mg values averaging −0.49 ± 0.14‰ (Sedaghatpour et al. 2013). Low-Ti basalt have δ^{49}Ti isotopic composition similar to terrestrial basalts while high-Ti basalts have slightly elevated δ^{49}Ti values, athough this is at the limit of detection (Millet et al. 2016). Magnesium, iron, and titanium isotopes thus suggest that low-Ti mare basalts are more representative of the bulk silicate Moon. At the present time, the Fe isotopic composition of the bulk Moon is very uncertain but its best estimate is close to the average Fe isotopic composition of low-Ti mare basalts; δ^{56}Fe ≈ +0.084‰ (Liu et al. 2010; Fig. 11)

HIGH-TEMPERATURE GEOCHEMISTRY

Low temperature aqueous processes can impart large iron isotopic fractionation. Because equilibrium fractionation factors decrease as $\sim 1/T^2$ (with T in K), it was initially thought that all igneous rocks should have identical Fe isotopic composition, providing a useful baseline to reference iron isotope variations documented in sediments (Beard and Johnson 1999). At 1200 °C the equilibrium fractionation factor is expected to decrease by a factor $(1473/293)^2 = 25$ compared to that at 20 °C, meaning that variations at the few tenths of permil at most are expected at high temperature in natural systems (at least when equilibrium processes are involved). Once analytical capabilities reached sufficient precision, iron isotope variations in mineral separates and bulk igneous rocks were readily detected (Zhu et al. 2002;

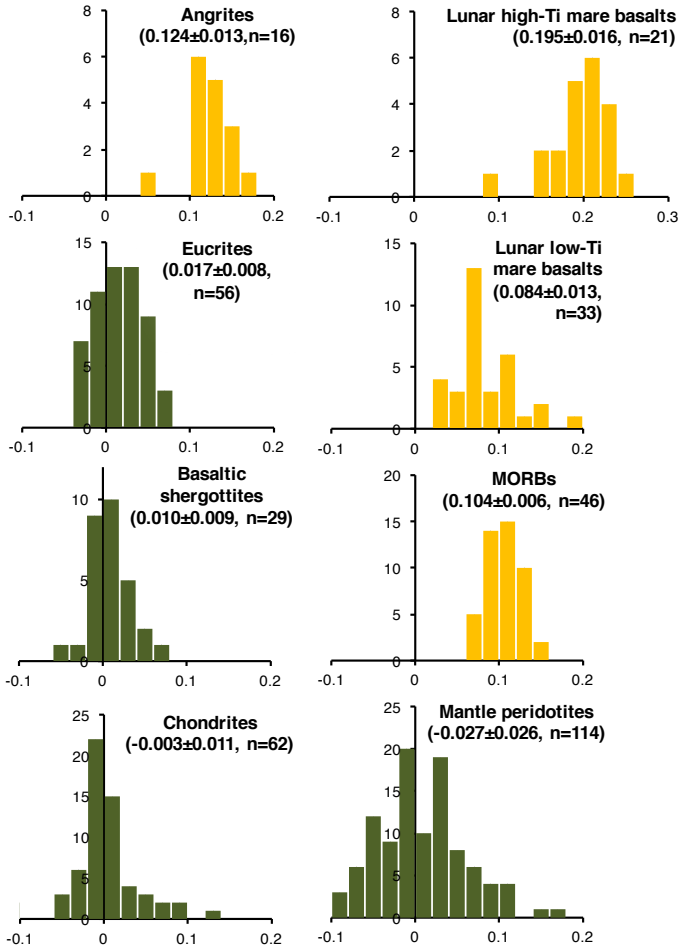

Figure 11. Histograms of δ^{56}Fe values in planetary reservoirs (compilation from the authors; see text for details and references). Eucrites, SNCs (martian meteorites) and mantle peridotites have near chondritic Fe isotopic compositions. MORBs, lunar basalts, and angrites have heavy δ^{56}Fe values relative to chondrites and mantle peridotites. The origins of those enrichments are not well understood. The mean, 95% confidence interval of the mean, and number of samples analyzed are given in parenthesis.

Beard and Johnson 2004b; Poitrasson et al. 2004; Williams et al. 2004a,b; Poitrasson and Freydier 2005; Weyer et al. 2005; Schoenberg and von Blanckenburg 2006; Teng et al. 2011). This is now a very active field of research in iron isotope geochemistry.

Iron isotope variations in mafic and ultramafic terrestrial rocks and the composition of the silicate Earth

Several sample types can be used to estimate the Fe isotopic composition of Earth's mantle. The first samples that were used for that purpose were basalts (Beard and Johnson 1999). One good reason to use those is that they sample large volumes of the Earth. Taking ocean ridges as an example, the yearly production of lavas is ~21 km^3 (Crisp 1984). Given that they form by ~10% partial melting, this means that globally and every year, 210 km^3 of Earth's mantle is sampled by MORBs. Actually, much of the early measurements were done on igneous rocks from oceanic island and continental settings, the reason being that geostandards are readily

available for these settings (e.g., BHVO basalt from Hawaii, BCR flood basalt from Columbia river). On the basis of these measurements, it was concluded that the silicate Earth had heavy Fe isotopic composition relative to chondrites (Poitrasson et al. 2004). Teng et al. (2013) subsequently published an extensive survey of the Fe isotopic composition of mid-ocean ridge basalts and showed that MORBs have constant δ^{56}Fe values (MSWD~1) (Fig. 11). It is thus tempting to conclude that the silicate Earth as a whole is isotopically fractionated relative to chondrites. However, Fe^{2+} has an effective partition coefficient of ~1 during partial melting (the FeO concentrations in MORBs and fertile peridotites are similar at ~8 wt%), meaning that when a mantle reservoir melts by 10% partial melting, 90% of iron is left behind in the mantle. While it is true that equilibrium fractionation decreases rapidly with increasing temperature, the fact that 90% of iron is left behind in the mantle provides considerable leverage to fractionate the isotopic composition of iron in the melt.

The samples that should provide the best estimate of the Fe isotopic composition of Earth's mantle are mantle peridotites that directly sample the shallowest portion of Earth's mantle (Fig. 11). Several peridotite types have been studied, including xenoliths from arcs, continental settings, ultramafic massifs, and abyssal peridotites. Zhu et al. (2002), Beard and Johnson (2004b), and Williams et al. (2004, 2005) were among the first to measure significant differences in δ^{56}Fe values between coexisting mantle minerals. Inter-mineral fractionations in peridotites do not vary systematically with the inferred closure temperatures, indicating that they are in disequilibrium, consistent with alteration by metasomatism (Beard and Johnson 2004b; Zhao et al. 2010; Roskosz et al. 2015). Williams et al. (2004, 2005) studied both bulk rocks and mineral separates of samples from the sub-continental margin mantle lithosphere, the sub-continental mantle lithosphere, and the sub-arc mantle. They found large iron isotopic variations, with high fO_2 sub-arc samples carrying lower δ^{56}Fe values than other peridotites. Spinels also show a strong correlation between the recorded oxygen fugacity and Fe isotopic composition. Quantitative modeling of those results is difficult but the pattern of isotopic variations in those rocks is qualitatively consistent with melt depletion under oxidizing conditions in arc samples. In an effort to better understand what controls Fe isotopic variations in mantle rocks and assess the composition of the silicate Earth, Weyer et al. (2005) and Weyer and Ionov (2007) studied mantle peridotites from diverse tectonic settings. Weyer and Ionov (2007) found that most of those samples defined a trend between δ^{56}Fe and Mg/(Mg+Fe), an indicator of melt extraction, such that the samples that have experienced the most extensive melt extraction were isotopically the lightest. The authors could explain the trend that they measured by a fractionation between melt and residue of +0.1 to +0.3‰. Extrapolating the iron isotopic data to a fertile mantle Mg# of 0.894 yielded a fertile mantle value of δ^{56}Fe of +0.02±0.03‰. They also identified several metasomatic trends in metasomatized peridotites that shifted δ^{56}Fe values towards heavy or extremely light values. The heavy Fe isotopic signatures in the metasomatized peridotites can be explained by the fact that the metasomatizing melt had heavy isotopic composition inherited from partial melting and silicate melt–solid interactions. The very low δ^{56}Fe values may reflect kinetic isotope fractionation during diffusion of Fe (the light isotopes tend to diffuse faster; Richter et al. 2009a). Schoenberg and von Blanckenburg (2006), Huang et al. (2011), Zhao et al. (2010, 2012), and Poitrasson et al. (2013) also measured the Fe isotopic compositions of mantle xenoliths and found that on average, those samples have an Fe isotopic composition indistinguishable from chondrites but display significant variations, presumably associated with melt extraction and metasomatic processes. All studies of mantle peridotites have found δ^{56}Fe values that were on average lower than the mean MORB δ^{56}Fe value of ~+0.1‰, suggesting that the Earth may be chondritic. Poitrasson et al. (2013) argued, however, that lithospheric mantle xenoliths are not representative of the Fe isotopic composition of the asthenosphere because they have been affected by complex melt extraction–metasomatic events, so that the silicate Earth may have a δ^{56}Fe value of +0.1‰, as is measured in MORBs.

Volumetrically, MORBs are the most important magmas at the surface of the Earth and they constitute much of Earth's oceanic crust (Crisp 1984). To directly address the question of whether iron isotopes can be fractionated during partial melting, Craddock et al. (2013) measured the Fe isotopic compositions of abyssal peridotites, which represent the mantle residues left behind from MORB generation. The difficulty with these samples is that ultramafic rocks in contact with seawater are extensively serpentinized and weathered. The MgO/SiO_2 ratio is a good proxy for the extent of marine weathering as Mg is more easily mobilized than Si during this process (Snow and Dick 1995). Craddock et al. (2013) found that abyssal peridotites have on average the same Fe isotopic composition as chondrites. The most weathered samples showed more scatter than the least weathered but focusing on the least weathered samples, Craddock et al. (2013) obtained an average δ^{56}Fe value of $+0.010 \pm 0.007$‰. For 10% partial melting, the Fe isotopic composition is not shifted much but accounting for this effect, Craddock et al. (2013) estimated the composition of the mantle source of MORBs to be $+0.025 \pm 0.025$‰. For comparison, MORBs have an average δ^{56}Fe value of $+0.105 \pm 0.006$‰. These results therefore suggest that partial melting can fractionate iron isotopes and that the silicate Earth has chondritic Fe isotopic composition.

An important question in modern igneous petrology is the mineralogical nature of Earth's mantle and the extent to which enriched (pyroxenitic) and depleted (peridotitic) lithologies coexist in the mantle and control the chemical composition of magmas sampled at Earth's surface, such as their SiO_2, Ni contents, and Fe/Mn ratios (Humayun et al. 2004; Sobolev et al. 2007). Williams and Bizimis (2014) investigated whether such sources could be traced using iron isotopes. For that purpose, they analyzed the Fe isotopic compositions of mineral separates from peridotite and pyroxenite xenoliths from Hawaii. The bulk rock compositions were recalculated using the known mineral δ^{56}Fe values, Fe concentrations, and modal mineralogy. Other geochemical proxies indicate that the peridotites have experienced variable extents of melt extraction and refertilization (addition of a melt component). The pyroxenites (garnet clinopyroxenite) are high pressure cumulates. Similarly to what Weyer and Ionov (2007) found for peridotites from various settings, Williams and Bizimis (2014) found that the δ^{56}Fe values of bulk peridotites are lower in samples that have experienced the greatest extent of melt extraction. The range of variations measured in peridotites (~0.3‰) is impossible to explain by a simple partial melting model because the most depleted peridotites have only experienced ~10% melt extraction, which would be insufficient to impart large isotopic fractionation to the residue (the iron melt/solid partition coefficient is ~1). A complex history of melt extraction and refertilization is therefore suggested by these data. The pyroxenites have heavy Fe isotopic compositions reaching +0.18‰. The pyroxenite samples with the highest δ^{56}Fe values also have the highest TiO_2 content, presumably because they formed as cumulates from the most evolved magmas and mafic magma differentiation can drive the melt towards heavier Fe isotopic composition through combinations of equilibrium and kinetic processes. This study showed that the mantle may be heterogeneous in its Fe isotopic composition, mirroring the distribution of pyroxenitic vs. peridotitic sources. Such heterogeneity may be visible in lavas in the form of heavy δ^{56}Fe values in hotspot basalts from the Society, Cook-Austral, and Samoan islands (Teng et al. 2013; Konter et al. 2016).

The weight of evidence from Fe isotope measurements of peridotite supports the view that the Fe isotopic composition of the accessible Earth is close to chondritic (Fig. 11). Unfortunately, the iron isotope record in those samples is complicated by the overprinting of melt extraction and metasomatic events, so the community is still debating to what extent those samples are representative of the whole mantle. As discussed below, other samples have been used in order to attempt to constrain its composition.

Komatiites are products of high degrees of partial melting (up to 50%) in the Archean, when the mantle potential temperatures were significantly higher than at present (~300 °C higher than MORBs for the mantle source of Alexo komatiites). High-degree of partial

melting and high temperature should concur to minimize the extent of equilibrium iron isotopic fractionation between the magma and its source, so komatiites may be used as another proxy isotopic composition for the silicate Earth. One difficulty working with komatiites is that they have been serpentinized, which seems to have affected the isotopic composition of Fe (Dauphas et al. 2010). Superimposed on that is the fact that magmatic fractionation of olivine has also induced Fe isotopic fractionation at a bulk rock scale (Dauphas et al. 2010). Using geochemical proxies to avoid these effects, Dauphas et al. (2010) estimated the Fe isotopic composition of the initial lava flow at Alexo to be $\delta^{56}Fe = +0.044 \pm 0.030‰$ (and its $\delta^{25}Mg = -0.138 \pm 0.021‰$; indistinguishable from chondrites). Hibbert et al. (2012) studied the Fe isotopic compositions of komatiites from Belingwe (2.7 Ga), Vetreny (2.4 Ga), and more recent Gorgona (89 Ma). They found correlations with proxies of magmatic differentiation. Correcting for these effects is difficult but Hibbert et al. (2012) proposed that the mantle source may have a lower $\delta^{56}Fe$ value than the value proposed by Dauphas et al. (2010); possibly as low as $-0.13 \pm 0.05‰$. Nebel et al. (2014) measured the Fe isotopic compositions of 3.5 Ga Coonterunah Subgroup and 3.16 Ga Regal Formation komatiites. After correction for crystal fractionation and accumulation, they obtain primary magma $\delta^{56}Fe$ values of −0.06 and ~0‰ for these two komatiite occurrences, consistent with other studies. To summarize, inferring the source Fe isotopic composition of komatiites is fraught with difficulties but available studies hint at a $\delta^{56}Fe$ value lower than MORBs and intraplate basalts. The extent to which those low values reflect prior episodes of melt extraction is uncertain. In addition, several studies point out the importance of immiscible sulfide melt segregation and potentially hydrothermal processes in controlling Fe isotope signatures of komatiites and associated Ni-rich mineralization (Bekker et al. 2009; Hiebert et al. 2013; Hofmann et al. 2014).

Arc basalts and boninites also show rich and complex Fe isotopic variations that have some bearing on Fe isotopic fractionation during partial melting and the composition of the mantle. Boninites are products of high degree flux melting of depleted mantle sources associated with subduction. Dauphas et al. (2009b) measured the Fe isotopic composition of many boninites and found that they have very uniform Fe isotopic composition, clustering around the Fe isotopic composition of chondrites. Those boninites were generated from a highly depleted mantle source that was fluxed with fluids. Hibbert et al. (2012) suggested that the low $\delta^{56}Fe$ value measured in boninites may reflect the fact that their mantle source has low $\delta^{56}Fe$ value inherited from previous partial melting events. This is unlikely to be the case because it would take extraordinary circumstances for melt depletion to shift the Fe isotopic composition of the residue by just the right amount to be offset during a subsequent episode of partial melting to produce lavas that have chondrite-like Fe isotopic compositions. Furthermore, some isotopic scatter would be expected while very little is found. This led Dauphas et al. (2009b) to suggest that Fe isotopic composition of boninites may be representative of the mantle, indicating that it is chondritic. Island arc basalts also show interesting systematics in their iron isotope variations. The samples from the New Britain island arc have Fe isotopic compositions that vary systematically with the distance from the trench and the degree of partial melting (Dauphas et al. 2009b) (Fig. 12). The ones formed by the largest degrees of partial melting with the largest amount of water have Fe isotopic compositions that are almost indistinguishable from the chondritic composition. On the other side of the array, the samples with the lowest degree of partial melting and lowest amount of water fluxing have Fe isotopic compositions similar to MORBs. This is another piece of evidence to support the view that partial melting can fractionate Fe isotopes and that the mantle has chondritic Fe isotopic composition. Nebel et al. (2013) found low $\delta^{56}Fe$ values in the Central Lau Spreading Center located in the Lay back-arc basin similar to signatures found in arcs that they interpreted to reflect the dragging of the proximal arc-front mantle to more distal regions where it can resurface in back arcs. Nebel et al. (2015) presented a study of island arc lavas along the Banda arc, Indonesia. After correction for fractional crystallization and possible crustal contamination, they found that the

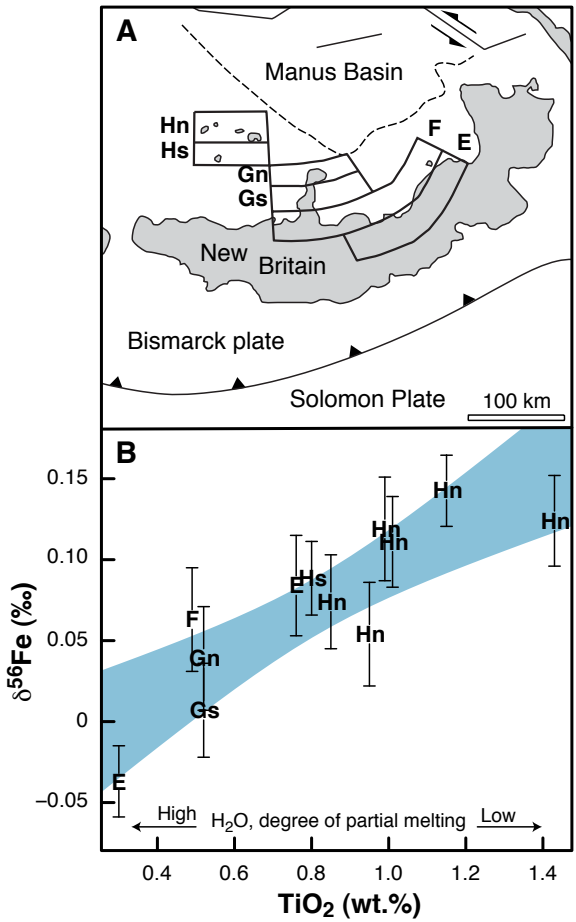

Figure 12. δ^{56}Fe variations in island arc basalts from the New Britain island arc (Dauphas et al. 2009b). The samples farther away from the trench that were fluxed by the smallest amounts of water and correspond to the lowest degrees of partial melting have the heaviest (MORB-like) δ^{56}Fe values. The samples closest to the trench that formed by the highest degrees of partial melting have δ^{56}Fe values similar to chondrites and peridotites.

pristine lavas have distinctly lower δ^{56}Fe values than MORBs, in agreement with the results obtained by Dauphas et al. (2009b). To explain the low δ^{56}Fe values of arc lavas, Dauphas et al. (2009b) suggested that the Fe isotopic fractionation in the source of island arc basalts may be partially suppressed. In this scenario, the starting δ^{56}Fe value of the mantle would be the same in MORBs and IABs but the extent of the fractionation would be reduced in the samples that have experienced the most extensive degree of partial melting and fluxing by subduction fluids. Nebel et al. (2015) instead postulate a different scenario, whereby the Fe isotopic composition would have started the same as mantle source of MORBs (~0‰) but an episode of melt extraction left behind a low δ^{56}Fe mantle, which was subsequently fluxed by oxidizing fluids that generated a second episode of melting. In this scenario, the low δ^{56}Fe value of arc lavas would be inherited from the first melt extraction event. The varied interpretations illustrate the difficulty of inferring the Fe isotopic composition of the mantle from lavas but they also show the strong potential of iron isotopes for tracing petrogenetic processes.

Debret et al. (2016) studied the Fe isotopic composition of serpentinites from Western Alps metaophiolites and found evidence for iron mobility in fluids during subduction, whereby isotopically light iron is lost as Fe(II)–SO_x or Fe(II)–Cl_2 species that could ~~be vectors of~~ oxidation ~~to~~ the mantle wedge.

Partial mantle melting

As discussed above, there still is significant uncertainty on the Fe isotopic composition of the silicate Earth. The fact that all peridotites from various tectonic settings define an average δ^{56}Fe value close to chondritic supports the view that the mantle has a lower δ^{56}Fe value than MORBs and intraplate magmatic rocks. If this is correct, this begs the question of what causes Fe isotopic fractionation during partial mantle melting. A difficulty at the present time is that equilibrium fractionation factors between minerals relevant to Earth's mantle and silicate magmas are not fully established.

Williams et al. (2005) first proposed a quantitative model of iron isotopic fractionation during partial melting. As pointed out by Craddock et al. (2013), some of the calculations violate mass-balance because the residual mantle is calculated to be isotopically fractionated even when the degree of partial melting is ~0, which is impossible (see Fig. 3A of Williams et al. 2005). With this caveat in mind, we can examine some of the parameters and assumptions made by Williams et al. (2005) in calculating melt–solid residue fractionation factors. Williams et al. (2005) used the Fe isotopic compositions of mineral pairs in peridotites to calculate equilibrium fractionation factors between coexisting minerals. They thus used fractionation factors of –0.15‰ between olivine and melt, –0.08‰ between opx and melt, –0.06‰ between cpx and melt, and –0.03‰ between spinel and melt. As discussed by Beard and Johnson (2004b), Zhao et al. (2010), and Roskosz et al. (2015), mineral pairs are often in isotopic disequilibrium in peridotites and it is difficult to infer equilibrium fractionation factors from such samples. Secondly, these fractionations can reflect subsolidus re-equilibration and need to be corrected to mantle solidus temperatures, introducing more uncertainties. Thirdly, there is significant scatter when one plots the δ^{56}Fe values of one mineral against another (olivine vs. pyroxene), so that the inter-mineral fractionation factors are plagued by large uncertainties. With no other data available, Williams et al. (2005) had no other option than to rely on those fractionation factors. They pointed out that the partitioning of more incompatible Fe^{3+} into the melt could in itself impart a heavy Fe isotopic composition to the melt. Williams and Bizimis (2014) built on that early effort. They again used inter-mineral fractionation factors from peridotites as inputs (not corrected for temperature) and left the melt-clinopyroxene as a free adjustable parameter. The melt-residue fractionation factor can be written as,

$$\begin{aligned}\alpha_{\text{residue}}^{\text{melt}} &= \frac{R_{\text{melt}}}{R_{\text{residue}}} = \frac{R_{\text{melt}}}{\sum_i [FeO]_i n_i R_i / \sum_i [FeO]_i n_i} \\ &= \frac{\sum_i [FeO]_i n_i R_{\text{melt}} / R_{\text{cpx}}}{\sum_i [FeO]_i n_i R_i / R_{\text{cpx}}} = \frac{\sum_i [FeO]_i n_i \alpha_{\text{cpx}}^{\text{melt}}}{\sum_i [FeO]_i n_i \alpha_{\text{cpx}}^{i}}\end{aligned} \tag{22}$$

where R is the $^{56}Fe/^{54}Fe$ ratio, n is the modal abundance of each mineral, i denotes a particular mineral in the residue (this is Eqn. 3 of Williams and Bizimis 2014). They used a realistic melting model whereby the modal abundance of the various minerals changes as melting progresses, with minerals like clinopyroxene being consumed more rapidly (they did not explicitly track Fe^{3+} but given that Fe^{3+} is concentrated in cpx and this mineral in preferentially consumed during melting, their model indirectly takes into account the more incompatible and heavy Fe isotopic composition of Fe^{3+}). Even when they set the fractionation between melt and cpx to 0‰, they were able to reproduce the fractionation of ~+0.1‰ for 10% partial melting measured in MORBs. However, because most iron is in olivine, the net fractionation

between the melt and the residue in Williams and Bizimis (2014) is effectively given by the sum $\Delta^{melt}_{cpx} + \Delta^{cpx}_{ol}$, meaning that their conclusion rests on the assumption that the fractionation Δ^{cpx}_{ol} is ~+0.1‰ when $\Delta^{melt}_{cpx} = 0$‰. Clearly, more work is needed to test those assumptions. Because the partition coefficient of Fe is around unity, when the system has reached 10% partial melting, only ~10% of the initial iron has been removed from the system and little change is expected in the Fe isotopic composition of the melt or the residue over such a melting interval (Dauphas et al. 2009b; Williams and Bizimis 2014).

Weyer and Ionov (2007) also investigated partial melting models and used a very simple formulation to describe the isotopic fractionation. They fitted the measured Fe isotopic composition of the peridotites (mantle residues) with Rayleigh distillation models and concluded that the melt–solid fractionation factor had to be between ~+0.1 and +0.3‰ to explain the variations.

Dauphas et al. (2009b) developed a model of isotopic fractionation that is entirely driven by the redox state of iron, meaning that Fe^{2+} in minerals and melt have the same isotopic compositions but that Fe^{3+} is systematically heavier in both minerals and melts relative to Fe^{2+}. They estimated the Fe^{3+}–Fe^{2+} equilibrium fractionation as a function of temperature using NRIXS and Mössbauer data as well as experimental results on the fractionation between peralkaline rhyolitic melt containing ~2/3 Fe^{3+} and pyrrhotite. An important driver of the melt–solid fractionation in this model is the mild incompatibility of Fe^{3+} relative to Fe^{2+}. While Fe^{2+} has a melt/solid equilibrium partition coefficient of ~1, the partition coefficient of Fe^{3+} is ~5. During melting, the melt has a high Fe^{3+}/Fe^{2+} ratio compared to the residual mantle, and because Fe^{3+} tends to have heavy Fe isotopic composition relative to Fe^{2+}, the melt could also have heavy Fe isotopic composition. Dauphas et al. (2009b) could only explain the heavy Fe isotopic composition of MORBs for an Fe^{3+}/Fe^{2+} ratio in the melt that is ~0.24 at 10% partial melting, whereas the measured value is around 0.12–0.16.

Dauphas et al. (2014) generalized this model by allowing for the presence of equilibrium fractionation between Fe^{3+}–Fe^{2+} in minerals, Fe^{3+}–Fe^{2+} in melt, and Fe^{2+}-melt–Fe^{2+}-minerals. The only simplification remaining in this model is that Fe^{2+} has the same Fe isotopic composition in all minerals (e.g., olivine, pyroxene, spinel). Dauphas et al. (2014) and Roskosz et al. (2015) also measured the force constant of iron bonds using the NRIXS synchrotron techniques (see Dauphas et al. 2012 for details) in olivine as well as basaltic glasses and spinels synthesized under various oxygen fugacities (Fig. 13). The glasses were taken as proxies for melts because the NRIXS technique only works with solids. The authors found that the force constants of Fe^{2+} in olivine (197 ± 10 N/m), Al-bearing spinel (207 ± 14 N/m), and basalt (199 ± 15 N/m) are very similar, so that little equilibrium fractionation is predicted for Fe^{2+} in minerals and melts at magmatic temperatures. In contrast, Fe^{3+} in basaltic glasses (351 ± 29 N/m) and spinel (300 ± 18 N/m) displays much higher force constants. The equilibrium fractionation factors at high temperature are directly proportional to differences in force constants between two phases A and B: $\Delta^{B}_{A} = 2{,}904\left(F_B - F_A\right)/T^2$. At a temperature relevant to MORB generation (~1300 °C), the force constants translate into a fractionation of ~+0.2‰ between melt Fe^{3+} and Fe^{2+} and 0.00 ± 0.02‰ between Fe^{2+} in melt and Fe^{2+} in olivine. Using those fractionation factors, Dauphas et al. (2014) could only explain approximately half of the difference in δ^{56}Fe values of MORBs and the inferred mantle value. Several explanations can be considered as to why the model does not predict the full extent of the fractionation that is measured: (1) glasses are imperfect proxies for melts and the fractionation factor is actually higher than that measured by NRIXS, (2) the bonds show some anharmonicity so that extrapolation of room temperature measurements to magmatic temperature suffers from inaccuracies, (3) the bonds stiffen with pressure and the melt is more sensitive to this stiffening, or (4) non-equilibrium (kinetic) processes are at play. Further work is needed to document equilibrium fractionation between magmas and minerals relevant to mantle melting before we can fully understand how iron isotopes are fractionated during partial mantle melting.

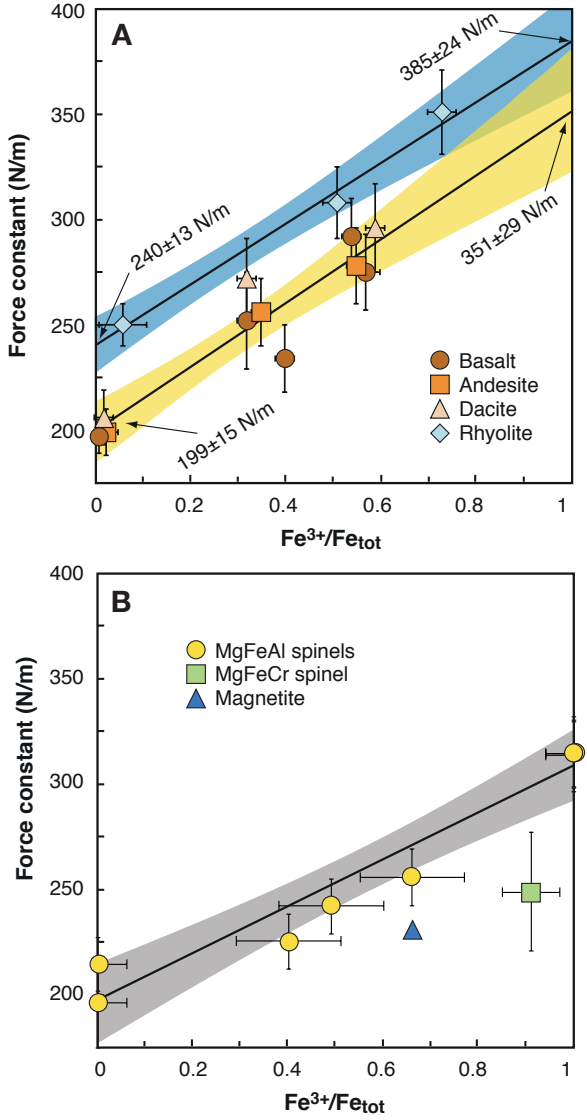

Figure 13. Force constant measurements of basalt, andesite, dacite, rhyolite glasses (A) and spinels (B) as a function of the redox state of iron (Dauphas et al. 2014; Roskosz et al. 2015). At high temperature equilibrium iron isotopic fractionation is directly proportional to the force constant; $1000\ln\beta = 2904 < F > / T^2$.

Impact evaporation and core formation

One motivation to investigate how iron isotopes are fractionated during partial melting is the observation that unlike MORBS, peridotites (and by inference Earth's mantle) have near chondritic Fe isotopic compositions (Fig. 11). Some, however, argue that peridotites are not necessarily representative of the silicate Earth composition and they posit instead that Earth's mantle as a whole has a heavy Fe isotopic composition. Poitrasson et al. (2004) suggested that impact-driven evaporation could be responsible for such heavy isotope enrichment. The

ramifications of this idea have not been tested thoroughly yet but one should note that highly volatile and depleted potassium (Humayun and Clayton 1995a,b) or zinc (Luck et al. 2005; Othman et al. 2006) isotopes are not very fractionated in the Earth relative to chondrites.

Most of iron in the Earth is present in its core (~93%; the rest is in the mantle and crust). If there was any isotopic fractionation between metal and silicate, this offers significant leverage to fractionate iron isotopes in Earth's mantle. High temperature equilibration experiments between metal and silicate (Poitrasson et al. 2009; Hin et al. 2012; Shahar et al. 2015) yield contradictory results (Fig. 8). Shahar et al. (2015) report the largest fractionation beween silicate and metal; -0.08 ± 0.03‰ at 1650 °C. There is some uncertainty on the conditions that prevailed during core formation but Ni and Co impose relatively high pressures of around 40–60 GPa, and a corresponding liquidus temperature of ~3000 K (Li and Agee 1996; Rubie et al. 2011; Siebert et al. 2013). At such elevated temperature, the predicted shift in the Fe isotopic composition of the mantle is divided by a factor of $(3000/1923)^2$, meaning that the fractionation would be at most −0.03‰ between the mantle and core. The results of Hin et al. (2012) suggest that it could be even less. Predicted equilibrium fractionation factors between basaltic glass (Dauphas et al. 2012, 2014) and either fcc iron (Dauphas et al. 2012; Krawczynski et al. 2014b) or bcc iron (Dauphas et al. 2012) based on NRIXS measurements also give different values than the experimental result of Shahar et al. (2015). The system basaltic glass–fcc Fe gives the largest predicted fractionation by NRIXS but even then, at 3000 K, the fractionation between silicate and metal would only be +0.015‰. Starting with a chondritic δ^{56}Fe value of ~0‰, the δ^{56}Fe value of the mantle would be predicted to be between approximately −0.03 and +0.014‰; i.e., much lower than the value of ~+0.1‰ measured in MORBs and intraplate magmatic rocks. Those estimates correspond to relatively low-P conditions and rest on the assumption that the bonds are harmonic, meaning that the fractionation factors can be extrapolated to high-T using a $1/T^2$ relationship, which still needs to be tested. As a side note, basalts from Mars and Vesta have Fe isotopic compositions similar to chondrites, suggesting that even when the core forms at lower temperature than the Earth, metal–silicate fractionation remains small (Fig. 11). This also puts constraints on the amount of sulfur that can be present in the martian core (Shahar et al. 2015).

Polyakov (2009) used NRIXS data on high pressure phases to calculate equilibrium fractionation factors at high pressure-high temperature between metal and high pressure mantle phases ferropericlase and postperovskite. He concluded that at core-mantle boundary conditions, the fractionation between ferropericlase and metal is small ($+0.0006 \pm 0.0030$‰ at 4000 K) but that the fractionation for the system postperovskite and metal could be significant ($+0.04 \pm 0.01$‰ at 4000 K) and possibly sufficient to explain the heavy Fe isotopic composition of the silicate Earth. While intriguing, this conclusion poses two problems. The first one is that postperovskite is irrelevant to core formation conditions (this phase would be unstable; the system most relevant is molten silicate–metal). Furthermore, the NRIXS data on postperovskite used in the calculation are of insufficient quality to reliably derive an equilibrium fractionation factor.

Shahar et al. (2016) and Liu et al. (2016) recently reported NRIXS measurements and ab initio calculations of iron isotopic fractionation between bridgmanite, basaltic glass, pure iron, and Fe-rich alloys of H, C, O Si, S, and Ni. The force constant measurements at high pressure involve the use of diamond anvil cells and are particularly challenging. The conclusion that is emerging from those studies is that the δ^{56}Fe isotopic shift in the mantle induced by core formation is small (<0.03‰ and most likely <0.02‰) because the temperatures involved (~3000–4000 K) were very high, which limited the extent of equilibrium iron isotopic fractionation

Williams et al. (2012) proposed that disproportionation of Fe^{2+} at high pressure in the lower mantle to Fe^0 and Fe^{3+} in bridgmanite could lead to an enrichment in the heavy Fe isotopic composition of the silicate Earth if metal thus formed was removed. However,

Craddock et al. (2013) showed that this does not work from a mass-balance point of view because the mantle only contains ~3% Fe^{3+} (97% Fe^{2+}) and the shift in $\delta^{56}Fe$ value from iron disproportionation would be negligible.

To summarize, some experiments and NRIXS data suggest that the fractionation between silicate and metal at conditions relevant to core formation should be small but more work needs to be done at high pressure on molten compositions to further assess whether this conclusion is correct.

Fractional crystallization, fluid exsolution, immiscibility, and thermal (Soret) diffusion

MORBs and intraplate basalts have a relatively constant $\delta^{56}Fe$ value of ~+0.1‰ (Fig. 11). Poitrasson and Freydier (2005) first showed that granites have heavier Fe isotopic composition than MORB and subsequent work showed that such heavy Fe isotope enrichments are not limited to granite and include rhyolites as well as other rock types such as pegmatites (Heimann et al. 2008; Telus et al. 2012). The $\delta^{56}Fe$ values of silicic rocks correlate broadly with the SiO_2 contents (Fig. 14). Below ~70 wt% SiO_2, igneous rocks have $\delta^{56}Fe$ values that are more or less constant ($\delta^{56}Fe$ between ~+0.08 and +0.14‰) and $\delta^{56}Fe$ then rapidly increases above 70 wt% SiO_2 to reach values as high as +0.4‰. Such large Fe isotopic variations are more commonly encountered in low-*T* environments, begging

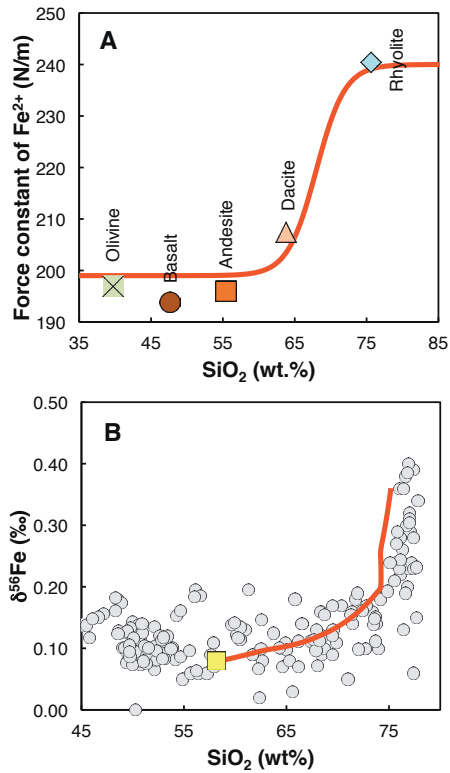

Figure 14. Controls on iron isotopic fractionation in silicic rocks (Dauphas et al. 2014). The force constant of Fe^{2+} shows an abrupt change between 65 and 75 wt% (panel A). This change can partially explain the rapid increase in $\delta^{56}Fe$ values of silicic rocks above 70 wt% SiO_2 (panel B). The circles are data points compiled from the literature and the curve is a fractional crystallization calculation for a starting andesitic melt at fixed fO_2 = FMQ using the Rhyolite–MELTS software and available measured force constant values of glasses, oxides, and silicates.

the question of what causes such large fractionation at magmatic temperatures. Below, we review the scenarios that have been put forward and evaluate their strengths and weaknesses.

Poitrasson and Freydier (2005) favored a scenario of aqueous fluid exsolution. In the later stages of granitic magma body evolution, aqueous fluids rich in chlorine can be exsolved from the magma and mobilize elements such as Zn, Cu, Mo, Au, or Fe that can form porphyry-style mineralizations of economic relevance. For this scenario to work, the fluids that are removed need to have low δ^{56}Fe values so as to drive the Fe isotopic composition of the residual magma towards heavier values. Heimann et al. (2008) extended the work of Poitrasson and Freydier (2005) and showed that both granitic and volcanic rocks have heavy Fe isotopic compositions. They also interpreted these results in terms of fluid exsolution on the basis that the samples with high δ^{56}Fe values have sub-chondritic Zr/Hf ratios. They assert that those low ratios are tracers of fluid exsolution. The model that they propose involves exchange between isotopically heavy magnetite and isotopically light $FeCl_2^0$. There are two arguments against the fluid exsolution model. The first one is that some of the granites that show some of the highest δ^{56}Fe values are of the A-type (anorogenic), which are among the most anhydrous granites encountered and are thought to have formed by partial melting of a dry source. One would not expect those A-type granites to have experienced the most extensive aqueous fluid exsolution (Sossi et al. 2012; Telus et al. 2012). A second argument against the fluid exsolution hypothesis is the study of Zn isotopic compositions and Zn/Fe ratios. Zinc is very mobile in chlorinated fluids and the most silicic magmas show significant Zn/Fe variations that cannot be easily explained by magmatic differentiation, suggesting that indeed Zn was mobilized in those rocks (Telus et al. 2012). If Fe had been mobilized in a similar manner to Zn, one would expect the samples with the highest δ^{56}Fe values to also exhibit fractionated Zn isotopic compositions. Telus et al. (2012) measured Zn isotopes in granites and did not find any significant correlation with iron (i.e., most samples with fractionated δ^{56}Fe values have non-fractionated Zn isotopic composition). Schuessler et al. (2009) measured the Li isotopic composition of samples from the Hekla volcano, Iceland, where Fe isotopic fractionation associated with magmatic differentiation was found. The authors did not detect any variation in the isotopic composition of the fluid-mobile element Li. Those studies suggest that aqueous fluid exsolution plays a minor role in fractionating the isotopic composition of iron in silicic rocks. Some pegmatites, however, show fractionated Zn and Fe isotopic compositions for which fluid exsolution likely played a role (Telus et al. 2012).

Another scenario that has been proposed to explain Fe isotopic variations in some silicic rocks is thermal diffusion. The general idea behind this model is that sills are injected by underplating under a thick volcanic pile that is a barrier to the flow. The magma in the sill is cooled from the top and partially differentiates by thermal migration. It was shown relatively recently that thermal gradients could drive Fe isotopic fractionation in magmas (Huang et al. 2009; Richter et al. 2009b), which led Lundstrom (2009) and Zambardi et al. (2014) to suggest that thermal diffusion could be responsible for some of the isotopic fractionations measured for Fe and other elements in silicic rocks. Zambardi et al. (2014) tested one aspect of the thermal migration model, namely that there should be a depth dependence of the isotopic composition (note that magmatic differentiation would also predict such a relationship). A second test of this idea follows from the observation that in thermal diffusion experiments, all elements can be fractionated isotopically, so that isotopic correlations are expected between elements. Telus et al. (2012) measured the stable isotopic compositions of Fe, Zn, Mg and U in the same samples but failed to detect the correlations expected for thermal diffusion, leading them to conclude that thermal/Soret diffusion was not the main driver of Fe isotopic fractionation in silicic rocks. Zambardi et al. (2014) countered that whether or not fractionation would be expressed depends on the leverage given by the melt/solid partition coefficient. In igneous systems, zinc is geochemically similar to iron (somewhat similar partition behaviors in many minerals), yet no clear isotopic correlation was found between Fe and Zn in the rocks studied by Telus et al. (2012).

Zhu et al. (2015) proposed a scenario to explain the heavy Fe isotopic composition of A-type granites that involves diffusion in a silica-rich immiscible melt. As the silica-rich melt grows at the expense of a Fe-rich magma, iron which is preferentially partitioned in the Fe-rich melt accumulates at the interface and diffuses away from the immiscible silicic melt. One would therefore predict that the immiscible melt and the interface should be enriched in the heavy isotopes of iron (during diffusion, source reservoirs are enriched in the heavy isotopes) while the bulk of the Fe-rich melt should be enriched in the light isotopes of iron (sink reservoirs are enriched in the light isotopes during diffusion because those diffuse faster than heavier ones) (Watson and Müller 2009). This is an intriguing possibility but a significant unknown is the extent to which advective transport of iron from the immiscible liquid interface to the far field can play a role to obliterate diffusion in such a system. Carbonatites, which may have formed by liquid immiscibility, define a large span in δ^{56}Fe values (almost 2‰) whose origin is still uncertain and may involve multiple processes (Johnson et al. 2010).

A third scenario, and in our view the most likely one that applies to the majority of magmatic rocks, is fractional crystallization. Obviously, we cannot exclude that thermal migration or fluid exsolution play some roles in some settings, as was suggested for pegmatites. Fractional crystallization is usually thought to be one of the main drivers behind the chemical differentiation of magmatic rocks. Teng et al. (2008) presented the first evidence that fractional crystallization can fractionate Fe and Mg isotopes. They measured samples from the Kilauea Iki lava lake, which is a crater pit that was filled with lava in 1959 and slowly cooled afterwards. The lava lake was drilled at regular intervals by the USGS. The rocks span a significant range in MgO content, from MgO-rich cumulate rocks to MgO-poor segregation veins. The variations in δ^{56}Fe values span 0.2‰, with heavy isotope enrichments in the more differentiated (more MgO-poor) compositions. Teng et al. (2008) could explain their data with a melt–solid fractionation coefficient of +0.1‰. This fractionation factor does not reflect equilibrium as it was subsequently shown by Teng et al. (2011) and Sio et al. (2013) that the fractionation is driven by kinetic fractionation accompanying Mg–Fe diffusion in olivine (this will be discussed more extensively in the next section). Other localities than Kilauea Iki lava lake have shown somewhat similar trends of isotopic fractionation associated with magmatic differentiation, including the Red Hill intrusion (Tasmania; Sossi et al. 2012), the Cedar Butte volcano (USA; Zambardi et al. 2014), the Hekla volcano (Iceland; Schuessler et al. 2009) and the Bergell intrusion (Switzerland, Schoenberg and von Blanckenburg 2006). Teng et al. (2011) showed that the fractionations that they measured in Kilauea Iki lava lake were due to Fe-Mg inter-diffusion in olivine but this interpretation is obviously not applicable to the overall pattern of δ^{56}Fe variations in silicic rocks and other interpretations/models must be sought. Dauphas et al. (2014) and Foden et al. (2015) used the Rhyolite-MELTS software to model the Fe isotopic composition of silicic rocks. Several important factors were identified that control the evolution of δ^{56}Fe values during fractionational crystallization.

Foden et al. (2015) examined the influence on iron isotopic fractionation of the initial redox state of the magma and whether or not the system is open (oxygen fugacity buffered, equilibrium crystallization) or closed (oxygen fugacity non-buffered, fractional crystallization). To model this process, the authors assumed a pyroxene–melt fractionation factor equal to $-0.17\times10^6/T^2$, corresponding to fractionations of –0.07 and –0.11‰ between pyroxene/ilmenite and melt at the relevant magmatic temperatures (Sossi et al. 2012). The assumed fractionation between magnetite and melt is $+0.13\times10^6/T^2$, corresponding to fractionations of +0.07 to +0.09‰ between magnetite and melt at the relevant magmatic temperatures of 900–1000 °C (Sossi et al. 2012). Those fractionation factors are derived semi-empirically to reproduce some of the iron isotope variations that are observed. In a closed system (non-buffered), Fe^{3+} being more incompatible early on than Fe^{2+}, the magma gets progressively more oxidized as crystallization proceeds. Magnetite crystallizes early, which mitigates the incompatible behavior of Fe^{3+} in

silicate minerals. Because the amount of Fe^{3+} in the closed system scenario is finite, by the time the system has reached 65–70% SiO_2, the Fe^{3+}/Fe_{tot} ratio of the melt is low and the late crystallizing phases are dominated by Fe^{2+}-bearing silicates, so the melt–mineral fractionation factor is positive. There is also very little Fe left in the melt at that point, so mineral crystallization gives a lot of leverage to enrich the residual magma in the heavy isotopes of iron. While this model can reproduce the heavy Fe isotopic composition of some A-type granites that are characterized by large enrichments in the heavy iron isotopes, the mineral-melt fractionation factors are somewhat arbitrary and do not evolve as the Fe^{3+}/Fe^{2+} ratio in the melt evolves (or only indirectly, through the modal abundances of the crystallizing phases, but not because the β-factor of Fe in the melt changes). The onset of the heavy isotope enrichment also does not match very well observations in natural samples, which see a turning point at ~68 wt%, while the model predictions of Foden et al. (2015) predict variations in $\delta^{56}Fe$ values in rocks with lower SiO_2 content.

Dauphas et al. (2014) modeled fractional crystallization of magmas to explain the trends towards heavy iron isotope values of silicic magmas based on the β-factors that they measured for Fe^{2+} and Fe^{3+} in minerals and glasses (taken as proxies for silicate melts) (Fig. 13). Measurements of olivine, pyroxene, spinels, magnetite and other minerals suggest that the β-factors for Fe^{2+} and Fe^{3+} in silicate minerals and oxides are approximately constant and equal to $0.57\times10^6/T^2$ and $0.73\times10^6/T^2$. Measurements of iron force constants in basalt, andesite, dacite, and rhyolite also show that the β-factor of Fe^{3+} in magmas is approximately constant and equal to $1.06\times10^6/T^2$. In a plot of force constant vs. Fe^{3+}/Fe^{2+} ratio, basalt, andesite and dacite define the same trend, corresponding to a β-factor of $0.57\times10^6/T^2$ for Fe^{2+}. The trend defined by rhyolite glasses is, however, shifted towards higher force constant for Fe^{2+}, corresponding to a β-factor of $0.68\times10^6/T^2$. This difference in the behavior of Fe^{2+} in rhyolitic glass is also seen in XANES (X-ray Absorption Near Edge Structure) spectroscopy, which probes the coordination environment of iron (Dauphas et al. 2014). Both NRIXS and XANES thus suggest that somewhere between dacite and rhyolite, the coordination environment of iron changes, so that ferrous iron forms stronger bonds with surrounding atoms. Dauphas et al. (2014) used those fractionation factors in a model of fractional crystallization of an andesitic starting composition using the Rhyolite-MELTS software, assuming buffered oxygen fugacity. They were able to reproduce the trend of $\delta^{56}Fe$ values vs. SiO_2 content, including the inflexion point at ~70wt% (Fig. 14).

The studies of Dauphas et al. (2014) and Foden et al. (2015) showed that fractional crystallization could explain the isotopic variations in silicic igneous rocks, with no need to invoke more exotic phenomena such as magma immiscibility, aqueous fluid exsolution, or thermal diffusion.

A new tool to improve on geospeedometry reconstructions in igneous petrology

Identifying diffusive processes in igneous petrology is important as it is often the only manner by which one can derive timescales and durations of magmatic processes. One such tool is Mg–Fe interdiffusion in olivine (Costa et al. 2008). It is a simple binary diffusion problem with well-established diffusion coefficients (Dohmen and Chakraborty 2007). Furthermore, the exchange coefficient of Mg and Fe between olivine and melt varies little depending on the melt composition (Toplis 2005), so that it is straightforward to relate trends of magmatic differentiation to crystal boundary conditions. A difficulty with Mg–Fe zoning in olivine (and other chemical profiles in other minerals) is that such zoning cannot always unambiguously be ascribed to diffusion. Let us consider two end-member scenarios to illustrate this point. Zoning in olivine is established in response to magmatic differentiation. Because olivine incorporates preferentially Mg relative to Fe, the magma evolves towards higher Fe/Mg ratio as crystallization proceeds. If the rate of diffusion in olivine is much slower than the rate of magmatic differentiation or cooling, then at each time step, the olivine that grows is in equilibrium with a magma that becomes more Fe rich. The growing olivine

will thus develop normal zoning with a composition that becomes more fayalitic from core to rim. In a second end-member scenario, let us consider an early formed olivine that is put into contact with a more evolved magma. Iron will diffuse in the olivine while Mg will diffuse out, creating a zoning pattern with a composition that is more fayalitic from core to rim. In the second scenario, zoning is entirely attributable to diffusion and one can calculate magmatic timescales from it. In the first scenario, zoning is due to crystal growth with no diffusion, so any timescale that one derives from it is meaningless. It is most often impossible to distinguish the two zoning patterns. Trace elements have been used for that purpose (Costa et al. 2008) but they suffer from the fact that the partitioning behavior of those trace elements are not always well constrained, the magma body evolution is uncertain leading to uncertainties in the boundary condition, and the diffusion coefficients are also uncertain. Magnesium and iron isotopes are fractionated during diffusive processes, which led Dauphas et al. (2010) and Teng et al. (2011) to suggest that the two modes of zoning could be distinguished (or their contributions teased apart when both processes are at play). Those authors showed that the Fe isotopic composition of olivine in Alexo komatiite and Kilauea Iki lava lake were affected by diffusion. Sio et al. (2013) and Oeser et al. (2015) built on these early studies and reported *in situ* Fe isotope measurements of zoned olivines (Fig. 4). An important uncertainty remains regarding the β-value of Mg and Fe, with measurements of natural samples suggesting that it should be around 0.084 to 0.16 for Mg and 0.16 to 0.27 for Fe (the ratio $\beta Fe/\beta Mg$ is better constrained to be 1.8 ± 0.3) (Sio et al. 2013; Oeser et al. 2015). As the β-values are refined and *in situ* measurement techniques are improved, it will be possible to inverse Fe isotope data in olivine (or other minerals) to reconstruct the thermal and crystal growth history of a magma (Sio and Dauphas 2016). The study of zoned minerals evolved from characterizing the petrography of the samples by optical microscopy to *in situ* analyses of major, minor and trace elements by microprobe. The next step in studies of zoned minerals is *in situ* stable isotopic analyses, which provide a unique tool to tease apart diffusion from crystal growth.

IRON BIOGEOCHEMISTRY

Microbial cycling of Fe isotopes

Dissimilatory iron reduction (DIR). The importance of Fe(III) oxides as electron acceptors for anaerobic respiration in Fe-rich modern sediments is widely recognized (Lovley et al. 1987; Roden 2004) and may have been associated with some of the earliest forms of metabolism on Earth (Vargas et al. 1998). Mineralogical products of dissimilatory Fe(III) reduction that may be preserved in the rock record include magnetite, Fe carbonates, and sulfides. In pioneering studies, Bullen and McMahon (1998) and Beard et al. (1999b) reported that the $\delta^{56}Fe$ value of dissolved Fe(II) produced by dissimilatory Fe-reducing bacteria was fractionated by ~−1.3‰ relative to the ferrihydrite substrate. Subsequent results have been extended to different DIR bacteria, growth conditions, and substrates (Beard et al. 2003a; Icopini et al. 2004; Crosby et al. 2005, 2007; Johnson et al. 2005; Wu et al. 2009; Tangalos et al. 2010; Percak-Dennett et al. 2011). In particular, at high reduction rates, Fe(II) produced by DIR has $\delta^{56}Fe$ values that are up to 2.6‰ lower than ferric substrate, possibly reflecting the effect of adsorption of heavy Fe(II) on hydrous ferric oxide. However, Crosby et al. (2005, 2007) have shown that the low $\delta^{56}Fe$ values for aqueous Fe(II) produced by DIR reflect isotopic exchange among three Fe inventories: aqueous Fe(II) [$Fe(II)_{aq}$], sorbed Fe(II) [$Fe(II)_{sorb}$], and a reactive Fe(III) component on the ferric oxide surface [$Fe(III)_{reac}$]. The fractionation in $^{56}Fe/^{54}Fe$ ratios between $Fe(II)_{aq}$ and $Fe(III)_{reac}$ was –2.95‰, and independent of the ferric Fe substrate (hematite or goethite) and bacterial species, indicating a common mechanism for Fe isotope fractionation during DIR. Moreover, the $Fe(II)_{aq}$–$Fe(III)_{reac}$ fractionation in $^{56}Fe/^{54}Fe$ ratios during DIR is identical within error of the equilibrium $Fe(II)_{aq}$–ferric oxide fractionation

in abiological systems at room temperatures (Johnson et al. 2002; Welch et al. 2003; Wu et al. 2011). This suggests that the role of bacteria in producing Fe isotope fractionations during DIR lies in catalyzing coupled atom and electron exchange between $Fe(II)_{aq}$ and $Fe(III)_{reac}$ so that equilibrium Fe isotope partitioning occurs (Crosby et al. 2007). Other parameters such as the removal or local accumulation of $Fe(II)_{aq}$, presence of dissolved Si, and pH may also affect the iron isotopic record of DIR in sediments (Wu et al. 2010).

Bacterial Fe oxidation. Although chemical oxidation of ferrous iron is thermodynamically favored during the interaction of reduced fluids with oxygenated waters, bacterial Fe(II) oxidation may prevail in acidic, microaerobic or anoxic environments. Microorganisms that oxidize Fe(II) to generate energy for growth include those that couple Fe(II)-oxidation to the reduction of nitrate at neutral pH (Benz et al. 1998), or to the reduction of oxygen at either low (Edwards et al. 2000), or neutral pH (Emerson and Moyer 1997), and the anaerobic Fe(II)-oxidizing phototrophs (Widdel et al. 1993).

Croal et al. (2004) investigated Fe isotope fractionation produced by Fe(II)-oxidizing phototrophs under anaerobic conditions. Among key results, the ferrihydrite precipitate has a δ^{56}Fe value that is ~+1.5‰ higher than the aqueous Fe(II) source. Since the degree of isotopic fractionation is not correlated with the rate of oxidation (controlled by changing the light intensity), it has been suggested that kinetic isotope effects were not of great importance in controlling the fractionation factor. The fractionation factor, however, is higher than for abiotic Fe(II) oxidation experiments (about 1‰, Bullen et al. 2001) and lower than for equilibrium fractionation between aqueous Fe(II) and Fe(III) of 3‰ at room temperature (Welch et al. 2003).

In fact, it has been difficult to determine Fe isotope fractionation between aqueous Fe(II) and poorly crystalline ferric hydrous oxides (HFO, or ferrihydrite) due to the rapid transformation of the latter to more stable minerals. Wu et al. (2011) experimentally determined the equilibrium Fe(II)–HFO fractionation factor using a three-isotope method. Iron isotope exchange between Fe(II) and HFO was rapid and near complete in the presence of dissolved silica. Equilibrium Fe(II)–HFO ^{56}Fe/^{54}Fe fractionation factors of −3.17‰ were obtained for HFO plus silica. In contrast, when coprecipitates of Si–HFO form during the experiment, a smaller fractionation factor of −2.6‰ was obtained, possibly reflecting blockage of oxide surface sites by sorbed silica leading to incomplete isotope exchange.

Magnetotactic bacteria. Magnetotactic bacteria (MB) are prokaryotes participating in the chemical transformation of Fe and S species via both redox and mineral precipitation processes. MB precipitates intracellular single domain ferromagnetic iron oxide (magnetite) or iron sulfide (greigite) minerals, causing them to respond to geomagnetic fields. These bacteria are globally distributed in suboxic to anoxic freshwater (Frankel et al. 1979; Spring et al. 1993) and marine sediments, soils, and stratified marine water columns (Bazylinski et al. 2000; Simmons et al. 2004).

Initial Fe isotope studies of magnetite produced by MB (Mandernack et al. 1999) have shown no detectable fractionation when either an Fe(II) or Fe(III) source was used in the growth media. These results contrast strongly with recent experimental work of Fe isotope fractionation during magnetite formation coupled to dissimilatory hydrous ferric oxide reduction, which shows large isotopic fractionation between Fe in magnetite and Fe in the fluid (Johnson et al. 2005). However, this does not preclude that there is an isotopic effect produced by MB because only two strains were investigated over a restricted range of laboratory conditions. In particular, Fe isotope fractionation might be dependent on the kinetics of Fe uptake by MB, which may vary with Fe concentration, Fe redox state, and the presence of Fe chelators (Schuler and Baeuerlein 1996). In a recent study, Amor (2015) investigated the chemical and isotopic properties of magnetite produced by *Magnetospirillum magneticum* AMB−1 model magnetotactic bacterium. Results suggest that AMB−1 bacteria preferentially incorporate heavy iron isotopes within the cell. Magnetite is then produced from partial reduction of iron accumulated within the cell. This led to magnetite crystal mineralizations that were enriched

in light isotopes and displayed δ^{56}Fe values from −1 to −1.5‰ lower than those of the growth medium. Magnetite biomineralizations may therefore have the potential to produce magnetite enriched in light iron isotopes relative to the precipitation solution. Amor et al. (2016) detected deviation from mass-dependent fractionation in ^{57}Fe in growth media and magnetite produced by magnetotactic bacterium *M. magneticum* strain AMB−1. This is the first documented iron isotopic anomaly induced by natural processes. The anomaly was only present when the growth medium was Fe(III)-quinate but was absent from Fe(II)-ascorbate experiments.

Fe isotopes in plants, animals, and humans

Iron is essential for all living organisms as it is used to maintain cellular homeostasis and plays a vital role in oxygen and carbon dioxide shuttling as well as enzymatic reactions required for DNA and hormone synthesis. In plants, Fe is required for iron-sulfur proteins and as a catalyst in enzyme-mediated redox reactions (e.g., Briat and Lobreaux 1997). Although the use of Fe isotopes as robust microbial biosignatures still remains controversial, a rapidly growing number of studies reported that higher organisms, including plants, animals and humans produce in fact the largest isotope fractionations.

In an initial study, Guelke et al. (2007) proposed that Fe isotope fractionation patterns in plants are related to two different strategies that plants have developed to incorporate Fe from the soil:

- strategy I: incorporation and potentially reduction of Fe(III) in soils resulting in the uptake of isotopically light Fe by up to 1.6‰ relative to available Fe in soils;
- strategy II: complexation with siderophores resulting in the uptake of iron that is 0.2‰ heavier than that in soils.

It remains however unclear whether redox-related plant metabolism could be the main cause of isotopic variation in the biogeochemical cycling of Fe. Guelke-Stelling and von Blanckenburg (2012) investigated strategy I and II plants grown in nutrient solutions and proposed a non-reductive translocation process in strategy I plants. Other studies determined the Fe isotopic composition of different plant parts, including the complete root systems, seeds, leaves and stems in order to distinguish between uptake and in-plant fractionation processes (von Blanckenburg et al. 2009; Kiczka et al. 2010; Moynier et al. 2013; Akerman et al. 2014; Arnold et al. 2015). The overall range of fractionation among the different plant tissues and organ systems was up to 4.5‰ (Kiczka et al. 2010), and may result from at least 4 fractionation steps: (1) before active plant uptake, probably during mineral dissolution; (2) during selective uptake of Fe at the plasma membrane; (3) during translocation processes and storage in plants; (4) during remobilization and transfer from old to new plant tissue, further changing the isotopic composition over the season. Ab initio calculations (Moynier et al. 2013) also provided a mechanistic explanation to the enrichment in heavy Fe isotopes in roots of strategy-II plants (by about 1‰ for the δ^{56}Fe value) relative to the upper parts of the plants.

A small number of research groups worldwide are currently using Fe isotopes for biomedical research, with the aim to develop new methods for medical diagnosis on the basis of Fe isotopic analysis of biofluids, either for diseases or metabolism studies (Albarede 2015; Vanhaecke and Costas-Rodriguez 2015; Larner 2016). Following the pioneering study of Walczyk and von Blanckenburg (2002), subsequent studies further improved our understanding of Fe isotope fractionation in the human body (Krayenbuehl et al. 2005; Walczyk and von Blanckenburg 2005; Albarede et al. 2011; Hotz et al. 2011, 2012; Van Heghe et al. 2012, 2013, 2014; Hotz and Walczyk 2013; Jaouen et al. 2013a; von Blanckenburg et al. 2013, 2014). It is now well-established that human blood and muscle tissues are enriched in light Fe isotopes by 1 to 2‰ when compared to the diet intake. It was also found that blood yields the lightest Fe isotopic composition, while the liver is less enriched in light isotopes. The same picture was

also observed in other mammals such as mice and sheeps (Balter et al. 2013). Although the exact mechanisms of Fe isotope fractionation during intestinal uptake, binding to the protein transferrin and transport within the blood plasma to various organs and tissues remain under investigation, it appears that whole blood Fe isotopic composition is an indicator of the efficiency of dietary Fe absorption (Hotz and Walczyk 2013). The isotopic composition of whole blood is also related to serum ferritin level, typically seen as a measure for the amount of Fe stored in the liver (Van Heghe et al. 2013). As a consequence, hereditary hemochromatosis, a disease characterized by excessive Fe uptake, is also reflected in the Fe isotopic composition of blood (Krayenbuehl et al. 2005). Finally, recent studies agree that the gender-based difference in whole blood Fe isotopic composition results from the response of the organism to the Fe loss accompanying menstruation rather than differential intestinal absorption between female and male (Van Heghe et al. 2013, 2014; Jaouen and Balter 2014). Considering a simple isotopic mass balance, it is possible that the isotopically heavier Fe in women's blood relative to that of men could be due to higher hepatic mobilization of Fe by women as a result of menstrual Fe loss, which represents up to 40% of the monthly dietary uptake (Harvey et al. 2005). With the assumption that Fe isotopic ratios in bones reflect the patterns observed in blood (Jaouen et al. 2012), Fe isotopes might be used in paleoanthropology as sex indicators for past populations or as proxies for the age at menopause in ancient populations.

Finally, considering the range of Fe isotopic compositions in plants and animals, it is likely that Fe isotopes may also provide important information on trophic levels and food chains, in particular for marine animals. Poigner et al. (2015) measured the Fe isotopic composition in bivalve hemolymph, which represents the product of cutaneous (gills) and intestinal (digestive tract) assimilation, while Emmanuel et al. (2014) measured the Fe isotopic composition of chiton teeth capped with magnetite (chitons are marine molluscs). Overall, δ^{56}Fe ranged from near 0 to −1.9‰, which results from either (i) physiologically controlled processes that lead to species-dependent fractionation; (ii) diet-controlled variability due to different Fe isotope fractionation in the food sources; and (iii) environmentally controlled fractionation that causes variation in the isotopic signatures of bioavailable Fe in the different regions. Jaouen et al. (2013b) found Fe isotopic fractionation in mammal trophic chains between plants, herbivores, and carnivores. Integrated studies, combining Fe isotopic composition of the different environmental compartments (seawater, sediments, porefluid, phytoplankton, marine particles) and the different tissues or organs of the organism are required to further understand what controls iron isotope variations in plants and animals.

FLUID–ROCK INTERACTIONS

In both terrestrial and marine environments Fe cycles between the solid and dissolved phases, and such phase transfers are associated with iron isotope fractionation. In this section we discuss what is known about the fractionation of Fe isotopes during fluid–mineral interactions in hydrothermal systems, soils, and rivers, as well as the application of δ^{56}Fe as a tracer for ore formation processes in the field of economic geology.

High- and low-temperature alteration processes at the seafloor

Past studies have demonstrated the complexity and diversity of seafloor hydrothermal systems and have highlighted the importance of subsurface environments where a variety of chemical reactions between seawater, rocks and hydrothermal deposits is taking place over a wide range of temperatures (German and VonDamm 2003; Hannington et al. 1995; Humphris et al. 1995). Alteration of oceanic crust by seawater is one of the most important processes controlling the global fluxes of many elements (Staudigel and Hart 1983; Wheat and Mottl 2004) and the composition of the aging oceanic crust (Alt 1995).

Leaching of Fe from basalts, either at high- or low-temperature, typically results in the preferential release of the lighter Fe isotopes (Rouxel et al. 2003). High-temperature (>300 °C) vent-fluids yield a range of Fe isotopic compositions that are systematically shifted toward light δ^{56}Fe values compared to igneous and mantle rocks (Sharma et al. 2001; Beard et al. 2003b; Severmann et al. 2004; Rouxel et al. 2008a, 2016; Bennett et al. 2009). Values as low as −0.67‰ and as high as −0.09‰ have been measured in hydrothermal vent fluids along the Mid-Atlantic Ridge and East Pacific Rise (EPR). The heaviest values have been reported for high-temperature hydrothermal fluids from ultramafic-hosted systems (e.g., Rainbow field; Severmann et al. 2004) while lighter values were reported for Fe-depleted vents from basaltic-hosted vent sites (e.g., Bio-vent, Rouxel et al. 2008a). In general, high-temperature hydrothermal fluids from basaltic-hosted fields have a restricted range from −0.3 down to −0.5‰ (Rouxel et al. 2008a, 2016; Bennett et al. 2009).

Potential processes controlling the variability of Fe isotopes in hydrothermal fluids include phase separation, high-temperature basalt alteration, and subsurface processes leading to Fe precitation or remobilization below seafloor. Although phase separation is one of the fundamental processes controlling mid-ocean ridge vent fluid chemistry (Von Damm 1988; Von Damm et al. 1995), several lines of evidence suggest only limited Fe-isotope fractionation during this process. First, Beard et al. (2003b) measured δ^{56}Fe values of both the vapor and brine phases from the Brandon Vent at EPR 21.5°S and found less than 0.15‰ difference between these two fluids. Secondly, although not spatially related, Fe isotopic compositions of the high salinity fluid at K-vent at EPR 9°30'N (i.e., Na above seawater) does not differ significantly from lower salinity, vapor-rich fluids at Tica vent at EPR 9°50'N (Rouxel et al. 2008a). Thirdly, a recent experimental study of Fe isotope fractionation during phase separation in the NaCl–H_2O system (Syverson et al. 2014) yielded a maximum Fe isotope fractionation between the vapor and liquid of 0.15 ± 0.05‰ with, in most cases, variations of δ^{56}Fe values indistinguishable within analytical uncertainties.

Hence, the general enrichment in light Fe isotopes in vent fluids relative to volcanic rocks should be explained by two alternative mechanisms (Rouxel et al. 2003, 2004, 2008a):

(1) high-temperature alteration of basalt and the formation of isotopically heavy secondary minerals (e.g., Mg–Fe amphibole) in the high-temperature reaction zone. This mechanism has been already observed during low-temperature alteration of basalts at the seafloor (Rouxel et al. 2003). In particular, highly altered basalts that are depleted in Fe by up to 80% from their original Fe concentration displayed an increase in δ^{56}Fe values relative to fresh values (up to 1.3‰), which suggests preferential leaching of light Fe isotopes (between −0.5 and −1.3‰) during alteration.

(2) precipitation of isotopically heavy pyrite in subsurface environments or in the reaction zone. Using first-principle methods based on density-functional theory (DFT) and Mössbauer spectroscopy methods, previous theoretical studies have demonstrated that pyrite should be enriched in heavy Fe isotopes under equilibrium conditions (Blanchard et al. 2009; Polyakov and Soultanov 2011; Blanchard et al. 2012). Using the reduced isotopic partition function ratios of FeS_2 and Fe(II)-aquo-chloro complexes, the isotope fractionation between FeS_2 and $Fe(II)_{aq}$ is estimated to be +1.0 to +1.5 at 350 °C. The experimentally determined equilibrium pyrite–hydrothermal fluid Fe isotopic fractionation also agrees with theoretical and spectrally based predictions (Syverson et al. 2013). Under hydrothermal conditions (300–350 °C, 500 bars) in NaCl- and sulfur-bearing aqueous fluids, the fractionation between FeS_2 and $Fe(II)_{aq}$ was determined to be +0.99 ± 0.29‰ (Syverson et al. 2013). Hence, in the case of pyrite precipitation in subsurface environments due to conductive cooling of the fluids, near equilibrium Fe-isotope fractionation is expected which should result in the preferential partitioning of isotopically light Fe in the hydrothermal fluids. This suggests that pyrite acts as important mineral buffer in the composition of high-temperature hydrothermal fluids.

Rivers and soils

In soils and river systems, isotopic fractionations are generally small (often less than ~0.5‰), and isotopically light Fe tends to be preferentially leached from source rocks into the dissolved phase. An early observation found that rivers with a high suspended load were similar to continental δ^{56}Fe, while rivers with a higher proportion of Fe in the dissolved phase typically had light δ^{56}Fe signatures (Fantle and DePaolo 2004). In the Amazon River, dissolved and suspended loads have similar δ^{56}Fe values to continental crust, while in the organic-rich "black" Negro River, there is a preferential concentration of lighter isotopes in the dissolved phase and heavier isotopes in the particulate phase (Bergquist and Boyle 2006). A more extensive subsequent study of δ^{56}Fe values in the Amazon River and its tributaries found similar results: δ^{56}Fe was isotopically light compared to continental material in organic rich rivers with a low suspended load, and similar to continental sources in rivers with more suspended material (Poitrasson et al. 2014). Direct measurements of the suspended material in the Amazon river system demonstrated that it also had an Fe isotope signature similar to the continental source (dos Santos Pinheiro et al. 2013).

While it is more common to find that rivers are isotopically light compared to continental material, many exceptions have been found. The North River in Massachusetts, for example, had dissolved δ^{56}Fe up to +0.3‰ (Escoube et al. 2009). Ingri et al. (2006) focused on the colloidal size fraction within the dissolved phase and found that δ^{56}Fe was dependent on the type of colloids present, with isotopically lighter organic colloids as low as −0.13‰ and heavier oxyhydroxide colloids up to +0.3‰. Escoube et al. (2015) and Ilina et al. (2013) found that larger Arctic rivers had δ^{56}Fe similar to continental material, while smaller rivers could vary dramatically from −1.7 to +1.6‰, which they attributed to active redox cycling and colloid formation. Conversely, a glacial outflow river on Svalbard had nearly continental δ^{56}Fe even over large changes in dissolved Fe concentrations, pointing to the lack of active redox cycling in this environment (Zhang et al. 2015).

Anthropogenic contamination may also influence riverine δ^{56}Fe values. River and lake samples from the South China Karst region show suspended material with δ^{56}Fe values ranging from −2.0 to +0.4‰, with the most negative values being attributed to biological activity and contaminated coal drainages (Song et al. 2011). Chen et al. (2014) found that anthropogenic Fe could be traced in the Seine river because of its isotopically light δ^{56}Fe signature.

Much of the water in rivers, and nearly all of the Fe, originates in the surrounding soils when meteoric water dissolves iron-containing soil minerals. Studies of redoximorphic soils showed a depletion of light isotopes during anoxic soil dissolution, and a subsequent precipitation of that isotopically light Fe under oxic conditions (Wiederhold et al. 2007b). In contrast, soils from a rainforest in Cameroon did not have variable δ^{56}Fe (Poitrasson et al. 2008). Guelke et al. (2010) found that the most mobile phases in soil were isotopically light, while the residual silicate fraction was isotopically heavy, suggesting the preferential release of lighter Fe isotopes during silicate weathering. Similarly, Kiczka et al. (2010) found an enrichment in lighter Fe isotopes in Fe oxyhydroxides, which they attributed to the preferential leaching of light Fe from silicates in an alpine glacier and subsequent precipitation of this Fe as oxyhydroxides. Recently, field observations of the preferential release of lighter Fe isotopes during weathering has been reproduced under experimental conditions where the redox conditions of a soil were artificially manipulated (Schuth et al. 2015).

Mineral deposits

One motivation to study the behavior of Fe isotopes in the natural world is to better understand how economically important iron ore deposits are formed. Many studies have therefore characterized the distribution of δ^{56}Fe within various different rocks and minerals

collected in active mining regions in order to better understand the processes by which these deposits were formed. Recent examples include the Xishimen (Chen et al. 2014), Han-Xing (Zhu et al. 2016) and Gaosong (Cheng et al. 2015) deposits in China, the Grangesberg Mining District in Sweden (Weis et al. 2013), nickel deposits in Zimbabwe (Hofmann et al. 2014), the Schwarzwald region in Germany (Horn et al. 2006; Markl et al. 2006), Sn–W deposits in Tasmania (Wawryk and Foden 2015), and iron oxide–apatite ore deposits in Chile (Bilenker et al. 2016). The study of Fe isotope systematics in modern systems such as hydrothermal vents and marine and terrestrial sediments can also inform our understanding of how economically important deposits (e.g., volcanogenic massive sulfide) form.

Rouxel et al. (2004, 2008b) and Toner et al. (2016) investigated coupled Fe- and S-isotope systematics of sulfide deposits from the East Pacific Rise at 9–10°N and Lucky Strike vent fields to better constrain processes affecting Fe-isotope fractionation during the formation and aging of sulfide deposits at the seafloor. The results showed systematically lower δ^{56}Fe and δ^{34}S values in marcasite/pyrite relative to chalcopyrite and hydrothermal fluids within a single chimney and suggest isotope disequilibrium in both Fe- and S-isotopes. The concomitant Fe and S-isotope fractionations during pyrite/marcasite precipitation are explained by (1) isotopic S-exchange between fluid H_2S and SO_4^{2-} during precipitation of pyrite from FeS precursors by reaction with thiosulfate and (2) rapid formation of pyrite from FeS, thus preserving negative Fe-isotope fractionation factors during FeS precipitation. In contrast, δ^{56}Fe and δ^{34}S values of pyrite precipitated in massive sulfides, either in the subsurface during conductive cooling of the fluid (i.e., slow rate of precipitation) or during multiple stages of remineralization, are expected to be similar to the δ^{56}Fe and δ^{34}S values of the hydrothermal fluid. This hypothesis is consistent with the limited range of δ^{56}Fe values between high-temperature, Fe-rich black smokers and lower temperature, Fe-poor vents suggesting minimal Fe-isotope fractionation during subsurface sulfide precipitation. It is also consistent with previous work showing opposite Fe-isotope fractionation factors during kinetic Fe-sulfide (mackinawite) precipitation (Butler et al. 2005) and equilibrium pyrite precipitation (Polyakov et al. 2007).

Although still not widely applied, Fe isotopes may provide useful application to distinguish hydrothermal vs. magmatic formation pathways, and address potential reservoir effects due to sulfide precipitation during subsurface cooling of the hydrothermal fluid. Furthermore, the effects of equilibrium or kinetic precipitation of sulfide pairs (pyrite–chalcopyrite) and the temperature of precipitation may be traced using Fe isotopes. Both reservoir effects and partial Fe equilibrium may result in contrasted Fe isotopic compositions in co-existing chalcopyrite and pyrite from the Grasberg Cu–Au porphyry and its associated skarn deposits (Irian Jaya, West New Guinea) (Graham et al. 2004).

Combined Δ^{33}S and δ^{56}Fe analyses have been also applied to determine the source(s) of sulfur in Archean komatiite-hosted Fe–Ni sulfide deposits. Samples were collected from Ni-rich sulfide deposits from (1) the ~2.7-Ga Hart komatiite, Abitibi greenstone belt, Ontario, Canada (Hiebert et al. 2016); (2) the ~2.71-Ga Agnew–Wiluna and Norseman–Wiluna greenstone belts of Western Australia and the time-equivalent Abitibi greenstone belt (Bekker et al. 2009); (3) the ~2.7-Ga volcano–sedimentary sequences of the Zimbabwe craton (Trojan and Shangani mines) (Hofmann et al. 2014); (4) the ~2.6-Ga Tati greenstone belt and the Phikwe Complex of Eastern Botswana (Fiorentini et al. 2012); (5) the ~1.3-Ga Voisey's Bay deposit, Labrador, Canada (Hiebert et al. 2013). While Δ^{33}S values suggest that sulfur in Archean komatiite-hosted Fe–Ni sulfide deposits comes from mixing of hydrothermally remobilized magmatic and sedimentary sulfur, Fe isotopes of sulfides from these deposits show a relatively small range of negative δ^{56}Fe values, consistent with high-temperature fractionations in magmatic systems at high silicate magma / sulfide melt ratios.

Iron isotopes have also been used to decipher the origins of detrital pyrite in Archean sedimentary rocks. Rounded grains of pyrite are a common component of conglomerate hosted gold and uranium deposits of the Mesoarchaean Witwatersrand basin of South Africa. Different sources for detrital pyrite have been discussed, including sedimentary, igneous, and various hydrothermal origins (Barton and Hallbauer 1996; England et al. 2002), while the source of gold remains poorly constrained in this model (Robb and Meyer 1990). The placer model (deposit of pyrite-bearing sand or gravel in the bed of a river or lake) has been challenged by several workers who ascribe these grains to post-depositional pyritisation of non-sulphidic (e.g., Fe-oxide) detrital grains during hydrothermal alteration (e.g., Barnicoat et al. 1997; Phillips and Law 2000). Multiple S ($\delta^{34}S$ and $\delta^{33}S$) and Fe ($\delta^{56}Fe$) isotope analyses of rounded pyrite grains from 3.1 to 2.6 Ga conglomerates of southern Africa (Hoffmann et al. 2009) confirm their detrital origin, which supports anoxic surface conditions in the Archaean.

IRON BIOGEOCHEMICAL CYCLING IN THE MODERN OCEAN

The biogeochemical cycling of Fe in the modern ocean is of particular interest because Fe limits the growth of phytoplankton in so much of the surface ocean, meaning that Fe has a large impact on marine biology and carbon cycling. The sources of Fe to the ocean are not well constrained, but Fe isotope 'fingerprinting' of Fe from various sources may provide a new tool to trace Fe as it mixes into the global ocean. Additionally, Fe stable isotopes may be used in order to better understand the internal cycling of Fe by biological and chemical processes in the marine realm.

The importance of iron in the global ocean

In high-nutrient low-chlorophyll (HNLC) regions of the world ocean, Fe is the element primarily responsible for limiting the growth of phytoplankton. Before the importance of Fe was fully understood, a wide variety of hypotheses had been considered about why there was an abundance of major nutrients (N, P, and Si) in HNLC regions such as the Southern Ocean, subarctic North Pacific, and the Equatorial Pacific. Prior hypotheses included light limitation and lack of grazing pressure (e.g., Landry et al. 1997). With the advent of trace-metal clean sampling techniques, however, it became clear that Fe concentrations in HNLC regions were very low (<1 nM) and the possibility of Fe limitation was considered. Work by John Martin and others at Monterey Bay Aquarium Research Institute was crucial to understanding the importance of Fe, including early experiments showing that cultures of phytoplankton from HNLC regions responded to Fe additions (Martin and Fitzwater 1988), and advancing the so-called 'iron hypothesis' that changes in dust Fe flux to the oceans was responsible for glacial–interglacial changes in atmospheric carbon dioxide (Martin 1990). The work of Martin and colleagues culminated with one of the most dramatic experiments in the history of oceanography, the addition of Fe to a large patch of the HNLC equatorial Pacific which resulted in a massive Fe-fertilized phytoplankton bloom (Martin et al. 1994).

Iron limitation plays a crucial role in marine biogeochemistry in both the modern and the past ocean. Modeling studies suggest that primary productivity in about a quarter of the global ocean is limited by Fe (Moore et al. 2002).There is also strong evidence of a correlation between dust flux to the Southern Ocean and glacial-interglacial climate cycles (Martinez-Garcia et al. 2011; Murray et al. 2012), although the full 'iron hypothesis' that Fe is the primary cause of glacial-interglacial cycles has not been supported by paleoceanographic research.

While there is no doubt about the importance of Fe to marine biogeochemical cycles, important questions remain. Iron stable isotopes may help to address two key questions about the marine biogeochemical cycling of Fe: What are the sources of Fe to the oceans? What are the chemical and biological processes that cycle Fe within the oceans?

Sources and sinks for Fe in the ocean

One of the most promising applications of Fe isotopes in the marine realm is to trace various sources of Fe to the ocean (Fig. 15). Often the measurement of Fe concentrations alone is not sufficient to determine what was the original source of Fe into the ocean, but because different sources often have a unique δ^{56}Fe signature, analysis of seawater δ^{56}Fe may be used to constrain these sources. Four different sources of Fe have been proposed as contributing significantly to global marine productivity; 1) atmospheric dust, 2) hydrothermal vents, 3) reducing sediments along continental margins, and 4) oxic seafloor sediments. Below we discuss the evidence that these sources contribute significant amounts of Fe to the ocean, and evidence regarding the isotope 'fingerprint' of each source.

Atmospheric dust. The importance of dust as a source of Fe to the ocean has been recognized since Fe concentrations were first accurately measured in seawater. The importance of dust can be easily appreciated from the global distribution of iron concentrations. Relatively high Fe concentrations in the North Atlantic coincide with a significant input of atmospheric dust from the Saharan Desert, while iron concentrations are lower in regions with less dust input such as the HNLC Southern Ocean and Equatorial Pacific (Fung et al. 2000; Jickells et al. 2005; Mahowald et al. 2005; Moore et al. 2002). Similarly, Fe concentrations in the surface ocean vary seasonally in response to seasonal changes in dust deposition, and even on shorter timescales in response to individual dust deposition events (Boyle et al. 2005; Fitzsimmons et al. 2015; Sedwick et al. 2005). Dust was considered to be such a dominant source of iron to the marine realm that early models of the global iron cycle considered it as the only source of Fe to the global ocean (Moore et al. 2002; Parekh et al. 2004).

While the importance of dust as a source of bioavailable Fe to the surface ocean is unquestionable, there are great uncertainties in the size of the dust-Fe flux to the ocean. Estimates of the total amount of Fe deposited in the surface ocean vary by nearly an order of magnitude from 1×10^{11} to 6×10^{11} mol.y^{-1} (Fung et al. 2000). This uncertainty is compounded by the even larger uncertainties about how much of that dust Fe dissolves in seawater. Typical estimates for the solubility of mineral dust range from 1% to 10%, and solubility estimates for Fe from less common sources such as biomass burning range up to 100% (Fung et al. 2000; Jickells and Spokes 2001; Luo et al. 2008; Mahowald et al. 2005). With the uncertainties in total dust

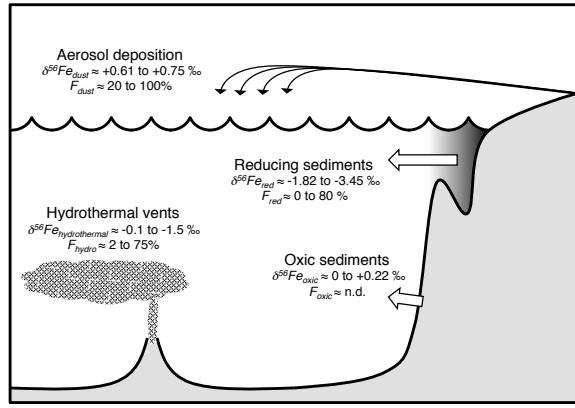

Figure 15. A pictoral representation of the major fluxes of Fe to the oceans including aerosol deposition to the surface ocean, hydrothermal vent input, and sources from both reducing and oxic sediments. The commonly observed range in δ^{56}Fe for each of these sources is taken from Conway and John (2014). Approximate ranges in the fraction of global surface-ocean Fe attributable to each of these sources is based on modeling studies, highlighting the large uncertainties in the relative magnitude of these various fluxes.

fluxes compounded by uncertainties in dust solubilities, there is very little constraint on the total amount of dissolved iron in the oceans that is delivered from dust. Of course in some cases it is clear dust is the source of dissolved Fe based on its distribution, for example when surface Fe maxima are observed away from other obvious Fe sources. But to better understand how much of the Fe is from dust in more ambiguous regions such as the global deep ocean, it may be useful to trace the isotopic signature of dust-derived Fe.

While the total δ^{56}Fe of most natural aerosols is similar to that of continental material, this may be different from the δ^{56}Fe of the Fe released from dust into seawater. The total δ^{56}Fe of most natural aerosols and loess samples falls within a small range near +0.1‰ (Beard et al. 2003; Majestic et al. 2009; Waeles et al. 2007). There is evidence, however, that industrial or anthropogenic aerosols may have a lighter δ^{56}Fe signature (Majestic et al. 2009). While the global importance of anthropogenic aerosols to the ocean is not well known, there is evidence that they can be transported far into the ocean. Fine size fraction aerosols from Bermuda have anomalously lower δ^{56}Fe values, generally between 0 and −0.5‰, during seasons when the aerosols are less influenced by Saharan dust and more influenced by North American sources, leading the authors to suggest that biomass burning may contribute isotopically light aerosol δ^{56}Fe (Mead et al. 2013). In addition to small variability in total dust δ^{56}Fe, there may be much larger fractionations between total dust δ^{56}Fe and soluble δ^{56}Fe. Leaching of Arizona Test Dust with an oxalate-EDTA solution meant to imitate the action of dissolved organic ligands in seawater resulted in the preferential release of slightly isotopically lighter Fe (roughly 0 to −0.5‰) (Revels et al. 2015).

However, neither the observed variability in aerosol δ^{56}Fe nor the observed fractionation of Fe isotopes during leaching with organic ligands can explain the observed δ^{56}Fe value of dust-influenced surface seawater in the North Atlantic. It was observed that surface ocean seawater dissolved δ^{56}Fe in the regions which showed the most obvious signs of dust Fe input (surface waters with high concentrations of Fe and low concentrations of other nutrients) were about +0.7‰, or roughly 0.6‰ heavier than expected total dust δ^{56}Fe (Conway and John 2014). While this observation appears robust at several locations across the North Atlantic, the reasons for this effect are unknown. Perhaps the dissolved seawater ligands are siderophores which bind iron with a very high affinity constant (Butler 2005; Reid et al. 1993), consistent with both theoretical and experimental evidence that stronger ligands preferentially bind heavier isotopes (Dideriksen et al. 2008).

While the evidence for a positive isotope effect during dust dissolution in the North Atlantic is strong, it is not yet known whether this is a universal 'fingerprint' which can be used to trace dust Fe throughout the global ocean. Future studies assessing the impact of dust deposition on seawater δ^{56}Fe in other locations, and a more complete understanding of the mechanisms that fractionate Fe during dust dissolution will help to answer these questions.

Hydrothermal input and plume dispersal. As with dust, there are large uncertainties about the amount of Fe delivered to the global ocean by hydrothermal vents. As hydrothermal fluids pass through the seafloor, they leach Fe from the surrounding rocks, yielding up to millimolar concentrations of Fe, many orders of magnitude higher than deep ocean seawater. If all of this Fe were to remain dissolved in seawater it would have an extraordinarily large impact on global ocean Fe concentrations. However, when hot and reducing hydrothermal fluids mix with the surrounding colder and more oxygenated seawater, nearly all of the hydrothermal iron is precipitated close to the hydrothermal vents as iron oxyhydroxide minerals (e.g., German and Von Damm 2003). While early studies suggested that iron was nearly quantitatively precipitated near hydrothermal vents, more recent work has suggested that a small portion of hydrothermal Fe may be stabilized within hydrothermal plumes through binding with dissolved and particular organic ligands (Bennett et al. 2008; Toner et al. 2009), and that this hydrothermal Fe may be transported great distances in the ocean. Ultimately, hydrothermal Fe is hypothesized to contribute significantly to global deep ocean Fe and surface ocean productivity.

The first evidence that hydrothermal vents might be a globally important source of Fe was based on the positive correlation between Fe concentrations and concentrations of excess ^{3}He in the North and South Pacific oceans (Boyle et al. 2005; Fitzsimmons et al. 2014), where excess ^{3}He is a tracer for deep sea hydrothermalism. These correlations were combined with global estimates of hydrothermalism to suggest that hydrothermal Fe contributes significantly to Fe concentrations and surface ocean productivity, particularly in the Southern Ocean which is far from other sources of Fe and where phytoplankton are known to be Fe-limited (Tagliabue et al. 2014, 2010). Modeling efforts are complemented by sampling efforts such as the GEOTRACES program, which have led to basin-scale sections of dissolved Fe concentrations across the world oceans. Elevated Fe concentrations in hydrothermal plumes have been found to extend hundreds, or thousands (in the case of the East Pacific rise) of kilometers from hydrothermal vents (Saito et al. 2013; Conway and John 2014; Resing et al. 2015). While such efforts have led to dramatic figures demonstrating the qualitative impact of hydrothermal vents on Fe concentrations, uncertainty remains about how quantitatively important vents are to the global ocean Fe inventory. Estimates of the hydrothermal Fe flux range from a few percent of the global dust flux up to 65%, with significant uncertainties derived from the roughly 2-orders of magnitude variability in Fe/^{3}He ratios measured at different vent sites (Tagliabue et al. 2010, 2014; Carazzo et al. 2013; Fitzsimmons et al. 2014; Saito et al. 2013).

While the δ^{56}Fe signature of most primary hydrothermal fluids falls within a narrow range, the δ^{56}Fe value of the Fe that eventually becomes stabilized within the hydrothermal plume is less well known. Primary hydrothermal fluid δ^{56}Fe is typically lighter than that of igneous rocks by about −0.2 to −0.3‰ (Beard et al. 2003; Rouxel et al. 2004, 2008b, 2016; Severmann et al. 2004; Sharma et al. 2001). Hydrothermal plume particulates enriched in Fe-oxyhydroxide have been found to be heavier than the original hydrothermal fluids (Severmann et al. 2004) while (buoyant) plume particulates dominated by Fe-sulfide minerals were isotopically lighter (Bennett et al. 2009; Rouxel et al. 2016). Those results led the authors to conclude that hydrothermal vents might be a source of either isotopically lighter or heavier Fe to the oceans depending on the end-member hydrothermal fluid composition (i.e., Fe/H_2S ratios) and geological setting.

In the North Atlantic ocean near the TAG (Trans-Atlantic Geotraverse) hydrothermal vent site, δ^{56}Fe has been measured in the hydrothermal plume but not in the immediate vicinity of hydrothermal venting (Conway and John 2014). These samples from within the neutrally buoyant hydrothermal plume provide the first look at how hydrothermal δ^{56}Fe might be expressed in the global ocean. Here, δ^{56}Fe value of dissolved iron within the plume ranges from −0.1 to −1.35‰. Because the −0.1‰ value represents mixing of hydrothermal Fe with ambient seawater, the data suggest that, at least for this particular TAG site, hydrothermal vents are a source of isotopically light Fe to the oceans.

Reducing sediments. The low solubility of Fe(III) in seawater is a major factor in defining the low Fe concentrations observed throughout the oxygenated oceans. Under certain conditions, however, Fe(III) may be reduced to Fe(II) which is very soluble in seawater. In the ocean, such reducing conditions typically occur at continental margins. Here, physical circulation brings nutrients into the upper ocean leading to high biological productivity in the surface, and a high flux of reduced organic carbon to the sediments. Within these sediments, particulate Fe(III) can be directly reduced by organisms which use it as an electron acceptor for metabolism of organic carbon, or it can be inorganically reduced by other reduced species in sediment porewater. Either way, the end result is sedimentary porewaters which contain extraordinarily high (μM to mM) concentrations of dissolved Fe(II). These porewaters may eventually diffuse into the overlying water column where Fe(II) may be reoxidized and precipitate back to the sediments, or where some portion of the Fe(II) may be stabilized and contribute to global ocean dissolved Fe.

As with other fluxes of Fe to the ocean, estimates vary considerably about the importance of reducing sediments to the global Fe pool. While early models of the global Fe cycle neglected sedimentary Fe inputs entirely, more recent models suggest that sediments may in fact be a dominant source of Fe to the oceans. A version of the BEC (Biogeochemical Elemental Cycling) model suggests that sediments contribute roughly half of the global ocean Fe, with the greatest impacts on productivity in Arctic regions (Moore and Braucher 2008). A study with the NEMO-PISCES (NEMO=Nucleus for European Modelling of the Ocean) model suggests an even greater impact of sediments, supplying roughly 80% of global Fe (Tagliabue et al. 2014). Scaling up observations from benthic landers to the global ocean would suggest that 98% of the Fe flux into the oceans is supported by reducing continental margin sediments (Elrod et al. 2004).

The δ^{56}Fe signature of reducing sediments is typically very isotopically light compared to other sources. The reason for this unique δ^{56}Fe signature is understood to be the isotopic equilibration of dissolved Fe(II), and Fe(III) either dissolved or attached to sediment particles. Both theoretical calculations and experimental observations suggest that Fe(II) is about −3‰ lighter than Fe(III) when the two species are at chemical equilibrium (Anbar et al. 2005; Johnson et al. 2002; Welch et al. 2003). Consequently, many studies of porewaters in reducing environments show porewater δ^{56}Fe values which are several permil lighter than bulk sediments (Bergquist and Boyle 2006; Severmann et al. 2006, 2010). This characteristically light signature has also been observed just above the sediment-water interface in benthic landers (Severmann et al. 2010), and in the water column tens to hundreds of meters above the bottom in the Santa Barbara and San Pedro basins and in the Peru upwelling region (John et al. 2012a; Chever et al. 2015). While Fe from reducing sediments is commonly isotopically light, there is significant variability in the exact δ^{56}Fe, with values almost always between roughly −3‰, which is the maximum fractionation expected between Fe(II) and Fe(III), and roughly 0‰ corresponding to a continental δ^{56}Fe value. Values of δ^{56}Fe higher than −3‰ could be due to closed-system isotope fractionation, where the first Fe(II) produced is roughly −3‰ lighter than the bulk particle δ^{56}Fe but continued dissolution of those particles drives the porewater δ^{56}Fe closer to the continental value (Chever et al. 2015). Alternatively, within sulfidic sediments the precipitation of isotopically light FeS has been shown to increase porewater δ^{56}Fe (Roy et al. 2012; Severmann et al. 2006; Sivan et al. 2011).

Non-reductive sediments. Oxic sediments have not traditionally been considered an important source of Fe to the oceans, though recent work has revived interest in this subject (Jeandel et al. 2011) and suggested that it may be a globally important source. The isotopic signature of Fe released from oxic sediments appears to be similar to that of continental material. In the first study which used seawater δ^{56}Fe as evidence for input of Fe from oxic sediments, it was suggested that the δ^{56}Fe signature of non-reductive sedimentary dissolution was about +0.3‰ (Radic et al. 2011). Subsequent studies have suggested that oxic sediments may have a δ^{56}Fe value close to that of continental material (Homoky et al. 2013).

Other sources. Most other sources of Fe to the oceans are not thought to contribute significantly to the global ocean Fe pool. However, point sources of Fe to the oceans may have a large impact on Fe concentrations and δ^{56}Fe locally. Such potentially important sources of Fe to the oceans include glaciers (Bhatia et al. 2013; Hawkings et al. 2014; Raiswell et al. 2006; Zhang et al. 2015), rivers (Escoube et al. 2009, 2015), and submarine groundwater discharge (Windom et al. 2006; Rouxel et al. 2008a; Roy et al. 2012).

The potential importance of coastal groundwater discharge in producing both highly negative and positive δ^{56}Fe values in local seawater has been hypothesized by Roy et al. (2012) and Rouxel et al. (2008a). The δ^{56}Fe value of groundwater discharge ultimately depends on mixing processes within subterranean estuaries. In Waquoit Bay (Massachussetts, USA), the groundwater source has high Fe(II) concentrations and δ^{56}Fe values between 0.3 and −1.3‰ (Rouxel et al. 2008a). Within the coastal sandy sediments, pore waters from the mixing zone

of the subterranean estuary have even lower $\delta^{56}Fe$ values down to −5‰ as a result of partial Fe(II) oxidation and precipitation of isotopically heavy Fe-oxhydroxides. Hence, the input of groundwater Fe-sources at Waquoit Bay is the most likely explanation for both negative $\delta^{56}Fe$ values and high Fe-concentrations observed in surface seawater (Rouxel and Auro 2010).

In contrast to Waquoit Bay, the Indian River Lagoon subterranean estuary (Florida, USA) is characterized by organic-rich sediments leading to SO_4^{2-} reduction and S_2-rich porewaters (Roy et al. 2010). In this system, Fe-oxide reduction produces dissolved Fe(II) below the zone of Fe-sulfide precipitation and this dissolved Fe(II) flows upward. The total range of Fe isotope fractionations, of about 2.5‰, results from in situ diagenetic reactions in the subterranean estuary. The near-surface Fe-sulfide precipitation ultimately delivers dissolved Fe with slightly positive $\delta^{56}Fe$ values, averaging about +0.24‰, via submarine groundwater discharge (SGD). Consequently, we suggest that Fe-sulfide precipitation in subterranean estuaries could be a previously unidentified source of isotopically heavy Fe to the coastal waters

Using Fe isotopes to trace sources of Fe in the oceans

A key motivation for efforts to analyze the $\delta^{56}Fe$ value of various marine Fe sources is to constrain the relative contributions of various different sources of Fe to the oceans. With orders of magnitude uncertainty in the flux of Fe from various sources to the ocean based on other methods, $\delta^{56}Fe$ provides a valuable tool for tracing these sources as they mix into the global ocean. Given certain assumptions, the $\delta^{56}Fe$ value of seawater can be used to quantify the amount of Fe coming from various sources. The general isotope mass balance equation:

$$\delta^{56}Fe_{total} = \delta^{56}Fe_A \Delta f_A + \delta^{56}Fe_B \Delta f_B$$

can be applied in the ocean to calculate the relative fraction of Fe from different sources where $\delta^{56}Fe_{total}$ is the measured $\delta^{56}Fe$ of seawater, and $\delta^{56}Fe_{A/B}$ and $f_{A/B}$ are the end-member isotopic composition and fraction of Fe in the seawater coming from source A or B. This technique has been widely applied to quantify the amount of Fe coming from different sources in many locations in the global ocean (Conway and John 2014; John and Adkins 2012; Lacan et al. 2008; Radic et al. 2011; Revels et al. 2014).

The weaknesses of this approach should be carefully considered. The calculated fraction of Fe coming from different sources depends on the choice of end-member $\delta^{56}Fe$ values, and studies have shown significant variability in the source $\delta^{56}Fe$ value from different locations. Also, such equations are only valid when assuming that only two sources of Fe are mixing at any individual location. Incorporating Fe stable isotopes into global models of the Fe cycle, combined with new datasets on the global distribution of $\delta^{56}Fe$ from GEOTRACES and other sampling efforts, presents an opportunity to combine the strengths of $\delta^{56}Fe$ as a tracer for Fe sources with the more complex formulations of mixing and circulation possible in global 3D models. Finally, the application of $\delta^{56}Fe$ to trace various Fe sources in the ocean relies on the assumption that $\delta^{56}Fe$ is not modified by chemical reaction as it travels away from the source.

Internal cycling of Fe isotopes within the ocean

While the assumption that $\delta^{56}Fe$ can be used as a passive tracer for mixing of Fe from different sources in the deep ocean, away from regions of biological productivity and strong gradients in chemistry, there are other locations where seawater $\delta^{56}Fe$ has been shown to be modified by chemical reaction.

Biological uptake of Fe appears to preferentially remove the heavier isotopes from seawater. In the North Atlantic, this is inferred from the fact that a minimum in $\delta^{56}Fe$ is observed in the upper-ocean, coincident with the Fe concentration minimum and the chlorophyll maximum (Conway and John 2014). In the Southern Ocean, the biological uptake of heavier Fe isotopes is observed as a decrease in $\delta^{56}Fe$ over the course of the spring phytoplankton bloom (Ellwood

et al. 2015). So-called 'inverse' isotope effects, where heavier isotopes react more quickly or are preferentially assimilated during biological processes, are very rare. Most known reactions of C, N, and O isotopes result in the preferential biological assimilation of lighter isotopes, as does the assimilation of Zn and Cd by phytoplankton (John and Conway 2013; John et al. 2007; Lacan et al. 2006). In contrast to these other nutrients, culture data on Fe isotope fractionation by phytoplankton are scarce (John et al. 2012b), limiting our ability to form a mechanistic explanation for the isotope fractionations observed in nature.

The fractionation of Fe isotopes has also been observed during Fe precipitation, though the magnitude and sign of this isotope effect changes under different conditions. Hydrothermal particles have been found to be heavier, lighter, and similar to the dissolved phase in various locations (Bennett et al. 2009; Conway and John 2014; Revels et al. 2014; Severmann et al. 2004; Rouxel et al. 2016). Altogether, these studies suggest that both the initial Fe isotope composition of the high-temperature vent fluids and its initial Fe/H_2S ratio (i.e., isotopically light Fe sulfide precipitation versus isotopically heavy Fe-oxyhydroxide precipitation) should impose characteristic Fe isotope "fingerprints" for hydrothermally derived Fe in the deep ocean.

Particles precipitating near reducing continental margins have been found to be similar to or heavier than the dissolved phase (Chever et al. 2015), while the weakly bound 'ligand leachable' phase within particles is generally isotopically lighter than seawater (Revels et al. 2014).

THE GEOLOGICAL RECORD AND PALEOCEANOGRAPHIC APPLICATIONS

The ferromanganese crust record

Since Fe is actively involved in key biogeochemical processes and has a variety of potential sources to the oceans (e.g., atmospheric deposition, sediment input, rivers, hydrothermal vents) (Hutchins et al. 1999; Johnson et al. 1999; Chase et al. 2005), the record of Fe isotopes in Fe–Mn deposits has attracted significant interest (Zhu et al. 2000; Beard et al. 2003b; Levasseur et al. 2004; Chu et al. 2006; Horner et al. 2015; Marcus et al. 2015). Ferromanganese (Fe–Mn) crusts and nodules have long been characterized for their elevated concentrations of transition metals (e.g., Ni Co, and Cu) and their very slow growth rates (1–6 mm/Myr). Long-lived radiogenic isotope (e.g., Os, Pb, Nd, Hf, Be) and more recently non-traditional stable isotope (e.g., Tl, Mo, Cd, Ni) compositions of hydrogenous Fe–Mn deposits have been used to reconstruct the connection between plate tectonics, climate change, weathering processes and (1) metal sources, (2) carbon and metal cycles, and (3) mixing of water masses in the ocean through the Cenozoic (Frank 2002; Siebert et al. 2003; Horner et al. 2010; Nielsen et al. 2011; Gall et al. 2013)

Modern marine sediments, such as deep-sea clays, terrigenous sediments, turbidite clays, and volcanoclastites, have a restricted range of $\delta^{56}Fe$ values clustered around average crust (Beard et al. 2003b; Rouxel et al. 2003; Homoky et al. 2013), suggesting minor Fe isotope fractionation during continental weathering and particle transport in seawater (Radic et al. 2011). In contrast, marine sediments in which the Fe budget is controlled by authigenic or diagenetic precipitates are characterized by a range of $\delta^{56}Fe$ values generally enriched in light Fe isotopes (Severmann et al. 2006; Homoky et al. 2013). This is particularly true for hydrogenous (i.e., seawater-derived) precipitates, including Fe–Mn crusts and nodules whose $\delta^{56}Fe$ values vary widely from −0.05 to −1.13‰, averaging -0.41 ± 0.49 (2SD, $n = 41$) in modern oceans (Fig. 16). Beard et al. (2003b) initially suggested that $\delta^{56}Fe$ variations in Fe–Mn deposits are controlled by the relative flux of Fe from aerosols (with $\delta^{56}Fe \sim 0$‰) and Fe from mid-oceanic ridge hydrothermal fluids (with $\delta^{56}Fe$ ranging from −0.5 to −1‰). This model assumes no Fe isotope fractionation during crust growth nor modification of the primary Fe isotope signature, which is unlikely considering the variety of Fe isotope

fractionation processes in hydrothermal plumes (Severmann et al. 2004; Bennett et al. 2009). Levasseur et al. (2004) reported the global variations of δ^{56}Fe of the surface scrapings of hydrogenetic Fe–Mn crusts (i.e., near modern values), and found no significant basin to basin trends or relationships with expected hydrothermal contributions (Fig. 16). Hence, although hydrothermal Fe may contribute significantly to some Fe–Mn crusts in the west Pacific (Chu et al. 2006), other marine sources characterized by light δ^{56}Fe values, such as dissolved Fe derived from shelf sediments (Severmann et al. 2006; Homoky et al. 2009; Conway and John 2014; Chever et al. 2015) may also contribute to these paleoceanographic records.

More recently, Horner et al. (2015) reported a range of δ^{56}Fe values from −1.12‰ to +1.54‰ along a 76 Ma-old Fe–Mn crust from the central Pacific (crust CD29–2). This range encompasses the range of δ^{56}Fe values measured for dissolved and particulate Fe from open seawater and oxygen minium zones—OMZs (Radic et al. 2011; John et al. 2012; Conway and John 2014; Chever et al. 2015). By considering a fractionation factor during crust uptake of Δ^{56}Fe–FeMn–SW = −0.77 ± 0.06‰, Horner et al. (2015) proposed that heavy δ^{56}Fe values of seawater (up to 2.2‰) may result from the modification of hydrothermally sourced Fe by precipitation of isotopically light Fe sulfides. Marcus et al. (2015) also investigated the Fe isotopic compositions over 1–3 mm increments across a nodule from the South Pacific Gyre. The δ^{56}Fe values showed limited range from −0.16 to −0.07‰ (Fig. 16), suggesting constant Fe isotope values over a period of 4 Ma despite the diversity of Fe mineral phases identified in the nodule layers (e.g., feroxyhite, goethite, lepidocrocite, and poorly ordered ferrihydrite-like phases). Hence, the results indicate that mineral alteration (i.e., recrystallization) did not affect the primary Fe isotopic composition of the nodule.

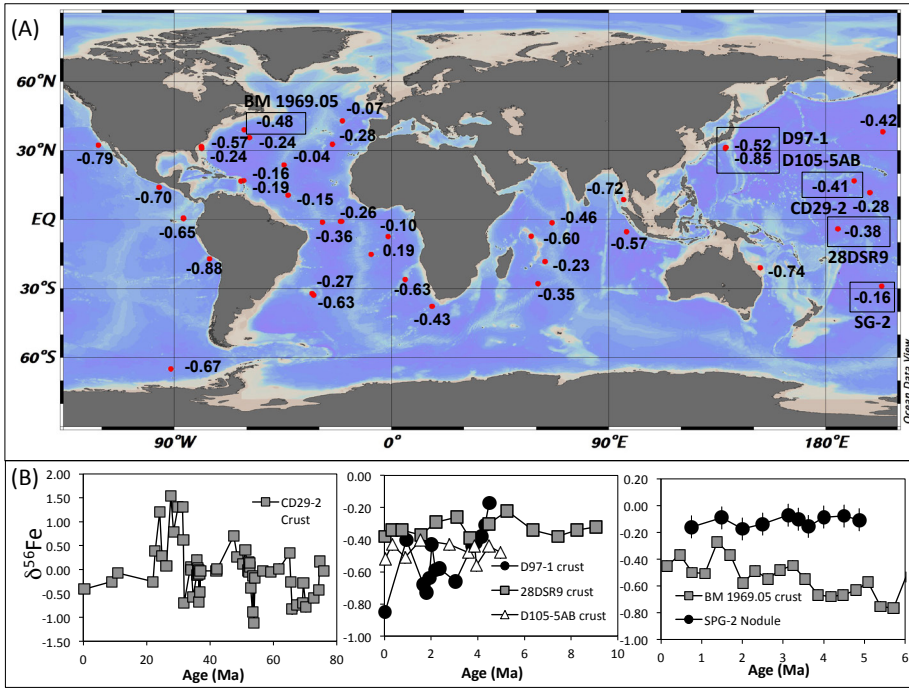

Figure 16. (A) Map of ferromanganese (FeMn) crust sample locations and δ^{56}Fe values of surface scrapings from each crust and (B) temporal δ^{56}Fe record from selected Fe–Mn crusts and nodules (location highlighted as framed number in panel A. Data from Zhu et al. (2000), Levasseur et al. (2004), Chu et al. (2006), Marcus et al. (2015).

Oceanic Anoxic Events

Extensive work in the Black Sea, the world's largest modern euxinic basin, reveals that additional reactive Fe, derived from benthic fluxes out of oxic-suboxic sediments in the shallow margin, is deposited as pyrite in the deep basin sediments (Raiswell and Canfield 1998; Wijsman et al. 2001; Anderson and Raiswell 2004; Lyons and Severmann 2006). Hence, sulfidic sediments often show pronounced enrichments in reactive Fe relative to oxic shelf sediments, leading to an increase in Fe/Al ratios and significant Fe isotope variability. Sediments from the oxic shelf of the Black Sea have bulk δ^{56}Fe values averaging +0.16 ± 0.02‰ that are slightly elevated relative to values for the average crust, whereas sulfidic sediments from the deep basin have lower values (mean δ^{56}Fe = –0.13 ± 0.04‰) (Severmann et al. 2008). The source of isotopically light Fe in bulk sediment is likely related to a shelf to basin Fe shuttle, whereby reactive Fe is sequestered nearly quantitatively during Fe sulfide precipitation in the euxinic water column (Severmann et al. 2008). This model is well supported by the fact that diagenetic fluids in anoxic and suboxic marine sediments have isotopically light Fe(II) (down to –2‰) (Severmann et al. 2006; Homoky et al. 2009). In contrast, Fe isotope data for a sediment core transect across the Peru upwelling area, which hosts one of the ocean's most pronounced OMZs (Scholz et al. 2014), show that the heaviest δ^{56}Fe values of the surface sediments coincide with the greatest Fe enrichment. The observed trend is the opposite of expected results (i.e., transfer of isotopically light Fe to the sediments below the OMZ) but could be explained by partial Fe(II) oxidation in the water column and precipitation of isotopically heavy Fe-oxyhydroxides (Chever et al. 2015).

Iron isotopic compositions of Phanerozoic organic-rich sediments studied so far display a range of δ^{56}Fe values consistent with the Black Sea model (Fig. 17). Jenkyns et al. (2007) examined the Fe isotopic compositions of shales formed during the Cenomanian–Turonian oceanic anoxic event (OAE). Black shales deposited before the onset of the OAE had light δ^{56}Fe values (−1.08 ± 0.28‰), unlike those found in the black shale deposited during the oceanic anoxic

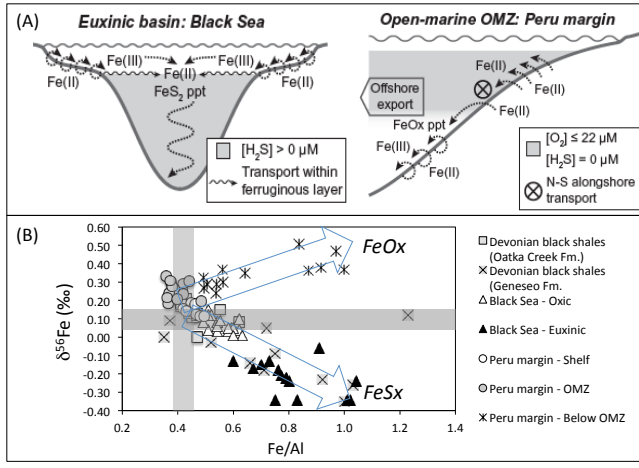

Figure 17. Cross plot of Fe/Al (in g/g) vs. δ^{56}Fe (B) of Devonian black shales (data from Duan et al. 2010) and sediment cores from the Black Sea (data from Severmann et al. 2008); the Peru margin (data from Scholz et al. 2014). The gray shaded areas correspond to Fe/Al and δ^{56}Fe of the lithogenic components while the two arrows illustrates the addition of authigenic Fe as Fe-sulfides and Fe-oxyhyroxide respectively showing the Fe isotope fingerprint for the Fe shuttle. The sketches at the top (A) are from Scholz et al. (2014) and illustrate mechanistic differences between Fe shuttles in euxinic basins and open-marine OMZs (FeS_2 ppt = pyrite precipitation; FeO_x ppt = Fe (oxyhydr)oxide precipitation). The gray shaded areas (see legend) refer to the redox state of the water column and do not provide information about the redox state of the sediments.

event itself (–0.07 ± 0.27‰). By comparison, Upper Jurassic pyrite- and siderite-bearing organic carbon-rich shales of the Kimmeridge Clay Formation (UK) yielded $\delta^{56}Fe = 0.08 \pm 0.13$‰ (Matthews et al. 2004). Duan et al. (2010) measured Fe isotopic compositions of bulk samples and chemically extracted pyrite in two black shale units deposited during the mid-to-late Devonian. Samples yielded light and variable bulk $\delta^{56}Fe$ values ranging from –0.53 to –0.06‰ and inversely correlated with Fe/Al. From these studies, it appears that the enrichment of isotopically light Fe in marine sediments can be used as diagnostic of enrichment mechanism (e.g., shelf to basin shuttle) in the geological record at times of widespread oxygen deficiency in the ocean.

The Precambrian record

A host of available geochemical and geological indicators demonstrate that the transition from an atmosphere with almost no oxygen to a fully oxygenated one—called the Great Oxidation Event (GOE)—occurred between 2.45 and 2.22 Ga (Holland 1984; see Lyons et al. 2014 for a recent review). It is now recognized that the rise of O_2 by ~2.3 Ga has been directly linked to an increase in the ocean's sulfate content and variable concentrations of redox-sensitive elements due to the combined effect of oxidative continental weathering and efficient trapping due to the development of local sulfidic environments (Canfield 1998; Scott et al. 2008; Poulton et al. 2010). Despite the recent progress, our understanding of ancient Fe biogeochemical cycling is still limited—if not biased—by the available rock archive and our ability to establish robust paleooceanographic proxies from rock compositions. The Banded Iron Formation (BIF) rock record, spanning every continent and encompassing sediments from as young as 0.55 Ga to as far back as Earth's earliest known marine deposit (~3.8 Ga BIF in Greenland) has been extensively used in the recent years. An alternative approach, which provides better temporal resolution than the BIF record, has also involved black shales. Considering that Fe sources (e.g., continental vs. hydrothermal) as well as Fe redox cycling mechanisms (biotic vs. abiotic) in Precambrian oceans remain controversial, the iron isotope geochemistry of Precambrian sedimentary rocks remains an active field of study, as presented in the following sections.

The archive of iron formations

The key to understanding the origin of Iron Formations (IFs) is to identify the mechanism that could have caused the oxidation of ferrous iron in an ocean that was globally anoxic (see the review by Bekker et al. 2010). There are three mechanisms that are generally considered: (i) oxygenic photosynthesis, releasing O_2 which could have then oxidized Fe(II) into Fe(III); (ii) anoxygenic photosynthesis, involving organisms using Fe(II) as an electron donor; (iii) UV photo-oxidation, promoted by an atmosphere devoid of ozone. The first two processes require the involvement of life, while photo-oxidation is a purely abiotic process. Recently, experiments have been performed to characterize the isotopic fractionation of Fe during photo-oxidation (Nie and Dauphas 2015; Nie et al. 2016). Those studies showed that Fe(II) photo-oxidation follows a Rayleigh fractionation model, with Fe isotope fractionation between Fe(III) precipitates and aqueous Fe(II) of about +1.2‰ at 45 °C. This fractionation is similar to that of anoxygenic photosynthetic oxidation and of O_2-mediated oxidation (Bullen et al. 2001; Welch et al. 2003; Croal et al. 2004; Balci et al. 2006; Beard et al. 2010a; Swanner et al. 2015), which therefore cannot be used to rule out possible pathways to BIF formation.

There have been a number of Fe isotope studies of IF, including Fe-oxide and carbonate facies IF, with the end goal of tracking the biogeochemical cycling of Fe on the early Earth (Beard et al. 1999; Johnson et al. 2003, 2008a,b; Dauphas et al. 2004b; Planavsky et al. 2009, 2012; Steinhoefel et al. 2009b; Heimann et al. 2010; Craddock and Dauphas 2011b; Li et al. 2015). Bulk samples of IF show a large range of $\delta^{56}Fe$ values (Fig. 18) which provide insights into Fe enrichment mechanisms and Fe sources. The two most commonly proposed iron sources, hydrothermal and benthic/diagenetic, have both negative (sub-crustal) $\delta^{56}Fe$ values (Rouxel et al. 2008b; Severmann et al. 2008; Homoky et al. 2013; Chever et al. 2015). Hence, the presence

of heavy δ^{56}Fe values in oxide-facies IF must reflect the fractionation during partial Fe(II) oxidation and Fe(III) mineral precipitation. This enrichment in heavy Fe isotopes contrasts with the isotope fractionations associated with Fe(II)-bearing siderite, ankerite, and green rust precipitation, which are depleted in the heavy Fe isotopes relative to the ambient $Fe(II)_{aq}$ pool (Wiesli et al. 2004). Although Fe silicates have been recently proposed to form the primary sediments (i.e., precursor) of Banded Iron Formations (BIFs), before being silicified upon deposition and diagenesis (Rasmussen et al. 2013, 2015), the exact fractionation factor during precipitation of Fe silicates in anoxic seawater is currently not known. Therefore, positive Fe isotope values in IF indicate that Fe(III) delivery was the main process driving the deposition of IF. Additionally, the expression of the Fe isotope fractionation implies partial Fe(II) oxidation, pointing towards oxidation at low Eh conditions (Dauphas et al. 2004b; Planavsky et al. 2009, 2012). If oxidation took place during mixing of anoxic Fe-rich and fully oxic marine waters, as was commonly envisaged in the past (Cloud 1973), oxidation would have been essentially quantitative given the rapid oxidation kinetics of iron at neutral to alkaline pH. This rapid and quantitative oxidation would have prevented any significant expression of iron isotope fractionations as is the case with modern hydrothermal plume fall-outs (Severmann et al. 2004).

A compilation of bulk-rock and mineral-specific δ^{56}Fe values for Archean and Paleo-proterozoic IFs (Fig. 18) reveals heavier δ^{56}Fe values in Archean and early Paleo-proterozoic IF, in contrast to later Proterozoic and Phanerozoic Fe oxide-rich rocks. Notably, the lowest δ^{56}Fe values are typical for the ca. 2.22 Ga Hotazel Formation of South Africa and especially for manganese-rich samples (Planavsky et al. 2012; Tsikos et al. 2010). This unique feature may reflect deposition of iron and manganese from hydrothermal fluids depleted in heavy Fe isotopes by progressive Fe oxidation and precipitation in the deeper part of the redox-stratified basin that was at a redox state intermediate between that required for iron and manganese oxidation (Tsikos et al. 2010). In general, BIF-hosted siderite has negative δ^{56}Fe values, which is expected given the isotopic fractionation during siderite precipitation and expected Fe isotope values for seawater. Therefore, the rare case of siderite with positive δ^{56}Fe values must have been derived from reductive dissolution of iron oxides rather than having precipitated directly from seawater. In most cases, microbial iron reduction can be assumed to be driving the reductive oxide dissolution. This also implies that the IF carbonates do not reflect seawater compositions, but instead record extensive diagenetic Fe cycling in the soft sediment prior to lithification (Heimann et al. 2010; Craddock and Dauphas 2011b; Johnson et al. 2013). A dichotomy exists among BIF associated carbonates (i.e., within nominal BIF units or stratigraphically close to BIF units) between those that are iron-rich (siderite, ankerite), have low δ^{13}C values, and high δ^{56}Fe values, and those that are iron-poor (calcite, dolomite), have normal δ^{13}C values, and low δ^{56}Fe values (Heimann et al. 2010; Craddock and Dauphas 2011b) (Fig. 19). The isotopic and chemical signatures of the second group of carbonates are consistent with precipitation from seawater. The first group of carbonates, however, is best explained by cycling of organic carbon and hydrous ferric iron oxide during diagenesis, possibly mediated by biological activity (DIR). Iron isotopes may point towards microbial iron reduction in the rock record, possibly dating back to the earliest sedimentary rocks at ca. 3.8 Ga (Craddock and Dauphas 2011b). An alternative is that the iron-rich carbonates formed entirely abiotically by reaction between ferric iron precipitate and organic carbon during metamorphism (Perry et al. 1973; Köhler et al. 2013; Halama et al. 2016).

Li et al. (2015) reported an extensive dataset of high-precision *in situ* Fe isotope variations in BIF from the Dales Gorge member (core DDH-47A). Fe isotope analysis performed along and across a magnetite microband showed limited variability at the grain scale, with δ^{56}Fe clustering at -0.49 ± 0.22‰ (2SD, $n = 136$). The homogeneity of Fe isotopic composition at centimeter scale argues either for constancy in supply and iron isotopic fractionation

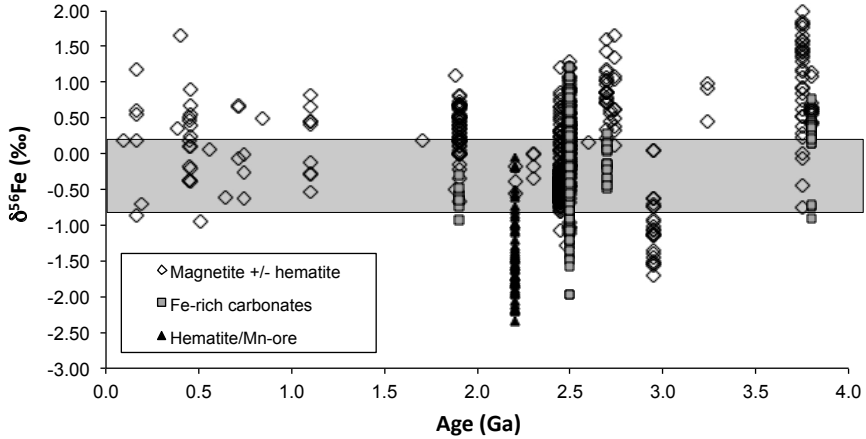

Figure 18. Secular variations in δ^{56}Fe values for Archean and Paleoproterozoic iron formations and younger sediments for comparison. Data include mineral separate analyses (magnetite, hematite, Fe-rich carbonates: ankerite and siderite, pyrite, and metamorphic Fe-silicates) and *in situ* analysis (magnetite) using laser-ablation MC-ICPMS and ion-microprobe. The gray area is bounded by the average δ^{56}Fe values for igneous rocks and δ^{56}Fe values for hydrothermal sources (Beard et al. 2003b; Rouxel et al. 2008a). A total of 663 datapoints is shown including: (a) 83 datapoints for the ca. 1.88 Ga GIF from the Animikie basin, North America (Frost et al. 2007; Hyslop et al. 2008; Planavsky et al. 2009); (b) 138 datapoints for the ca. 2.5 Ga Brockman Iron Formation, Western Australia (Johnson et al. 2008b); (c) 154 datapoints for the 2.5 Ga Kuruman IF and Gomahaan Fm., Transvaal supergroup, South Africa (Johnson et al. 2003; Heimann et al. 2010); (d) 27 datapoints for the Shurugwi and Belingwe greenstone belt IF, Zimbabwe (Rouxel et al. 2005; Steinhoefel et al. 2009a); (e) 137 datapoints for the Eoarchean Isua, Akilia, and Innersuartuut IF and metamorphic rocks (Dauphas et al. 2004a, 2007a,b; Whitehouse and Fedo 2007b); (f) 12 datapoints for the Neoproterozoic Rapitan IF (Halverson et al. 2011); (g) 52 datapoints for IF and Mn formation from the Paleoproterozoic Hotazel Formation, Transvaal Supergroup, South Africa (Tsikos et al. 2010); (h) 45 datapoints for other Paleoproterozoic and Archean IF (Planavsky et al. 2012); (i) 263 datapoints for the Dales Gorge member of the ca. 2.5 Ga Brockman IF (Hamersley Basin, Western Australia) (Craddock and Dauphas 2011; Li et al. 2015) (j) 42 datapoints for the Joffre Member of the Brockman Iron Formation (Hamersley Basin, Western Australia) (Haugaard et al. 2016); (k) 20 datapoints for 2.95 Ga Sinqeni Formation, Pongola (Planavsky et al. 2014); (l) 8 datapoints for the Ordovician Jasper beds from the Lokken ophiolite complex (Norway, Moeller et al. 2014) and additional data from Phanerozoic jasper (Planavsky et al. 2012).

for ~1000 yr or significant homogenization during early BIF diagenesis, consistent with the lines of evidence showing that magnetite and quartz are not primary minerals (Bekker et al. 2012; Rasmussen et al. 2015). Using coupled Fe and Nd isotope systems, Li et al. (2015) also evaluated potential variations in Fe sources during BIF deposition. The results suggested mixing of seawater masses with distinct Fe- and Nd-isotopic compositions: one is continentally sourced and has near-zero to negative δ^{56}Fe values, whereas the other is mantle/hydrothermally sourced and has slightly to strongly positive δ^{56}Fe values. The origin of the isotopically light Fe source in Archean seawater, however, remains a matter of controversy. On the one hand, negative δ^{56}Fe values in BIFs have been explained by the progressive oxidation of hydrothermal fluids following a Rayleigh fractionation-type model (Rouxel et al. 2005; von Blanckenburg et al. 2008; Steinhoefel et al. 2009b; Tsikos et al. 2010; Planavsky et al. 2012; Busigny et al. 2014). In this scenario, anoxygenic phototrophic oxidation could have established significant water column Fe concentration gradients—and therefore Fe isotope gradients—through ferric Fe removal during upwelling. On the other hand, the source of light Fe in IF could result from the near-quantitative oxidation of Fe(II) produced through dissimilatory Fe reduction (DIR) (Severmann et al. 2008; Heimann et al. 2010; Li et al. 2015). In fact, both models may be reconciled considering an Fe-rich deep ocean globally affected by strong hydrothermal input, and shallow water masses dominated by continentally derived Nd and isotopically light

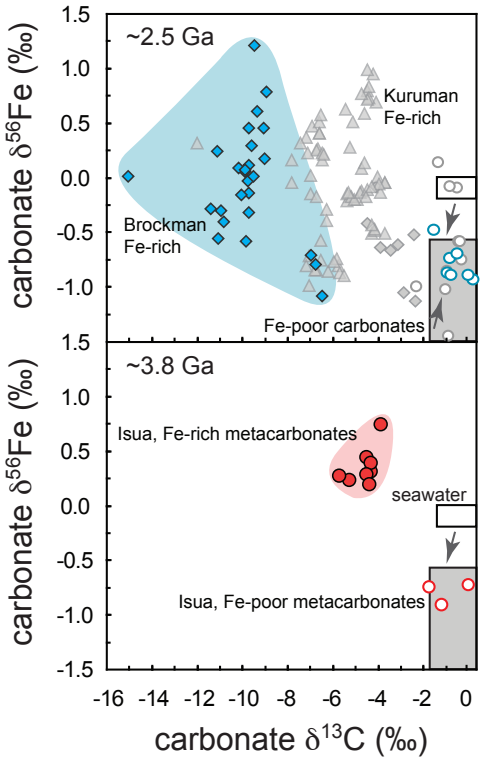

Figure 19. Iron and carbon isotopic compositions of carbonates associated with iron formations (Craddock and Dauphas 2011b and references therein). Iron-poor carbonates have low δ^{56}Fe values and high δ^{13}C values consistent with precipitation from seawater. Iron-rich carbonates have high δ^{56}Fe values and low δ^{13}C values consistent with cycling during diagenesis between low-δ^{13}C organic matter and high-δ^{56}Fe ferric iron oxide precipitate. Such cycling may have been mediated by bacterial dissimilatory iron reduction.

Fe (and Fe-depleted) due to efficient oxidation of hydrothermally affected Fe in the photic zone. This model is consistent with the generally accepted genetic models for Archean and Paleoproterozoic IF (Bau and Dulski 1996; Sumner 1997; Bekker et al. 2012).

The average Fe isotopic composition of different types of IFs remains a major unresolved question. In some cases IF have been estimated to have near crustal average δ^{56}Fe values (Johnson et al. 2008b) or slightly heavier (Planavsky et al. 2012). Recently, Haugaard et al. (2016) conducted detailed petrologic and geochemical analyses of a core section drilled through the entire 355 m of stratigraphic depth of the ca. 2.45 Ga Joffre Member from the Brockman Iron Formation. As a whole, δ^{56}Fe ranges from –0.74 to +1.21‰ with no obvious relationships with either lithology or stratigraphic levels. Although the average δ^{56}Fe value of +0.11‰ for the entire section is close to crustal values defined at +0.09‰, this value may still be affected by sampling bias considering the large variability and still limited sample size (i.e., 42 samples for about 350 m of stratigraphic unit). Furthermore, the Joffre Member was likely deposited in a restricted basin and Algoma-type iron formations are more likely to have positive δ^{56}Fe values (Planavsky et al. 2012). More work is needed to better understand the Fe isotope mass-balance of BIFs and in particular to test whether deposition of isotopically heavy IFs in the deeper parts of the basins could create pools of isotopically light dissolved iron that were buried in shallow-water environments in the Archean.

Black Shales and Sedimentary Pyrite Archives

Trace-metal concentrations of laminated, organic-rich shale facies have long been used to draw inferences concerning paleoredox conditions as well as metal inventory in ancient oceans (Algeo et al. 2004; Brumsack 2006; Lyons and Severmann 2006; Lehmann et al. 2007; Scott et al. 2008) with potential constraints on past atmospheric oxygenation, weathering intensity, marine productivity, global volcanic and hydrothermal events and ocean redox structure. Past studies of non-mass dependent and mass dependent sulfur isotope records of sedimentary pyrite have placed important constraints on the biogeochemical cycle of sulfur and the evolution of ocean chemistry during the rise in atmospheric oxygen (Cameron 1982; Farquhar et al. 2000, 2007; Mojzsis et al. 2003; Ono et al. 2003; Bekker et al. 2004; Johnston et al. 2006). Rouxel et al. (2005) applied a similar time-record approach to explore potential changes in Fe isotope values of sedimentary pyrite in black shale. They identified a direct link between the rise in atmospheric oxygen and changes in the Fe ocean cycle that provides new insights into past ocean redox states.

The general pattern of this record divides Earth's history into three stages (Fig. 20) which are strikingly similar to the stages defined by the $\delta^{34}S$ and $\Delta^{33}S$ records as well as other indicators of the redox state of the atmosphere and ocean (Holland 1984; Bau and Moller 1993; Karhu and Holland 1996; Farquhar et al. 2000; Bekker et al. 2004, 2005). The first stage in >2.3 Ga black shales corresponds to highly variable (from approximately −3.5 to +0.5‰) and overall negative $\delta^{56}Fe$ values in diagenetic pyrite. The second stage between 2.3 and 1.8 Ga shows more subdued variations in $\delta^{56}Fe$ values that extend from ~−0.5 to +1‰. The last stage after 1.8 Ga shows limited variations in $\delta^{56}Fe$ values and an average that is near zero or slightly negative. Although several interpretations of this Fe isotope record were proposed in subsequent studies (Archer and Vance 2006; Rouxel et al. 2006; Severmann et al. 2008; Guilbaud et al. 2011b, 2012), there is a general consensus that the shift from high $\delta^{56}Fe$ variability in >2.3 Ga black shales to little variability <1.8 Ga reflects redox-related changes in the global oceanic Fe cycle. The variable and light $\delta^{56}Fe$ values in pyrites older than about 2.3 Ga suggest that an iron-rich global ocean was strongly affected by the deposition of Fe oxides in a globally anoxic and Fe-rich ocean. The Fe oxide pool provides a means to generate isotopically light dissolved Fe through (1) reservoir effects during partial Fe(II) oxidation, and (2) dissimilatory Fe reduction. Between 2.3 and 1.8 Ga, positive Fe isotope values of pyrite up to +1‰ likely reflect an increase in the precipitation of

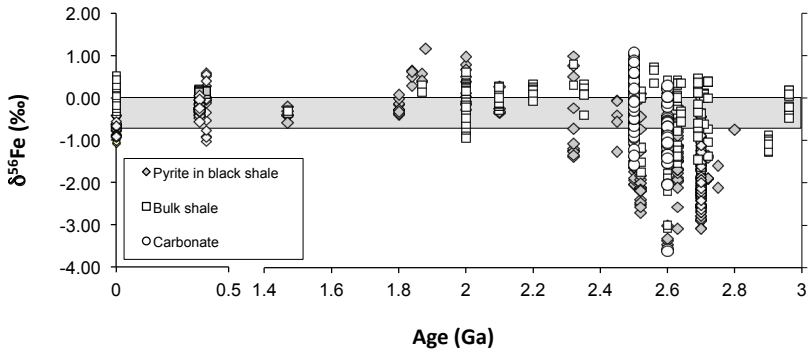

Figure 20. Secular trend of $\delta^{56}Fe$ values of pyrite from black shales (data from Rouxel et al. 2005; Duan et al. 2010 and Rouxel, unpublished), and bulk samples of organic-rich shales (data from Rouxel et al. 2005; Yamaguchi et al. 2005; Archer and Vance 2006; Czaja et al. 2010; Duan et al. 2010) and carbonate (data from Czaja et al. 2010; Heimann et al. 2010). Organic matter-rich sediments from the Black Sea and Peru Margin (Severmann et al. 2008; Scholz et al. 2014) are shown for comparison. *In situ* $\delta^{56}Fe$ values of pyrite, ranging from ca. −4 to +4‰ (Yoshiya et al. 2012; Tahata et al. 2015) are not displayed. The gray area is bounded by the average $\delta^{56}Fe$ values for igneous rocks and $\delta^{56}Fe$ values for hydrothermal sources (Beard et al. 2003b; Rouxel et al. 2008a).

isotopically light Fe sulfides relative to Fe oxides in a redox stratified ocean (Rouxel et al. 2005). Regardless of the exact process leading to Fe isotope variations in sedimentary pyrite, it apprears that Fe isotopes are particularly sensitive to the concentration of dissolved Fe(II) and H_2S (i.e., the size of seawater Fe and sulfate reservoir) and can be used to place important constraints on the sources to and sinks from this Fe(II) reservoir in past oceans.

In order to better assess intra-grain δ^{56}Fe variability, several studies applied *in situ* techniques such as laser ablation coupled to MC-ICPMS (Nishizawa et al. 2010b; Yoshiya et al. 2012; Tahata et al. 2015) or ion microprobe (Marin-Carbonne et al. 2014). Nishizawa et al. (2010) performed *in situ* Fe isotope analyses of pyrite within 2.7 Ga shallow marine carbonates from the Fortescue Group, and showed that the δ^{56}Fe values range from −3.0 to +2.2‰ with a bimodal distribution pattern. Pyrites from the upper Mingah Member of the Fortescue Group showed the widest variation of δ^{56}Fe values from −4.18 to +2.10‰ (Yoshiya et al. 2012). The extremely light δ^{56}Fe values are best explained by the combination of Fe isotope fractionation during precipitation of Fe-sulfide precursors (Guilbaud et al. 2011b) and a globally isotopically light Fe(II) pool in seawater (Rouxel et al. 2005). The pyrite grains with positive δ^{56}Fe values may originate from Fe(III)-bearing minerals like Fe oxide or ferrihydrite (Nishizawa et al. 2010; Yoshiya et al. 2012), or equilibrium pyrite precipitation/recrystallization (Polyakov and Soultanov 2011). The high δ^{56}Fe variability observed at the grain scale or between pyrite grains also suggests strong diagenetic signals. Marin-Carbonne et al. (2014) further adressed the importance of diagenetic overprinting by investigating coupled Fe and S isotope signatures of two pyrite nodules in a ca. 2.7 Ga black shale from the Bubi greenstone belt (Zimbabwe). Spatially resolved analysis across the nodules shows a large range of variation at micrometer-scale for both Fe and S isotopic compositions that cannot be explained by combined DIR and Bacterial Sulfate Reduction (BSR) as previously proposed (Archer and Vance 2006), but rather by the contributions of different Fe and S sources during a complex diagenetic history.

Because of the complication in interpreting the Fe isotope record in pyrite, the indentification of Fe isotope biosignatures in Late Archean black shales remains a matter of debate (Rouxel et al. 2005; Yamaguchi et al. 2005; Archer and Vance 2006; Rouxel et al. 2006; Severmann et al. 2006). Since dissimilatory Fe(III) reduction has been suggested to be important on the early Earth (Vargas et al. 1998) and is known to produce significant Fe isotope fractionation that may be preserved in organic-rich sediments (Johnson et al. 2004a) and carbonates associated with IFs (Heimann et al. 2010; Craddock and Dauphas 2011), it has been hypothesized that the extreme Fe isotope fractionations in the Archean were produced by this metabolic activity (Archer and Vance 2006; Yamaguchi et al. 2007; Johnson et al. 2008a; Nishizawa et al. 2010; Yoshiya et al. 2012). In contrast, Guilbaud et al. (2011a) suggested that the strongly negative δ^{56}Fe values in > 2.4 Ga black shales could be produced solely by pyrite precipitation. However, there are numerous examples of negative δ^{56}Fe values in bulk shales (i.e., where Fe budget is not controlled by pyrite) correlating with δ^{56}Fe values in pyrite (Rouxel et al. 2006; Czaja et al. 2010) suggesting that pyrite precipitation is not the sole mechanism generating isotopically light values in black shales. Additionally, most of the low-δ^{56}Fe shales of Neoarchean and Paleoproterozoic age are enriched in Fe (i.e., Fe/Al greater than 0.5, the value of average Archean shale), and there is no correlation between Fe enrichment, δ^{56}Fe value, and the proportion of pyrite in the Fe inventories of these samples (Czaja et al. 2010; Asael et al. 2013).

To summarize, Fe isotope studies in Archean environments confirmed the existence of an isotopically negative, anoxic, Fe-rich seawater pool. This negative pool was fueled by dissimilatory Fe reduction (similar to the Fe-shuttle found in modern redox stratified basins) and/or by hydrothermal input with partial oxidation in the photic zone (process likely dominant in anoxic Archean oceans). Large variations of δ^{56}Fe in sedimentary pyrite may be diagnostic of ferruginous conditions, as recently proposed by Tahata et al. (2015). Fe isotopes may therefore prove important proxies for paleoceanographic reconstructions when used in conjunction with Fe specitation studies (Poulton et al. 2004).

CONCLUSION

Iron isotope geochemistry is among non-traditional stable isotope systems one of the most rapidly growing fields. This is justified by the ubiquity, and rich and complex chemistry of iron in natural systems. Measuring iron's chemical bonding, abundance, ratio to geochemically similar elements Zn and Mn, redox state, and electronic spin is sometimes insufficient to unravel the riddles of iron's complex geochemical and biochemical behaviors. Iron isotopes provide a unique tool to lift these uncertainties and have already found important applications in several fields:

(1) Iron isotope measurements in ancient rocks and mineral separates (oxides, carbonates, and sulfides) provide a record of the geobiochemical cycling of iron in the ocean and sediments. In particular, processes that involved oxidation or reduction of iron seem to have left an imprint in iron isotopic compositions. Iron isotopes have thus been used to trace partial oxidation of iron in the dominantly anoxic Archean ocean and dissimilatory iron reduction (a form of respiration) in banded-iron formations.

(2) Iron availability is an important factor limiting biological productivity and carbon fixation in the ocean. One of the most promising applications of Fe isotopes in the marine realm is to trace various sources of Fe to the ocean (atmospheric dust, hydrothermal vents, reducing sediments along continental margins, and oxic seafloor sediments). For example, iron isotope measurements of seawater samples from the North Atlantic Ocean show that Saharan dust aerosol is the dominant source of dissolved iron.

(3) Differences in iron metabolism between individual and sexes are manifested in the iron isotopic composition of blood. For example, blood samples from individuals affected by hereditary hemochromatosis (excessive intestinal absorption of dietary iron associated with a number of pathologies) tend to have heavy iron isotopic compositions. Iron isotopes are also fractionated along trophic chains and might be used as tracers of paleodiets.

(4) Iron isotopes have found many applications in igneous petrology. They are sensitive to partial melting, metasomatism, and magmatic differentiation. They can also help disentangle mineral zoning that arises from diffusion vs. crystal growth. Iron isotopes may even provide some insights into the conditions of core formation and the redox evolution of Earth's mantle. Extraterrestrial bodies (the Moon, Mars, meteorites) have also been studied and those measurements provide context for understanding what controls iron isotopic fractionation during magmatic processes.

(5) Studies of the iron isotopic compositions of presolar grains provide clues on the conditions of nucleosynthesis in stars. Detection of ^{60}Ni isotope variations in meteorites from the decay of ^{60}Fe ($t_{1/2}$ = 2.62 Myr) constrains the abundance of the short-lived nuclide ^{60}Fe at the formation of the solar system. The low abundance of ^{60}Fe suggests that the solar system was contaminated by the outflows of one or several massive stars.

New applications are emerging, and the iron age of stable isotope geochemistry is just starting.

ACKNOWLEDGMENTS

The extensive reviews of Adrianna Heimann, Noah Planavsky, Martin Oeser, and Fang Huang greatly improved the manuscript. Nicole Nie is thanked for discussions and assistance in preparing figures 1 and 2. This work was supported by grants from NASA (Laboratory Analysis of Returned Samples, NNX14AK09G; Cosmochemistry, OJ-30381-0036A and NNX15AJ25G) and NSF (Petrology and Geochemistry, EAR144495; Cooperative Studies of the Earth's Deep Interior, EAR150259) to N.D. OR acknowledges the support from the National Science Foundation, Europole Mer, LabexMer (ANR-10-LABX-19–01)

REFERENCES

Akerman A, Poitrasson F, Oliva P, Audry S, Prunier J, Braun JJ (2014) The isotopic fingerprint of Fe cycling in an equatorial soil-plant-water system: The Nsimi watershed, South Cameroon. Chem Geol 385:104–116

Albarède F (2015) Metal stable isotopes in the human body: a tribute of geochemistry to medicine. Elements 11:265–269

Albarède F, Beard B (2004) Analytical methods for non-traditional isotopes. Rev Mineral Geochem 55:113–152

Albarède F, Telouk P, Lamboux A, Jaouen K, Balter V (2011) Isotopic evidence of unaccounted for Fe and Cu erythropoietic pathways. Metallomics 3:926–933

Alexander C, Wang J (2001) Iron isotopes in chondrules: Implications for the role of evaporation during chondrule formation. Meteorit Planet Sci 36:419–428

Alexander COD, Grossman J, Wang J, Zanda B, Bourot-Denise M, Hewins R (2000) The lack of potassium isotopic fractionation in Bishunpur chondrules. Meteorit Planet Sci 35:859–868

Alexander CMOD, Hewins R (2004) Mass fractionation of Fe and Ni isotopes in metal in Hammadah Al Hamrah 237. Meteorit Planet Sci 39:5080

Alexander COD, Grossman JN (2005) Alkali elemental and potassium isotopic compositions of Semarkona chondrules. Meteorit Planet Sci 40:541–556

Alexander COD, Grossman J, Ebel D, Ciesla F (2008) The formation conditions of chondrules and chondrites. Science 320:1617–1619

Algeo TJ, Schwark L, Hower JC (2004) High-resolution geochemistry and sequence stratigraphy of the Hushpuckney Shale (Swope Formation, eastern Kansas): implications for climato-environmental dynamics of the Late Pennsylvanian Midcontinent Seaway. Chem Geol 206:259–288

Alt JC (1995) Subseafloor processes in mid-ocean ridge hydrothermal systems. *In:* Seafloor Hydrothermal Systems: Physical, Chemical, Biological, Geological Interactions. Geophysical Monograph 91. Humphris SE, Zierenberg RA, Mullineaux LS, Thomson RE (eds). American Geophysical Union, p 85–114

Amor M (2015) Chemical and isotopic signatures of the magnetite from magnetotactic bacteria. PhD Thesis Institut de Physique du Globe de Paris, Paris

Amor M, Busigny V, Louvat P, Gelabert A, Cartigny P, Durand-Dubief M, Ona-Nguema G, E Alphandery, I Chebbi, F Guyot. Mass-dependent and-independent signature of Fe isotopes in magnetotactic bacteria Science 352:705–708

Anand M, Russell SS, Blackhurst RL, Grady MM (2006) Searching for signatures of life on Mars: an Fe-isotope perspective. Phil Trans R Soc B: Biol Sci 361:1715–1720

Anbar AD, Rouxel O (2007) Metal stable isotopes in paleoceanography. Ann Rev Earth Planet Sci 35:717–746

Anbar AD, Jarzecki AA, Spiro TG (2005) Theoretical investigation of iron isotope fractionation between $Fe(H_2O)_6^{3+}$ and $Fe(H_2O)_6^{2+}$: Implications for iron stable isotope geochemistry. Geochim Cosmochim Acta 69:825–837

Anderson TF, Raiswell R (2004) Sources and mechanisms for the enrichment of highly reactive iron in euxinic black sea sediments. Am J Sci 304:203–233

Archer C, Vance D (2006) Coupled Fe and S isotope evidence for Archean microbial Fe(III) and sulfate reduction. Geology 34:153–156

Arnold T, Markovic T, Kirk GJD, Schonbachler M, Rehkamper M, Zhao FJ, Weiss DJ (2015) Iron and zinc isotope fractionation during uptake and translocation in rice (*Oryza sativa*) grown in oxic and anoxic soils. C R Geosci 347:397–404

Asael D, Tissot FLH, Reinhard CT, Rouxel O, Dauphas N, Lyons TW, Ponzevera E, Liorzou C, Cheron S (2013) Coupled molybdenum, iron and uranium stable isotopes as oceanic paleoredox proxies during the Paleoproterozoic Shunga Event. Chem Geol 362:193–210

Badro J, Fiquet G, Guyot F, Rueff J-P, Struzhkin VV, Vankó G, Monaco G (2003) Iron partitioning in Earth's mantle: toward a deep lower mantle discontinuity. Science 300:789–791

Balci N, Bullen TD, Witte-Lien K, Shanks WC, Motelica M, Mandernack KW (2006) Iron isotope fractionation during microbially stimulated Fe(II) oxidation and Fe(III) precipitation. Geochim Cosmochim Acta 70:622–639

Balter V, Lamboux A, Zazzo A, Telouk P, Leverrier Y, Marvel J, Moloney AP, Monahan FJ, Schmidt O, Albarede F (2013) Contrasting Cu Fe, Zn isotopic patterns in organs and body fluids of mice and sheep, with emphasis on cellular fractionation. Metallomics 5:1470–1482

Barnicoat AC, Henderson IHC, Knipe RJ, Yardley BWD, Napler RW, Fox NPC, Lawrence SR (1997) Hydrothermal gold mineralization in the Witwatersrand basin. Nature 386:820–824

Barrat J, Yamaguchi A, Greenwood R, Bohn M, Cotten J, Benoit M, Franchi I (2007) The Stannern trend eucrites: Contamination of main group eucritic magmas by crustal partial melts. Geochim Cosmochim Acta 71:4108–4124

Barrat JA, Rouxel O, Wang K, Moynier F, Yamaguchi A, Bischoff A, Langlade J (2015) Early stages of core segregation recorded by Fe isotopes in an asteroidal mantle. Earth Planet Sci Lett 419:93–100

Barton EA, Hallbauer DK (1996) Trace-element and U–Pb isotopic compositions of pyrite types in the Proterozoic Black Reef, Transvaal Sequence, South Africa: Implications on genesis and age. Chem Geol 133:173–199

Bau M, Dulski P (1996) Distribution of yttrium and rare-earth elements in the Penge and Kuruman iron-formations, Transvaal Supergroup, South Africa. Precambrian Res 79:37–55

Bau M, Moller P (1993) Rare earth element systematics of the chemically precipitated component in Early Precambrian iron formations and the evolution of the terrestrial atmopshere-hydrosphere-lithosphere system. Geochim Cosmochim Acta 57:2239–2249

Bazylinski DA, Schlezinger DR, Howes BH, Frankel RB, Epstein SS (2000) Occurence and distribution of diverse populations of magnetic protists in a chemically stratified coastal salt pond. Chem Geol 169:319–328

Beard BL, Johnson CM (1999) High precision iron isotope measurements of terrestrial and lunar materials. Geochim Cosmochim Acta 63:1653–1660

Beard BL, Johnson CM (2004a) Fe isotope variations in the modern and ancient earth and other planetary bodies. Rev Mineral Geochem 55:319–357

Beard BL, Johnson CM (2004b) Inter-mineral Fe isotope variations in mantle-derived rocks and implications for the Fe geochemical cycle. Geochim Cosmochim Acta 68:4727–4743

Beard BL, Johnson CM, Cox L, Sun H, Nealson KH, Aguilar C (1999) Iron isotope biosignatures. Science 285:1889–1892

Beard BL, Johnson CM, Skulan JL, Nealson KH, Cox L, Sun H (2003a) Application of Fe isotopes to tracing the geochemical and biological cycling of Fe. Chem Geol 195:87–117

Beard BL, Johnson CM, Von Damm KL, Poulson RL (2003b) Iron isotope constraints on Fe cycling and mass balance in oxygenated Earth oceans. Geology 31:629–632

Beard BL, Handler RM, Scherer MM, Wu L, Czaja AD, Heimann A, Johnson CM (2010) Iron isotope fractionation between aqueous ferrous iron and goethite. Earth Planet Sci Lett 295:241–250

Bekker A, Holland HD, Wang PL, RumbleIII D, Stein HJ, Hannah JL, Coetzee LL, Beukes NJ (2004) Dating the rise of atmospheric oxygen. Nature 427:117–120

Bekker A, Kaufman AJ, Karhu JA, Eriksson KA (2005) Evidence for Paleoproterozoic cap carbonates in North America. Precambrian Res 137:167–206

Bekker A, Barley ME, Fiorentini ML, Rouxel OJ, Rumble D, Beresford SW (2009) Atmospheric sulfur in Archean komatiite-hosted nickel deposits. Science 326:1086–1089

Bekker A, Slack JF, Planavsky N, Krapez B, Hofmann A, Konhauser KO, Rouxel OJ (2010) Iron formation: the sedimentary product of a complex interplay among mantle, tectonic, oceanic, biospheric processes. Econ Geol 105:467–508

Bekker A, Krapez B, Slack JF, Planavsky N, Hofmann A, Konhauser KO, Rouxel OJ (2012) Iron formation: the sedimentary product of a complex interplay among mantle, tectonic, oceanic, biospheric processes—a Reply. Econ Geol 107:379–380

Belshaw N, Zhu X, Guo Y, O'Nions R (2000) High precision measurement of iron isotopes by plasma source mass spectrometry. Inter J Mass Spectrom 197:191–195

Bennett SA, Achterberg EP, Connelly DP, Statham PJ, Fones GR, German CR (2008) The distribution and stabilisation of dissolved Fe in deep-sea hydrothermal plumes. Earth Planet Sci Lett 270:157–167

Bennett SA, Rouxel O, Schmidt K, Garbe-Schönberg D, Statham PJ, German CR (2009) Iron isotope fractionation in a buoyant hydrothermal plume, 5°S Mid-Atlantic Ridge. Geochim Cosmochim Acta 73:5619–5634

Benz M, Brune A, Schink B (1998) Anaerobic and aerobic oxidation of ferrous iron at neutral pH by chemoheterotrophic nitrate-reducing bacteria. Arch Microbiol 169:159–165

Berglund M, Wieser ME (2011) Isotopic Compositions of the Elements 2009 (IUPAC Technical Report). Pure Appl Chem 83:397–410

Bergquist BA, Boyle EA (2006) Iron isotopes in the Amazon River system: Weathering and transport signatures. Earth Planet Sci Lett 248:54–68

Bhatia MP, Kujawinski EB, Das SB, Breier CF, Henderson PB, Charette MA (2013) Greenland meltwater as a significant and potentially bioavailable source of iron to the ocean. Nat Geosci 6:274–278

Bigeleisen J, Mayer MG (1947) Calculation of equilibrium constants for isotopic exchange reactions. J Chem Phys 15:261–267

Bilenker LD, Simon AC, Reich M, Lundstrom CC, Gajos N, Bindeman I, Barra F, Munizaga R (2016) Fe–O stable isotope pairs elucidate a high-temperature origin of Chilean iron oxide-apatite deposits. Geochim Cosmochim Acta 177:94–104

Black JR, John SG, Young ED, Kavner, A (2010) Effect of temperature and mass transport on transition metal isotope fractionation during electroplating. Geochim Cosmochim Acta 74:5187–5201

Blanchard M, Poitrasson F, Meheut M, Lazzeri M, Mauri F, Balan E (2009) Iron isotope fractionation between pyrite (FeS_2), hematite (Fe_2O_3) and siderite ($FeCO_3$): A first-principles density functional theory study. Geochim Cosmochim Acta 73:6565–6578

Blanchard M, Morin G, Lazzeri M, Balan E (2010) First-principles study of the structural and isotopic properties of Al-and OH-bearing hematite. Geochim Cosmochim Acta 74:3948–3962

Blanchard M, Poitrasson F, Meheut M, Lazzeri M, Mauri F, Balan E (2012) Comment on "New data on equilibrium iron isotope fractionation among sulfides: Constraints on mechanisms of sulfide formation in hydrothermal and igneous systems" by VB Polyakov and DM Soultanov. Geochim Cosmochim Acta 87:356–359

Blanchard M, Dauphas N, Hu M, Roskosz M, Alp E, Golden D, Sio C, Tissot F, Zhao J, Gao L (2015) Reduced partition function ratios of iron and oxygen in goethite. Geochim Cosmochim Acta 151:19–33
Borrok D, Wanty R, Ridley W, Wolf R, Lamothe P, Adams M (2007) Separation of copper, iron, zinc from complex aqueous solutions for isotopic measurement. Chem Geol 242:400–414
Bowen N (1928) The Evolution of the Igneous Rocks Princeton University Press. Princeton, New Jersey
Boyle EA, Bergquist BA, Kayser RA, Mahowald, N (2005) Iron, manganese, lead at Hawaii Ocean Time-series station ALOHA: Temporal variability and an intermediate water hydrothermal plume. Geochim Cosmochim Acta 69:933–952
Brantley SL, Liermann LJ, Guynn RL, Anbar A, Icopini GA, Barling, J (2004) Fe isotopic fractionation during mineral dissolution with and without bacteria. Geochim Cosmochim Acta 68:3189–3204
Briat JF, Lobreaux S (1997) Iron transport and storage in plants. Trends Plant Sci 2:187–193
Brumsack H-J (2006) The trace metal content of recent organic carbon-rich sediments: Implications for Cretaceous black shale formation. Palaeogeogr Palaeoclimatol Palaeoecol 232:344– 361
Bullen TD, McMahon PM (1998) Using stable Fe isotopes to assess microbially mediated Fe^{3+} reduction in a jet-fuel contaminated aquifer. Mineral Mag 62A:255–256
Bullen TD, White AF, Childs CW, Vivit DV, Schulz MS (2001) Demonstration of significant abiotic iron isotope fractionation in nature. Geology 29:699–702
Busigny V, Planavsky NJ, Jezequel D, Crowe S, Louvat P, Moureau J, Viollier E, Lyons TW (2014) Iron isotopes in an Archean ocean analogue. Geochim Cosmochim Acta 133:443–462
Butler A (2005) Marine siderophores and microbial iron mobilization. Biometals 18:369–374
Cameron EM (1982) Sulphate and sulphate reduction in early Precambrian oceans. Nature 296:45–148
Canfield DE (1998) A new model for Proterozoic ocean chemistry. Nature 396:450–453
Canil D, O'Neill HSC, Pearson D, Rudnick R, McDonough W, Carswell D (1994) Ferric iron in peridotites and mantle oxidation states. Earth Planet Sci Lett 123:205–220
Carazzo G, Jellinek AM, Turchyn AV (2013) The remarkable longevity of submarine plumes: Implications for the hydrothermal input of iron to the deep-ocean. Earth Planet Sci Lett 382:66–76
Chapman JB, Weiss DJ, Shan Y, Lemburger, M (2009) Iron isotope fractionation during leaching of granite and basalt by hydrochloric and oxalic acids. Geochim Cosmochim Acta 73:1312–1324
Charlier B, Ginibre C, Morgan D, Nowell G, Pearson D, Davidson J, Ottley C (2006) Methods for the microsampling and high-precision analysis of strontium and rubidium isotopes at single crystal scale for petrological and geochronological applications. Chem Geol 232:114–133
Chase Z, Johnson KS, Elrod VA, Plant JN, Fitzwater SE, Pickell L, Sakamoto CM (2005) Manganese and iron distributions off central California influenced by upwelling and shelf width. Mar Chem 95:235–254
Chen J-B, Busigny V, Gaillardet J, Louvat P, Wang Y-N (2014) Iron isotopes in the Seine River (France): Natural versus anthropogenic sources. Geochim Cosmochim Acta 128:128–143
Chen Y Su, S He, Y Li S, Hou J, Feng S, Gao K (2014) Fe isotope compositions and implications on mineralization of Xishimen iron deposit in Wuan, Hebei. Acta Petrolog Sinica 30:3443–3454
Cheng Y, Mao J, Zhu X, Wang, Y (2015) Iron isotope fractionation during supergene weathering process and its application to constrain ore genesis in Gaosong deposit, Gejiu district, SW China. Gondwana Res 27:1283–1291
Chever F, Rouxel OJ, Croot PL, Ponzevera E, Wuttig K, Auro, M (2015) Total dissolvable and dissolved iron isotopes in the water column of the Peru upwelling regime. Geochim Cosmochim Acta 162:66–82
Chu NC, Johnson CM, Beard BL, German CR, Nesbitt RW, Frank M, Bohn M, Kubik PW, Usui A, Graham I (2006) Evidence for hydrothermal venting in Fe isotope compositions of the deep Pacific Ocean through time. Earth Planet Sci Lett 245:202–217
Cloud PE (1973) Paleoecological significance of banded iron-formation. Economic Geology 68:1135–1143
Conway TM, John SG (2014) Quantification of dissolved iron sources to the North Atlantic Ocean. Nature 511:212–215
Conway TM, Rosenberg AD, Adkins JF, John SG (2013) A new method for precise determination of iron, zinc and cadmium stable isotope ratios in seawater by double-spike mass spectrometry. Analytica Chimica Acta 793:44–52
Costa F, Dohmen R, Chakraborty S (2008) Time scales of magmatic processes from modeling the zoning patterns of crystals. Rev Mineral Geochem 69:545–594
Craddock PR, Dauphas N (2011a) Iron isotopic compositions of geological reference materials and chondrites. Geostand Geoanal Res 35:101–123
Craddock PR, Dauphas N (2011b) Iron and carbon isotope evidence for microbial iron respiration throughout the Archean. Earth Planet Sci Lett 303:121–132
Craddock PR, Warren JM, Dauphas N (2013) Abyssal peridotites reveal the near-chondritic Fe isotopic composition of the Earth. Earth Planet Sci Lett 365:63–76
Crisp JA (1984) Rates of magma emplacement and volcanic output. J Volcanol Geotherm Res 20:177–211
Croal LR, Johnson CM, Beard BL, Newman DK (2004) Iron isotope fractionation by Fe(II)-oxidizing photoautotrophic bacteria. Geochim Cosmochim Acta 68:1227–1242

Crosby HA, Johnson CM, Roden EE, Beard BL (2005) Coupled Fe(II)–Fe(III) electron and atom exchange as a mechanism for Fe isotope fractionation during dissimilatory iron oxide reduction. Environ Sci Technol 39:6698–6704, doi:10.1021/es0505346

Crosby HA, Roden EE, Johnson CM, Beard BL (2007) The mechanisms of iron isotope fractionation produced during dissimilatory Fe(III) reduction by *Shewanella putrefaciens* and *Geobacter sulfurreducens*. Geobiology 5:169–189

Czaja AD, Johnson CM, Beard BL, Eigenbrode JL, Freeman KH, Yamaguchi KE (2010) Iron and carbon isotope evidence for ecosystem and environmental diversity in the similar to 2.7 to 2.5 Ga Hamersley Province, Western Australia. Earth Planet Sci Lett 292:170–180

d'Abzac F-X, Beard BL, Czaja AD, Konishi H, Schauer JJ, Johnson CM (2013) Iron isotope composition of particles produced by UV-femtosecond laser ablation of natural oxides, sulfides, carbonates. Anal Chem 85:11885–11892

d'Abzac FX, Czaja AD, Beard BL, Schauer JJ, Johnson CM (2014) Iron distribution in size-resolved aerosols generated by UV-femtosecond laser ablation: influence of cell geometry and implications for in situ isotopic determination by LA-MC-ICP-MS Geostand Geoanal Res 38:293–309

Dauphas N (2007) Diffusion-driven kinetic isotope effect of Fe and Ni during formation of the Widmanstatten pattern. Meteorit Planet Sci 42:1597–1613

Dauphas N, Rouxel O (2006) Mass spectrometry and natural variations of iron isotopes. Mass Spectrometry Reviews 25:515–550

Dauphas N, Schauble E (2016) Mass fractionation laws, mass-independent effects, isotopic anomalies. Ann Rev Earth Planet Sci 44:709–783

Dauphas N, Janney PE, Mendybaev RA, Wadhwa M, Richter FM, Davis AM, van Zuilen M, Hines R, Foley CN (2004a) Chromatographic separation and multicollection-ICPMS analysis of iron. Investigating mass-dependent and-independent isotope effects. Anal Chem 76:5855–5863

Dauphas N, van Zuilen M, Wadhwa M, Davis AM, Marty B, Janney PE (2004b) Clues from Fe isotope variations on the origin of early Archean BIFs from Greenland. Science 306:2077–2080

Dauphas N, Cates NL, Mojzsis SJ, Busigny V (2007a) Identification of chemical sedimentary protoliths using iron isotopes in the >3750 Ma Nuvvuagittuq supracrustal belt, Canada. Earth Planet Sci Lett 254:358–376

Dauphas N, Van Zuilen M, Busigny V, Lepland A, Wadhwa M, Janney PE (2007b) Iron isotope, major and trace element characterization of early Archean supracrustal rocks from SW Greenland: Protolith identification and metamorphic overprint. Geochim Cosmochim Acta 71:4745–4770

Dauphas N, Cook DL, Sacarabany A, Frohlich C, Davis AM, Wadhwa M, Pourmand A, Rauscher T, Gallino R (2008) Iron-60 evidence for early injection and efficient mixing of stellar debris in the protosolar nebula. Astrophys J 686:560–569

Dauphas N, Pourmand A, Teng F-Z (2009a) Routine isotopic analysis of iron by HR-MC-ICPMS: How precise and how accurate? Chem Geol 267:175–184

Dauphas N, Craddock PR, Asimow PD, Bennett VC, Nutman AP, Ohnenstetter D (2009b) Iron isotopes may reveal the redox conditions of mantle melting from Archean to Present. Earth Planet Sci Lett 288:255–267

Dauphas N, Teng F-Z, Arndt NT (2010) Magnesium and iron isotopes in 2.7 Ga Alexo komatiites: Mantle signatures, no evidence for Soret diffusion, identification of diffusive transport in zoned olivine. Geochim Cosmochim Acta 74:3274–3291

Dauphas N, Roskosz M, Alp E, Golden D, Sio C, Tissot F, Hu M, Zhao J, Gao L, Morris R (2012) A general moment NRIXS approach to the determination of equilibrium Fe isotopic fractionation factors: application to goethite and jarosite. Geochim Cosmochim Acta 94:254–275

Dauphas N, Roskosz M, Alp E, Neuville D, Hu M, Sio C, Tissot F, Zhao J, Tissandier L, Médard E (2014) Magma redox and structural controls on iron isotope variations in Earth's mantle and crust. Earth Planet Sci Lett 398:127–140

Dauphas N, Poitrasson F, Burkhardt C, Kobayashi H, Kurosawa K (2015) Planetary and meteoritic Mg/Si and δ^{30}Si variations inherited from solar nebula chemistry. Earth Planet Sci Lett 427:236–248

Debret B, Millet M-A, Pons M-L, Bouihol P, Inglis E, Williams H (2016) Isotopic evidence for iron mobility during subduction. Geology 44:215–218

de Jong J, Schoemann V, Tison JL, Becquevort S, Masson F, Lannuzel D, Petit J, Chou L, Weis D, Mattielli, N (2007) Precise measurement of Fe isotopes in marine samples by multi-collector inductively coupled plasma mass spectrometry (MC-ICP-MS). Anal Chim Acta 589:105–119

Dideriksen K, Baker J, Stipp S (2006) Iron isotopes in natural carbonate minerals determined by MC-ICP-MS with a ^{58}Fe–^{54}Fe double-spike. Geochim Cosmochim Acta 70:118–132

Dideriksen K, Baker JA, Stipp SLS (2008) Equilibrium Fe isotope fractionation between inorganic aqueous Fe (III) and the siderophore complex Fe (III)-desferrioxamine B. Earth Planet Sci Lett 269:280–290

Dodson M (1963) A theoretical study of the use of internal standards for precise isotopic analysis by the surface ionization technique: Part I—General first-order algebraic solutions. J Sci Instrum 40:289

Dohmen R, Chakraborty S (2007) Fe–Mg diffusion in olivine II: point defect chemistry, change of diffusion mechanisms and a model for calculation of diffusion coefficients in natural olivine. Phys Chem Mineral 34:409–430

Domagal-Goldman SD, Kubicki JD (2008) Density functional theory predictions of equilibrium isotope fractionation of iron due to redox changes and organic complexation. Geochim Cosmochim Acta 72:5201–5216

Dominguez G, Wilkins G, Thiemens MH (2011) The Soret effect and isotopic fractionation in high-temperature silicate melts. Nature 473:70–73

dos Santos Pinheiro GM, Poitrasson F, Sondag F, Vieira LC, Pimentel MM (2013) Iron isotope composition of the suspended matter along depth and lateral profiles in the Amazon River and its tributaries. J South Am Earth Sci 44:35–44

Duan Y, Severmann S, Anbar AD, Lyons TW, Gordon GW, Sageman BB (2010) Isotopic evidence for Fe cycling and repartitioning in ancient oxygen-deficient settings: Examples from black shales of the mid-to-late Devonian Appalachian basin. Earth Planet Sci Lett 290:244–253

Dziony W, Horn I, Lattard D, Koepke J, Steinhoefel G, Schuessler JA, Holtz F (2014) In-situ Fe isotope ratio determination in Fe–Ti oxides and sulfides from drilled gabbros and basalt from the IODP Hole 1256D in the eastern equatorial Pacific. Chem Geol 363:101–113

Edwards KJ, Bond PL, Gihring TM, Banfield JF (2000) An archaeal iron-oxidizing extreme acidophile important in acid mine drainage. Science 287:1796–1799

Ellwood MJ, Hutchins DA, Lohan MC, Milne A, Nasemann P, Nodder SD, Sander SG, Strzepek R, Wilhelm SW, Boyd PW (2015) Iron stable isotopes track pelagic iron cycling during a subtropical phytoplankton bloom. PNAS 112:E15–E20

Elrod VA, Berelson WM, Coale KH, Johnson KS (2004) The flux of iron from continental shelf sediments: A missing source for global budgets. Geophys Res Lett 31:10.1029/2004GL020216

Emerson D, Moyer C (1997) Isolation and characterization of novel iron-oxidizing bacteria that grow at circumneutral pH Appl Environ Microbiol 61:2681–2687

Emmanuel S, Schuessler JA, Vinther J, Matthews A, von Blanckenburg F (2014) A preliminary study of iron isotope fractionation in marine invertebrates (chitons, Mollusca) in near-shore environments. Biogeosciences 11:5493–5502

England GL, Rasmussen B, Krapez B, Groves DI (2002) Palaeoenvironmental significance of rounded pyrite in siliciclastic sequences of the Late Archaean Witwatersrand. Sedimentology 49:1133–1156

Escoube R, Rouxel OJ, Sholkovitz E, Donard OF (2009) Iron isotope systematics in estuaries: The case of North River, Massachusetts (USA). Geochim Cosmochim Acta 73:4045–4059

Escoube R, Rouxel OJ, Pokrovsky OS, Schroth A, Holmes RM, Donard, OFX (2015) Iron isotope systematics in Arctic rivers. C R Geosci 347:377–385

Falkowski PG (1997) Evolution of the nitrogen cycle and its influence on the biological sequestration of CO_2 in the ocean. Nature 387:272–275

Fantle MS, DePaolo DJ (2004) Iron isotopic fractionation during continental weathering. Earth Planet Sci Lett 228:547–562

Farquhar J, Bao H, Thiemens M (2000) Atmospheric influence of Earth's earliest sulfur cycle. Science 289:756–758

Farquhar J, Peters M, Johnston DT, Strauss H, Masterson A, Wiechert U, Kaufman AJ (2007) Isotopic evidence for *Mesoarchaean anoxia* and changing atmospheric sulphur chemistry. Nature 449:706–709

Fiorentini ML, Bekker A, Rouxel O, Wing BA, Maier W, Rumble D (2012) Multiple sulfur and iron isotope composition of magmatic Ni–Cu–(PGE) sulfide mineralization from Eastern Botswana. Econ Geol 107:105–116

Fitzsimmons JN, Boyle EA, Jenkins WJ (2014) Distal transport of dissolved hydrothermal iron in the deep South Pacific Ocean. PNAS 111:16654–16661

Fitzsimmons JN, Carrasco GG Wu J Roshan S Hatta M Measures CI, Conway TM, John SG, Boyle EA (2015) Partitioning of dissolved iron and iron isotopes into soluble and colloidal phases along the GA03 GEOTRACES North Atlantic Transect. Deep Sea Research Part II 116:130–151

Foden J, Sossi PA, Wawryk CM (2015) Fe isotopes and the contrasting petrogenesis of A-, I-and S-type granite. Lithos 212:32–44

Frank M (2002) Radiogenic isotopes: Tracers of past ocean circulation and erosional input. Rev Geophys 40, doi:100110.1029/2000rg000094

Frankel RB, Blakemore RP, Wolfe RS (1979) Magnetite in freshwater magnetotactic bacteria. Science 203:1355–1356

Frierdich AJ, Beard BL, Reddy TR, Scherer MM, Johnson CM (2014a) Iron isotope fractionation between aqueous Fe (II) and goethite revisited: New insights based on a multi-direction approach to equilibrium and isotopic exchange rate modification. Geochim Cosmochim Acta 139:383–398

Frierdich AJ, Beard BL, Scherer MM, Johnson CM (2014b) Determination of the Fe $(II)_{aq}$–magnetite equilibrium iron isotope fractionation factor using the three-isotope method and a multi-direction approach to equilibrium. Earth Planet Sci Lett 391:77–86

Frost DJ, Liebske C, Langenhorst F, McCammon CA, Trønnes RG, Rubie DC (2004) Experimental evidence for the existence of iron-rich metal in the Earth's lower mantle. Nature 428:409–412

Frost CD, von Blanckenburg F, Schoenberg R, Frost BR, Swapp SM (2007) Preservation of Fe isotope heterogeneities during diagenesis and metamorphism of banded iron formation. Contrib Mineral Petrol 153:211–235

Fujii T, Moynier Fdr, Telouk P, Albarède F (2006) Isotope fractionation of iron(III) in chemical exchange reactions using solvent extraction with crown ether. J Phys Chem A 110:11108–11112

Fujii T, Moynier F, Blichert-Toft J, Albarède F (2014) Density functional theory estimation of isotope fractionation of Fe Ni Cu, Zn among species relevant to geochemical and biological environments. Geochim Cosmochim Acta 140:553–576

Fung IY, Meyn SK, Tegen I Doney SC, John JG, Bishop, JKB (2000) Iron supply and demand in the upper ocean. Global Biogeochem Cycles 14:281–295

Gall L, Williams HM, Siebert C, Halliday AN, Herrington RJ, Hein JR (2013) Nickel isotopic compositions of ferromanganese crusts and the constancy of deep ocean inputs and continental weathering effects over the Cenozoic. Earth Planet Sci Lett 375:148–155

German CR, Von Damm KL (2003) Hydrothermal processes. *In:* The Oceans and Marine Geochemistry. Treatise on Geochemistry Volume 6, pp.181–222

Graham S, Pearson N, Jackson S, Griffin W, O'Reilly S (2004) Tracing Cu and Fe from source to porphyry: in situ determination of Cu and Fe isotope ratios in sulfides from the Grasberg Cu–Au deposit. Chem Geol 207:147–169

Guelke M, von Blanckenburg F (2007) Fractionation of stable iron isotopes in higher plants. Environ Sci Technol 41:1896–1901

Guelke M, von Blanckenburg F, Schoenberg R, Staubwasser M, Stuetzel, H (2010) Determining the stable Fe isotope signature of plant-available iron in soils. Chem Geol 277:269–280

Guelke-Stelling M, von Blanckenburg F (2012) Fe isotope fractionation caused by translocation of iron during growth of bean and oat as models of strategy I and II plants. Plant Soil 352:217–231

Guilbaud R, Butler IB, Ellam RM, Rickard D, Oldroyd A (2011a) Experimental determination of the equilibrium Fe^{2+} isotope fractionation between and FeSm (mackinawite) at 25 and 2 °C Geochim Cosmochim Acta 75:2721–2734

Guilbaud R, Butler IB, Ellam RM (2011b) Abiotic pyrite formation produces a large fe isotope fractionation. Science 332:1548–1551

Guilbaud R, Butler IB, Ellam RM (2012) Response to Comment on "Abiotic pyrite formation produces a large Fe isotope fractionation". Science 335:538

Günther D, Heinrich CA (1999) Enhanced sensitivity in laser ablation-ICP mass spectrometry using helium-argon mixtures as aerosol carrier. J Anal At Spectrom 14:1363–1368

Halama M, Swanner ED, Konhauser KO, Kappler A (2016) Evaluation of siderite and magnetite formation in BIFs by pressure-temperature experiments of Fe(III) minerals and microbial biomass. Earth Planet Sci Lett 450:243–253

Halverson GP, Poitrasson F, Hoffman PF, Nedelec A, Montel JM, Kirby J (2011) Fe isotope and trace element geochemistry of the Neoproterozoic syn-glacial Rapitan iron formation. Earth Planet Sci Lett 309:100–112

Hannington MD, Jonasson IR, Herzig PM, Petersen S (1995) Physical and chemical processes of seafloor mineralization at mid-ocean ridges. *In:* Seafloor Hydrothermal Systems: Physical, Chemical, Biological, Geological Interactions, SE Humphris, RA Zierenberg, LS Mullineaux, RE Thomson (eds), American Geophysical Union, Washington, D C. doi:10.1029/GM091p0115

Harvey LJ, Armah CN, Dainty JR, Foxall RJ, Lewis DJ, Langford NJ, Fairweather-Tait SJ (2005) Impact of menstrual blood loss and diet on iron deficiency among women in the UK Br J Nutr 94:557–564

Haugaard R, Pecoits E, Lalonde SV, Rouxel OJ, Konhauser KO (2016) The Joffre Banded Iron Formation, Hamersley Group, Western Australia: Assessing the palaeoenvironment through detailed petrology and chemostratigraphy. Precambrian Res 273:12–37

Hawkings JR, Wadham JL, Tranter M, Raiswell R, Benning LG, Statham PJ, Tedstone A, Nienow P, Lee K, Telling J (2014) Ice sheets as a significant source of highly reactive nanoparticulate iron to the oceans. Nat Commun 5,:doi: 10.1038/ncomms4929

Heimann A, Beard BL, Johnson CM (2008) The role of volatile exsolution and sub-solidus fluid/rock interactions in producing high Fe–56/Fe–54 ratios in siliceous igneous rocks. Geochim Cosmochim Acta 72:4379–4396

Heimann A, Johnson CM, Beard BL, Valley JW, Roden EE, Spicuzza MJ, Beukes NJ (2010) Fe C, O isotope compositions of banded iron formation carbonates demonstrate a major role for dissimilatory iron reduction in similar to 2.5 Ga marine environments. Earth Planet Sci Lett 294:8–18

Herzfeld KF, Teller E (1938) The vapor pressure of isotopes. Phys Rev 54:912

Hezel DC, Needham AW, Armytage R, Georg B, Abel RL, Kurahashi E, Coles BJ, Rehkämper M, Russell SS (2010) A nebula setting as the origin for bulk chondrule Fe isotope variations in CV chondrites. Earth Planet Sci Lett 296:423–433

Hibbert K, Williams H, Kerr AC, Puchtel I (2012) Iron isotopes in ancient and modern komatiites: evidence in support of an oxidised mantle from Archean to present. Earth Planet Sci Lett 321:198–207
Hiebert RS, Bekker A, Wing BA, Rouxel OJ (2013) The role of paragneiss assimilation in the origin of the voisey's bay Ni–Cu sulfide deposit, labrador: multiple S and Fe isotope evidence. Econ Geol 108:1459–1469
Hiebert RS, Bekker A, Houlé MG, Wing BA, Rouxel OJ (2016) Tracing sources of crustal contamination using multiple S and Fe isotopes in the Hart komatiite-associated Ni–Cu–PGE sulfide deposit, Abitibi greenstone belt, Ontario, Canada. Miner Deposita 51:919–935
Hill PS, Schauble EA (2008) Modeling the effects of bond environment on equilibrium iron isotope fractionation in ferric aquo-chloro complexes. Geochim Cosmochim Acta 72:1939–1958
Hill PS, Schauble EA, Shahar A, Tonui E, Young ED (2009) Experimental studies of equilibrium iron isotope fractionation in ferric aquo-chloro complexes. Geochim Cosmochim Acta 73:2366–2381
Hin RC, Schmidt MW, Bourdon B (2012) Experimental evidence for the absence of iron isotope fractionation between metal and silicate liquids at 1 GPa and 1250–1300 °C and its cosmochemical consequences. Geochim Cosmochim Acta 93:164–181
Hofmann A, Bekker A, Rouxel O, Rumble D, Master S (2009) Multiple sulphur and iron isotope composition of detrital pyrite in Archaean sedimentary rocks: a new tool for provenace analysis. Earth Planet Sci Lett 286:436–445
Hofmann A, Bekker A, Dirks P, Gueguen B, Rumble D, Rouxel OJ (2014) Comparing orthomagmatic and hydrothermal mineralization models for komatiite-hosted nickel deposits in Zimbabwe using multiple-sulfur, iron, nickel isotope data. Mineralium Deposita 49:75–100
Holland HD (1984) The Chemical Evolution of the Atmosphere and Oceans. Princeton Univ. Press., New York
Homoky WB, Severmann S, Mills RA, Statham PJ, Fones GR (2009) Pore-fluid Fe isotopes reflect the extent of benthic Fe redox recycling: Evidence from continental shelf and deep-sea sediments. Geology 37:751–754
Homoky WB, John SG, Conway TM, Mills RA (2013) Distinct iron isotopic signatures and supply from marine sediment dissolution. Nat Commun 4, doi: 10.1038/ncomms3143
Horn I, von Blanckenburg F, Schoenberg R, Steinhoefel G, Markl G (2006) In situ iron isotope ratio determination using UV-femtosecond laser ablation with application to hydrothermal ore formation processes. Geochim Cosmochim Acta 70:3677–3688
Horn I, von Blanckenburg F (2007) Investigation on elemental and isotopic fractionation during 196 nm femtosecond laser ablation multiple collector inductively coupled plasma mass spectrometry. Spectrochim Acta Part B: At Spectr 62:410–422
Horner TJ, Schönbächler M, Rehkämper M, Nielsen SG, Williams H, Halliday AN, Xue Z, Hein JR (2010) Ferromanganese crusts as archives of deep water Cd isotope compositions. G-cubed: doi:10.1029/2009GC002987
Horner TJ, Williams HM, Hein JR, Saito MA, Burton KW, Halliday AN, Nielsen SG (2015) Persistence of deeply sourced iron in the Pacific Ocean. PNAS 112:1292–1297
Hotz K, Walczyk T (2013) Natural iron isotopic composition of blood is an indicator of dietary iron absorption efficiency in humans. J Biol Inorg Chem 18:1–7
Hotz K, Augsburger H, Walczyk T (2011) Isotopic signatures of iron in body tissues as a potential biomarker for iron metabolism. J Anal At Spectrom 26:1347–1353
Hotz K, Krayenbuehl PA, Walczyk T (2012) Mobilization of storage iron is reflected in the iron isotopic composition of blood in humans. J Biol Inorg Chem 17:301–309
Hu MY, Sturhahn W, Toellner TS, Mannheim PD, Brown DE, Zhao J, Alp EE (2003) Measuring velocity of sound with nuclear resonant inelastic X-ray scattering. Phys Rev B 67:094304
Hu MY, Toellner TS, Dauphas N, Alp EE, Zhao J (2013) Moments in nuclear resonant inelastic x-ray scattering and their applications. Phys Rev B 87:064301
Huang F, Lundstrom C, Glessner J, Ianno A, Boudreau A, Li J, Ferré E, Marshak S, DeFrates J (2009) Chemical and isotopic fractionation of wet andesite in a temperature gradient: experiments and models suggesting a new mechanism of magma differentiation. Geochim Cosmochim Acta 73:729–749
Huang F, Chakraborty P, Lundstrom C, Holmden C, Glessner J, Kieffer S, Lesher C (2010) Isotope fractionation in silicate melts by thermal diffusion. Nature 464:396–400
Huang F, Zhang Z, Lundstrom CC, Zhi X (2011) Iron and magnesium isotopic compositions of peridotite xenoliths from Eastern China. Geochim Cosmochim Acta 75:3318–3334
Humayun M, Clayton RN (1995a) Precise determination of the isotopic composition of potassium: Application to terrestrial rocks and lunar soils. Geochim Cosmochim Acta 59:2115–2130
Humayun M, Clayton RN (1995b) Potassium isotope cosmochemistry: Genetic implications of volatile element depletion. Geochim Cosmochim Acta 59:2131–2148
Humayun M, Qin L, Norman MD (2004) Geochemical evidence for excess iron in the mantle beneath Hawaii. Science 306:91–94

Humphris SE, Herzig PM, Miller DJ, Alt JC, Becker K, Brown D, Brugmann G, Chiba H, Fouquet Y, Gemmell JB, Guerin G, Hannington MD, Holm NG, Honnorez JJ, Iturrino GJ, Knott R, Ludwig R, Nakamura K, Petersen S, Reysenbach AL, Rona PA, Smith S, Sturz AA, Tivey MK, Zhao X (1995) The internal structure of an active sea-floor massive sulfide deposit. Nature 377:713–716

Hutchins DA, Witter AE, Butler A, Luther III GW (1999) Competition among marine phytoplankton for different chelated iron species. Nature 400:858–861

Hyslop EV, Valley JW, Johnson CM, Beard BL (2008) The effects of metamorphism on O and Fe isotope compositions in the Biwabik Iron Formation, Northern Minnesota. Contrib Mineral Petrol 155:313–328

Icopini GA, Anbar AD, Ruebush SS, Tien M, Brantley SL (2004) Iron isotope fractionation during microbial reduction of iron: The importance of adsorption. Geology 32:205–208

Ilina SM, Poitrasson F, Lapitskiy SA, Alekhin YV, Viers J, Pokrovsky OS, (2013) Extreme iron isotope fractionation between colloids and particles of boreal and temperate organic-rich waters. Geochim Cosmochim Acta 101:96–111

Ingri J, Malinovsky D, Rodushkin I, Baxter DC, Widerlund A, Andersson P, Gustafsson O, Forsling W, Ohlander, B (2006) Iron isotope fractionation in river colloidal matter. Earth Planet Sci Lett 245:792–798

Jaouen K, Balter V (2014) Menopause effect on blood Fe and Cu isotope compositions. Am J Phys Anthropol 153:280–285

Jaouen K, Balter V, Herrscher E, Lamboux A, Telouk P, Albarede F (2012) Fe and Cu stable isotopes in archeological human bones and their relationship to sex. Am J Phys Anthropol 148:334–340

Jaouen K, Gibert M, Lamboux A, Telouk P, Fourel F, Albareede F, Alekseev AN, Crubeezy E, Balter V (2013a) Is aging recorded in blood Cu and Zn isotope compositions? Metallomics 5:1016–1024

Jaouen K, Pons M-L, Balter V (2013b) Iron, copper and zinc isotopic fractionation up mammal trophic chains. Earth Planet Sci Lett 374:164–172

Jarzecki A, Anbar A, Spiro T (2004) DFT analysis of $Fe(H_2O)_6^{3+}$ and $Fe(H_2O)_6^{2+}$ structure and vibrations; implications for isotope fractionation. J Phys Chem A 108:2726–2732

Jeandel C, Peucker-Ehrenbrink B, Jones M, Pearce C, Oelkers EH, Godderis Y, Lacan F, Aumont O, Arsouze, T (2011) Ocean margins: The missing term in oceanic element budgets? Eos 92:217

Jenkyns HC, Matthews A, Tsikos H, Erel Y (2007) Nitrate reduction, sulfate reduction, sedimentary iron isotope evolution during the Cenomanian–Turonian oceanic anoxic event. Paleoceanography:PA3208,doi:3210.102 9/2006PA001355

Jickells TD, Spokes LJ (2001) Atmospheric iron inputs to the oceans. *In:* DR Turner, KA Hunter (Eds.) The Biogeochemistry of Iron in Seawater pp. 85–118. John Wiley, Hoboken, NJ

Jickells TD, An ZS, Andersen KK, Baker AR, Bergametti G, Brooks N, Cao JJ, Boyd PW, Duce RA, Hunter KA, Kawahata H (2005) Global iron connections between desert dust, ocean biogeochemistry, climate. Science 308:67–71

John SG (2012) Optimizing sample and spike concentrations for isotopic analysis by double-spike ICPMS J Anal At Spectrom 27:2123

John SG, Adkins JF (2010) Analysis of dissolved iron isotopes in seawater. Mar Chem 119:65–76

John SG, Adkins JF (2012) The vertical distribution of iron stable isotopes in the North Atlantic near Bermuda. Global Biogeochem Cycles 26, doi: 10.1029/2011GB004043

John SG, Conway TM (2013) A role for scavenging in the marine biogeochemical cycling of zinc and zinc isotopes. Earth Planet Sci Lett 394:159–167

John SG, Geis RW, Saito MA, Boyle EA (2007) Zinc isotope fractionation during high-affinity and low-affinity zinc transport by the marine diatom *Thalassiosira oceanica*. Limnol Oceanogr 52:2710–2714

John SG, Mendez J, Moffett J, Adkins JF (2012a) The flux of iron and iron isotopes from San Pedro Basin sediments. Geochim Cosmochim Acta 93:14–29

John SG, King A, Hutchins D, Adkins JF Fu F, Wasson A, Hodierne, C (2012b) Biological, chemical, electrochemical, photochemical fractionation of Fe isotopes. AGU Fall Meeting Abstracts

Johnson CM, Beard BL (1999) Correction of instrumentally produced mass fractionation during isotopic analysis of Fe by thermal ionization mass spectrometry. Inter J Mass Spectrom 193:87–99

Johnson KS, Chavez FP, Friederich GE (1999) Continental-shelf sediment as a primary source of iron for coastal phytoplankton. Nature 398:697–700

Johnson CM, Skulan JL, Beard BL, Sun H, Nealson KH, Braterman PS (2002) Isotopic fractionation between Fe(III) and Fe(II) in aqueous solutions. Earth Planet Sci Lett 195:141–153

Johnson CM, Beard BL, Beukes NJ, Klein C, O'Leary JM (2003) Ancient geochemical cycling in the Earth as inferred from Fe isotope studies of banded iron formations from the Transvaal Craton. Contrib Mineral Petrol 144:523–547

Johnson CM, Beard BL, Roden EE, Newman DK, Nealson KH (2004) Isotopic constraints on biogeochemical cycling of Fe. Rev Mineral Geochem 55:359–408

Johnson CM, Roden EE, Welch SA, Beard BL (2005) Experimental constraints on Fe isotope fractionation during magnetite and Fe carbonate formation coupled to dissimilatory hydrous ferric oxide reduction. Geochim Cosmochim Acta 69:963–993

Johnston DT, Poulton SW, Fralick PW, Wing BA, Canfield DE, Farquhar J (2006) Evolution of the oceanic sulfur cycle at the end of the Paleoproterozoic. Geochim Cosmochim Acta 70:5723–5739
Johnson CM, Beard BL, Roden EE (2008a) The iron isotope fingerprints of redox and biogeochemical cycling in the modern and ancient Earth. Ann Rev Earth Planet Sci 36:457–493
Johnson CM, Beard BL, Klein C, Beukes NJ, Roden EE (2008b) Iron isotopes constrain biologic and abiologic processes in banded iron formation genesis. Geochim Cosmochim Acta 72:151–169
Johnson CM, Bell K, Beard BL, Shultis AI (2010) Iron isotope compositions of carbonatites record melt generation, crystallization, late-stage volatile-transport processes. Mineral Petrol 98:91–110
Johnson CM, Ludois JM, Beard BL, Beukes NJ, Heimann A (2013) Iron formation carbonates: Paleoceanographic proxy or recorder of microbial diagenesis? Geology 41:1147–1150
Karhu JA, Holland HD (1996) Carbon isotopes and the rise of atmospheric oxygen. Geology 24:867–870
Kavner A, Bonet F, Shahar A, Simon J, Young, E (2005) The isotopic effects of electron transfer: An explanation for Fe isotope fractionation in nature. Geochim Cosmochim Acta 69:2971–2979
Kehm K, Hauri E, Alexander COD, Carlson R (2003) High precision iron isotope measurements of meteoritic material by cold plasma ICP-MS Geochim Cosmochim Acta 67:2879–2891
Kiczka M, Wiederhold JG, Frommer J, Kraemer SM, Bourdon B, Kretzschmar, R (2010) Iron isotope fractionation during proton- and ligand-promoted dissolution of primary phyllosilicates. Geochim Cosmochim Acta 74:3112–3128
Kieffer SW (1982) Thermodynamics and lattice vibrations of minerals: 5. Applications to phase equilibria, isotopic fractionation, high-pressure thermodynamic properties. Rev Geophys 20:827–849
Kita N, Huberty J, Kozdon R, Beard B, Valley J (2011) High-precision SIMS oxygen, sulfur and iron stable isotope analyses of geological materials: accuracy, surface topography and crystal orientation. Surf Interfac Anal 43:427–431
Košler J, Pedersen RB, Kruber C, Sylvester PJ (2005) Analysis of Fe isotopes in sulfides and iron meteorites by laser ablation high-mass resolution multi-collector ICP mass spectrometry. J Anal At Spectrom 20:192–199
Krawczynski MJ, Van Orman JA, Dauphas N, Alp EE, Hu M (2014) Iron isotope fractionation between metal and troilite: a new cooling speedometer for iron meteorites. Lunar Planet Sci Conf 45:2755
Krayenbuehl PA, Walczyk T, Schoenberg R, von Blanckenburg F, Schulthess G (2005) Hereditary hemochromatosis is reflected in the iron isotope composition of blood. Blood 105:3812–3816, doi:10.1182/blood-2004-07–2807
Kyser T, Lesher C, Walker D (1998) The effects of liquid immiscibility and thermal diffusion on oxygen isotopes in silicate liquids. Contrib Mineral Petrol 133:373–381
Lacks DJ, Goel G, Bopp IV CJ, Van Orman JA, Lesher CE, Lundstrom CC (2012) Isotope fractionation by thermal diffusion in silicate melts. Phys Rev Lett 108:065901
Lacan F, Francois R, Ji YC, Sherrell RM (2006) Cadmium isotopic composition in the ocean. Geochim Cosmochim Acta 70:5104–5118
Lacan F, Radic A, Jeandel C, Poitrasson F, Sarthou G, Pradoux C, Freydier, R (2008) Measurement of the isotopic composition of dissolved iron in the open ocean. Geophys Res Lett 35, doi: 10.1029/2008GL035841
Lacan F, Radic A, Labatut M, Jeandel C, Poitrasson F, Sarthou G, Pradoux C, Chmeleff J, Freydier, R (2010) High-precision determination of the isotopic composition of dissolved iron in iron depleted seawater by double-spike multicollector-ICPMS Anal Chem 55:7103–7111
Landry MR, Barber RT, Bidigare RR, Chai F, Coale KH, Dam HG, Lewis MR, Lindley ST, McCarthy JJ, Roman MR, Stoecker DK, Verity PG, White JR (1997) Iron and grazing constraints on primary production in the central equatorial Pacific: An EqPac synthesis. Limnol Oceanogr 42:405–418
Larner F (2016) Can we use high precision metal isotope analysis to improve our understanding of cancer? Anal Bioanal Chem 408:345–349
LeClaire A, Lidiard A (1956) LIII Correlation effects in diffusion in crystals. Phil Mag 1:518–527
Lee C-TA, Luffi P, Plank T, Dalton H, Leeman WP (2009) Constraints on the depths and temperatures of basaltic magma generation on Earth and other terrestrial planets using new thermobarometers for mafic magmas. Earth Planet Sci Lett 279:20–33
Lehmann B, Nägler TF, Holland HD, Wille M, Mao J, Pan J, Ma D, Dulski P (2007) Highly metalliferous carbonaceous shale and Early Cambrian seawater. Geology 35:403–406
Levasseur S, Frank M, Hein JR, Halliday AN (2004) The global variation in the iron isotope composition of marine hydrogenetic ferromanganese deposits: implications for seawater chemistry? Earth Planet Sci Lett 224:91–105
Li J, Agee CB (1996) Geochemistry of mantle–core differentiation at high pressure. Nature 381:686–689
Li X, Liu Y (2015) A theoretical model of isotopic fractionation by thermal diffusion and its implementation on silicate melts. Geochim Cosmochim Acta 154:18–27
Li WQ, Beard BL, Johnson CM (2015) Biologically recycled continental iron is a major component in banded iron formations. PNAS 112:8193–8198
Lin JF, Speziale S, Mao Z, Marquardt H (2013) Effects of the electronic spin transitions of iron in lower mantle minerals: implications for deep mantle geophysics and geochemistry. Rev Geophys 51:244–275

Liu Y, Spicuzza MJ, Craddock PR, Day J, Valley JW, Dauphas N, Taylor LA (2010) Oxygen and iron isotope constraints on near-surface fractionation effects and the composition of lunar mare basalt source regions. Geochim Cosmochim Acta 74:6249–6262

Liu S-A, Li D, Li S, Teng F-Z, Ke S, He Y, Lu Y (2014) High-precision copper and iron isotope analysis of igneous rock standards by MC-ICP-MS J Anal At Spectrom 29:122–133

Liu J, Dauphas N, Roskosz M, Hu MY, Yang H, Bi W, Zhao J, Alp EE, Hu JY, Lin J-F (2016) Iron isotopic fractionation between silicate mantle and metallic core at high pressure. Nat Commun: in press

Lovley DR, Stolz JF, Nord GL, Phillips EJP (1987) Anaerobic production of magnetite by a dissimilatory iron-reducing microorganism. Nature 330:252–254

Luck J-M, Othman DB, Albarède F (2005) Zn and Cu isotopic variations in chondrites and iron meteorites: early solar nebula reservoirs and parent-body processes. Geochim Cosmochim Acta 69:5351–5363

Lundstrom C (2009) Hypothesis for the origin of convergent margin granitoids and Earth's continental crust by thermal migration zone refining. Geochim Cosmochim Acta 73:5709–5729

Luo C, Mahowald N, Bond T, Chuang PY, Artaxo P, Siefert R, Chen Y, Schauer J (2008) Combustion iron distribution and deposition. Global Biogeochem Cycles, 22

Luz B, Barkan E, Bender ML, Thiemens MH, Boering KA (1999) Triple-isotope composition of atmospheric oxygen as a tracer of biosphere productivity. Nature 400:547–550

Lyons TW, Severmann S (2006) A critical look at iron paleoredox proxies: New insights from modern euxinic marine basins. Geochim Cosmochim Acta 70:5698–5722

Lyons TW, Reinhard CT, Planavsky NJ (2014) The rise of oxygen in Earth's early ocean and atmosphere. Nature 506:307–315

Mahowald NM, Baker AR, Bergametti G, Brooks N, Duce RA, Jickells TD, Kubilay N, Prospero JM, Tegen, I (2005) Atmospheric global dust cycle and iron inputs to the ocean. Global Biogeochem Cycles 19

Mandernack KW, Bazylinski DA, Shanks WC, Bullen TD (1999) Oxygen and iron isotope studies of magnetite produced by magnetotactic bacteria. Science 285:1892–1896

Majestic BJ, Anbar AD, Herckes, P (2009) Stable Isotopes as a Tool to Apportion Atmospheric Iron. Environ Sci Technol 43:4327–4333

Marcus RA (1965) On the theory of electron-transfer reactions. VI Unified treatment for homogeneous and electrode reactions. J Chem Phys:43:679–701

Marcus MA, Edwards KJ, Gueguen B, Fakra SC, Horn G, Jelinski NA, Rouxel O, Sorensen J, Toner BM (2015) Iron mineral structure, reactivity, isotopic composition in a South Pacific Gyre ferromanganese nodule over 4 Ma. Geochim Cosmochim Acta 171:61–79

Maréchal CN, Télouk P, Albarède F (1999) Precise analysis of copper and zinc isotopic compositions by plasma-source mass spectrometry. Chem Geol 156:251–273

Marhas KK, Amari S, Gyngard F, Zinner E, Gallino R (2008) Iron and nickel isotopic ratios in presolar SiC grains. Astrophys J 689:622

Marin-Carbonne J, Rollion-Bard C, Luais B (2011) In-situ measurements of iron isotopes by SIMS: MC-ICP-MS intercalibration and application to a magnetite crystal from the Gunflint chert. Chem Geol 285:50–61

Marin-Carbonne J, Rollion-Bard C, Bekker A, Rouxel O, Agangi A, Cavalazzi B, Wohlgemuth-Ueberwasser CC, Hofmann A, McKeegan KD (2014) Coupled Fe and S isotope variations in pyrite nodules from Archean shale. Earth Planet Sci Lett 392:67–79

Markl G, von Blanckenburg F, Wagner T (2006) Iron isotope fractionation during hydrothermal ore deposition and alteration. Geochim Cosmochim Acta 70:3011–3030

Martin JH (1990) Glacial-interglacial CO_2 change: The iron hypothesis. Paleoceanography 5:1–13

Martin JH, Fitzwater SE (1988) Iron-deficiency limits phytoplankton growth in the Northeast Pacific Subarctic. Nature 331:341–343

Martin JH, Coale KH, Johnson KS, Fitzwater SE, Gordon RM, Tanner SJ, Hunter CN, Elrod VA, Nowicki JL, Coley TL, others (1994) Testing the iron hypothesis in ecosystems of the equatorial Pacific Ocean. Nature 371:123–129

Martinez-Garcia A, Rosell-Mele A, Jaccard SL, Geibert W, Sigman DM, Haug GH (2011) Southern Ocean dust—climate coupling over the past four million years. Nature 476:312–315

Matsuhisa Y, Goldsmith JR, Clayton RN (1978) Mechanisms of hydrothermal crystallization of quartz at 250 °C and 15 kbar. Geochim Cosmochim Acta 42:173–182

Matthews A, Zhu XK, O'Nions, K (2001) Kinetic iron stable isotope fractionation between iron (-II) and (-III) complexes in solution. Earth Planet Sci Lett 192:81–92

Matthews A, Morgans-Bell HS, Emmanuel S, Jenkyns HC, Erel Y, Halicz L (2004) Controls on iron-isotope fractionation in organic-rich sediments (Kimmeridge Clay, Upper Jurassic, southern England). Geochim Cosmochim Acta 68:3107–3123

McCracken G, Love H (1960) Diffusion of lithium through tungsten. Phys Rev Lett 5:201

Mead C, Herckes P, Majestic BJ, Anbar AD (2013) Source apportionment of aerosol iron in the marine environment using iron isotope analysis. Geophys Res Lett 40:5722–5727

Millet M-A, Dauphas N (2014) Ultra-precise titanium stable isotope measurements by double-spike high resolution MC-ICP-MS J Anal At Spectrom 29:1444–1458

Millet M-A, Baker JA, Payne CE (2012) Ultra-precise stable Fe isotope measurements by high resolution multiple-collector inductively coupled plasma mass spectrometry with a ^{57}Fe–^{58}Fe double-spike. Chem Geol 304:18–25

Millet M-A, Dauphas N, Greber ND, Burton KW, Dale CW, Debret B, Pacpherson CG, Nowell GM, Williams HM (2016) Titanium stable isotope investigation of magmatic processes on the Earth and Moon. Earth Planet Sci Lett 449:197–205

Mills MM, Ridame C, Davey M, La Roche J, Geider RJ (2004) Iron and phosphorus co-limit nitrogen fixation in the eastern tropical North Atlantic. Nature 429:292–294

Mishra RK, Chaussidon M (2014) Fossil records of high level of ^{60}Fe in chondrules from unequilibrated chondrites. Earth Planet Sci Lett 398:90–100

Mishra R, Goswami J (2014) Fe–Ni and Al–Mg isotope records in UOC chondrules: Plausible stellar source of ^{60}Fe and other short-lived nuclides in the early Solar System. Geochim Cosmochim Acta 132:440–457

Mishra RK, Marhas KK (2016) Abundance of ^{60}Fe inferred from nanoSIMS study of QUE 97008 (L3. 05) chondrules. Earth Planet Sci Lett 436:71–81

Moeller K, Schoenberg R, Grenne T, Thorseth IH, Drost K, Pedersen RB (2014) Comparison of iron isotope variations in modern and Ordovician siliceous Fe oxyhydroxide deposits. Geochim Cosmochim Acta 126:422–440

Mojzsis SJ, Coath CD, Greenwood JP, McKeegan KD, Harrison TM (2003) Mass-independent isotope effects in Archean (2.5 to 3.8 Ga) sedimentary sulfides determined by ion microprobe analysis. Geochim Cosmochim Acta 67:1635–1658

Moore JK, Braucher, O (2008) Sedimentary and mineral dust sources of dissolved iron to the world ocean. Biogeosciences 5:631–656

Moore JK, Doney SC, Glover DM, Fung IY (2002) Iron cycling and nutrient-limitation patterns in surface waters of the World Ocean. Deep Sea Res Part II 49:463–507

Moynier F, Fujii T, Wang K, Foriel J (2013) Ab initio calculations of the Fe (II) and Fe (III) isotopic effects in citrates, nicotianamine, phytosiderophore, new Fe isotopic measurements in higher plants. C R Geosci 345:230–240

Mullane E, Russell S, Gounelle M (2005) Nebular and asteroidal modification of the iron isotope composition of chondritic components. Earth Planet Sci Lett 239:203–218

Mullen JG (1961) Isotope effect in intermetallic diffusion. Phys Rev 121:1649

Müller W, Shelley M, Miller P, Broude S (2009) Initial performance metrics of a new custom-designed ArF excimer LA-ICPMS system coupled to a two-volume laser-ablation cell. J Anal At Spectrom 24:209–214

Murray RW, Leinen M, Knowlton CW (2012) Links between iron input and opal deposition in the Pleistocene equatorial Pacific Ocean. Nature Geosci 5:270–274

Nebel O, Arculus R, Sossi P, Jenner F, Whan T (2013) Iron isotopic evidence for convective resurfacing of recycled arc-front mantle beneath back-arc basins. Geophys Res Lett 40:5849–5853

Nebel O, Campbell IH, Sossi PA, Van Kranendonk MJ (2014) Hafnium and iron isotopes in early Archean komatiites record a plume-driven convection cycle in the Hadean Earth. Earth Planet Sci Lett 397:111–120

Nebel O, Sossi P, Bénard A, Wille M, Vroon P, Arculus R (2015) Redox-variability and controls in subduction zones from an iron-isotope perspective. Earth Planet Sci Lett 432:142–151

Needham A, Porcelli D, Russell S (2009) An Fe isotope study of ordinary chondrites. Geochim Cosmochim Acta 73:7399–7413

Nie N, Dauphas N (2015) Iron isotope constraints on the photo-oxidation pathway to BIF formation. Lunar Planet Sci Conf 46: #2635

Nie N, Dauphas N, Greenwood R (2016) Iron and oxygen isotope fractionation during photo-oxidation. Oxygen and iron isotope fractionation during iron UV photo-oxidation: Implications for early Earth and Mars. Earth Planet Sci Lett, in press

Nielsen SG, Gannoun A, Marnham C, Burton KW, Halliday AN, Hein JR (2011) New age for ferromanganese crust 109D-C and implications for isotopic records of lead, neodymium, hafnium, thallium in the Pliocene Indian Ocean. Paleoceanography 26:PA2213

Nishizawa M, Yamamoto H, Ueno Y, Tsuruoka S, Shibuya T, Sawaki Y, Yamamoto S, Kon Y, Kitajima K, Komiya T (2010) Grain-scale iron isotopic distribution of pyrite from Precambrian shallow marine carbonate revealed by a femtosecond laser ablation multicollector ICP-MS technique: possible proxy for the redox state of ancient seawater. Geochim Cosmochim Acta 74:2760–2778

O'Connor C, Sharp BL, Evans P (2006) On-line additions of aqueous standards for calibration of laser ablation inductively coupled plasma mass spectrometry: theory and comparison of wet and dry plasma conditions. J Anal At Spectrom 21:556–565

Oeser M, Weyer S, Horn I, Schuth S (2014) High-precision Fe and Mg Isotope ratios of silicate reference glasses determined in situ by femtosecond LA-MC-ICP-MS and by solution nebulisation MC-ICP-MS Geostand Geoanal Res 38:311–328

Oeser M, Dohmen R, Horn I, Schuth S, Weyer S (2015) Processes and time scales of magmatic evolution as revealed by Fe–Mg chemical and isotopic zoning in natural olivines. Geochim Cosmochim Acta 154:130–150

Ono S, Eigenbrode JL, Pavlov AA, Kharecha P, Rumble D, Kasting JF, Freeman KH (2003) New insights into Archean sulfur cycle from mass-independent sulfur isotope records from the Hamersley Basin, Australia. Earth Planet Sci Lett 213:15–30

Othman DB, Luck J, Bodinier J, Arndt N, Albarède F (2006) Cu–Zn isotopic variations in the Earth's mantle. Geochim Cosmochim Acta 70:A46

Ottonello G, Zuccolini MV (2009) Ab-initio structure, energy and stable Fe isotope equilibrium fractionation of some geochemically relevant H–O–Fe complexes. Geochim Cosmochim Acta 73:6447–6469

Parekh P, Follows MJ, Boyle, E (2004) Modeling the global ocean iron cycle. Global Biogeochem Cycles 18, doi: 10.1029/2003GB002061

Pell E (1960) Diffusion of Li in Si at high *T* and the isotope effect. Phys Rev 119:1014

Percak-Dennett EM, Beard BL, Xu H, Konishi H, Johnson CM, Roden EE (2011) Iron isotope fractionation during microbial dissimilatory iron oxide reduction in simulated Archaean seawater. Geobiology 9:205–220

Perry EC, Tan FC, Morey GB (1973) Geology and stable isotope geochemistry of the Biwabik iron formation, Northern Minnesota. Economic Geology 68:1110–1125

Phillips GN, Law JDM (2000) Witwatersrand gold fields: geology, genesis, exploration. SEG Rev. 13:439–500

Planavsky N, Rouxel O, Bekker A, Shapiro R, Fralick P, Knudsen A (2009) Iron-oxidizing microbial ecosystems thrived in late Paleoproterozoic redox-stratified oceans. Earth Planet Sci Lett 286:230–242

Planavsky N, Rouxel OJ, Bekker A, Hofmann A, Little CTS, Lyons TW (2012) Iron isotope composition of some Archean and Proterozoic iron formations. Geochim Cosmochim Acta 80:158–169

Planavsky NJ, Asael D, Hofman A, Reinhard CT, Lalonde SV, Knudsen A, Wang X, Ossa FO, Pecoits E, Smith AJ, Beukes N (2014) Evidence for oxygenic photosynthesis half a billiion years before the Great Oxidation Event. Nat Geosci 7:283–286

Poigner H, Wilhelms-Dick D, Abele D, Staubwasser M, Henkel S (2015) Iron assimilation by the clam *Laternula elliptica*: Do stable isotopes (δ^{56}Fe) help to decipher the sources? Chemosphere 134:294–300

Poitrasson F, Freydier R (2005) Heavy iron isotope composition of granites determined by high resolution MC-ICP-MS Chem Geol 222:132–147

Poitrasson F, Halliday AN, Lee D-C, Levasseur S, Teutsch N (2004) Iron isotope differences between Earth, Moon, Mars and Vesta as possible records of contrasted accretion mechanisms. Earth Planet Sci Lett 223:253–266

Poitrasson F, Viers J, Martin F, Braun, J-J (2008) Limited iron isotope variations in recent lateritic soils from Nsimi, Cameroon: Implications for the global Fe geochemical cycle. Chem Geol 253:54–63

Poitrasson F, Roskosz M, Corgne A (2009) No iron isotope fractionation between molten alloys and silicate melt to 2000 degrees C and 7.7 GPa: Experimental evidence and implications for planetary differentiation and accretion. Earth Planet Sci Lett 278:376–385

Poitrasson F, Delpech G, Grégoire M (2013) On the iron isotope heterogeneity of lithospheric mantle xenoliths: implications for mantle metasomatism, the origin of basalts and the iron isotope composition of the Earth. Contrib Mineral Petrol 165:1243–1258

Poitrasson F, Vieira LC, Seyler P, dos Santos Pinheiro GM, Mulholland DS, Bonnet, M-P, Martinez, J-M, Lima BA, Boaventura GR, Chmeleff J, others (2014) Iron isotope composition of the bulk waters and sediments from the Amazon River Basin. Chem Geol 377:1–11

Polyakov VB (2009) Equilibrium iron isotope fractionation at core-mantle boundary conditions. Science 323:912–914

Polyakov VB, Mineev SD (2000) The use of Mössbauer spectroscopy in stable isotope geochemistry. Geochim Cosmochim Acta 64:849–865

Polyakov VB, Soultanov DM (2011) New data on equilibrium iron isotope fractionation among sulfides: Constraints on mechanisms of sulfide formation in hydrothermal and igneous systems. Geochim Cosmochim Acta 75:1957–1974

Polyakov V, Clayton R, Horita J, Mineev S (2007) Equilibrium iron isotope fractionation factors of minerals: reevaluation from the data of nuclear inelastic resonant X-ray scattering and Mössbauer spectroscopy. Geochim Cosmochim Acta 71:3833–3846

Poulton SW, Fralick PW, Canfield DE (2004) The transition to a sulfidic ocean ~1.84 billion years ago. Nature 431:173–177

Poulton SW, Fralick PW, Canfield DE (2010) Spatial variability in oceanic redox structure 1.8 billion years ago. Nat Geosci 3:486–490

Quitté G, Markowski A, Latkoczy C, Gabriel A, Pack A (2010) Iron–60 Heterogeneity and Incomplete Isotope Mixing in the Early Solar System. Astrophys J 720:1215–1224

Radic A, Lacan F, Murray JW (2011) Iron isotopes in the seawater of the equatorial Pacific Ocean: New constraints for the oceanic iron cycle. Earth Planet Sci Lett 306:1–10
Raiswell R, Canfield DE (1998) Sources of iron for pyrite formation in marine sediments. Am J Sci 298:219–245
Raiswell R, Tranter M, Benning LG, Siegert M, De'ath R, Huybrechts P, Payne T (2006) Contributions from glacially derived sediment to the global iron (oxyhydr)oxide cycle: Implications for iron delivery to the oceans. Geochim Cosmochim Acta 70:2765–2780
Rasmussen B, Meier DB, Krapez B, Muhling JR (2013) Iron silicate microgranules as precursor sediments to 2.5-billion-year-old banded iron formations. Geology 41:435–438
Rasmussen B, Krapez B, Muhling JR, Suvorova A (2015) Precipitation of iron silicate nanoparticles in early Precambrian oceans marks Earth's first iron age. Geology 43:303–306
Reddy TR, Frierdich AJ, Beard BL, Johnson CM (2015) The effect of pH on stable iron isotope exchange and fractionation between aqueous Fe(II) and goethite. Chem Geol 397:118–127
Reid RT, Livet DH, Faulkner DJ, Butler, A (1993) A siderophore from a marine bacterium with an exceptional ferric ion affinity constant. Nature 366:455–458
Resing JA, Sedwick PN, German CR, Jenkins WJ, Moffett JW, Sohst BM, Tagliabue, A (2015) Basin-scale transport of hydrothermal dissolved metals across the South Pacific Ocean. Nature 523:200–203
Revels BN, Ohnemus DC, Lam PJ, Conway TM, John SG (2014) The isotope signature and distribution of particulate iron in the north Atlantic ocean. Deep Sea Research Part II: 116:321-31
Revels BN, Zhang R, Adkins JF, John SG (2015) Fractionation of iron isotopes during leaching of natural particles by acidic and circumneutral leaches and development of an optimal leach for marine particulate iron isotopes. Geochim Cosmochim Acta 166:92–104
Richter FM (2004) Timescales determining the degree of kinetic isotope fractionation by evaporation and condensation. Geochim Cosmochim Acta 68:4971–4992
Richter FM, Davis AM, Ebel DS, Hashimoto A (2002) Elemental and isotopic fractionation of Type B calcium-, aluminum-rich inclusions: experiments, theoretical considerations, constraints on their thermal evolution. Geochim Cosmochim Acta 66:521–540
Richter FM, Janney PE, Mendybaev RA, Davis AM, Wadhwa M (2007) Elemental and isotopic fractionation of Type B CAI-like liquids by evaporation. Geochim Cosmochim Acta 71:5544–5564
Richter FM, Watson EB, Mendybaev RA, Teng F-Z, Janney PE (2008) Magnesium isotope fractionation in silicate melts by chemical and thermal diffusion. Geochim Cosmochim Acta 72:206–220
Richter FM, Dauphas N, Teng F-Z (2009a) Non-traditional fractionation of non-traditional isotopes: evaporation, chemical diffusion and Soret diffusion. Chem Geol 258:92–103
Richter FM, Watson EB, Mendybaev R, Dauphas N, Georg B, Watkins J, Valley J (2009b) Isotopic fractionation of the major elements of molten basalt by chemical and thermal diffusion. Geochim Cosmochim Acta 73:4250–4263
Richter FM, Huss GR, Mendybaev RA (2014a) Iron and nickel isotopic fractionation across metal grains from three CBb meteorites. Lunar Planet Sci Conf 45:1346
Richter FM, Watson EB, Chaussidon M, Mendybaev R, Christensen JN, Qiu L (2014b) Isotope fractionation of Li and K in silicate liquids by Soret diffusion. Geochim Cosmochim Acta 138:136–145
Robb LJ, Meyer FM (1990). The nature of the Witwatersrand hinterland; conjectures on the source area problem. Econ Geol 85:511–536
Roden E (2004) Analysis of long-term bacterial vs. chemical Fe(III) oxide reduction kinetics. Geochim Cosmochim Acta 68:3205–3216
Rodushkin I, Stenberg A, Andrén H, Malinovsky D, Baxter DC (2004) Isotopic fractionation during diffusion of transition metal ions in solution. Anal CHem 76:2148–2151
Roskosz M, Luais B, Watson HC, Toplis MJ, Alexander CMD, Mysen BO (2006) Experimental quantification of the fractionation of Fe isotopes during metal segregation from a silicate melt. Earth Planet Sci Lett 248:851–867
Roskosz M, Sio CK, Dauphas N, Bi W, Tissot FL, Hu MY, Zhao J, Alp EE (2015) Spinel–olivine–pyroxene equilibrium iron isotopic fractionation and applications to natural peridotites. Geochim Cosmochim Acta 169:184–199
Rouxel OJ, Auro M (2010) Iron isotope variations in coastal seawater determined by multicollector ICP-MS Geostand Geoanal Res 34:135–144
Rouxel O, Dobbek N, Ludden J, Fouquet Y (2003) Iron isotope fractionation during oceanic crust alteration. Chem Geol 202:155–182
Rouxel O, Fouquet Y, Ludden JN (2004) Subsurface processes at the Lucky Strike hydrothermal field, Mid-Atlantic Ridge: Evidence from sulfur, selenium, iron isotopes. Geochim Cosmochim Acta 68:2295–2311
Rouxel OJ, Bekker A, Edwards KJ (2005) Iron isotope constraints on the Archean and Paleoproterozoic ocean redox state. Science 307:1088–1091
Rouxel OJ, Bekker A, Edward KJ (2006) Response to comment on "Iron isotope constraints on the archean and paleoproterozoic ocean redox state". Science 311, doi:Doi 10.1126/Science.1118420

Rouxel O, Sholkovitz E, Charette M, Edwards KJ (2008a) Iron isotope fractionation in subterranean estuaries. Geochim Cosmochim Acta 72:3413–3430

Rouxel O, Shanks WC, Bach W, Edwards KJ (2008b) Integrated Fe- and S-isotope study of seafloor hydrothermal vents at East Pacific Rise 9–10°N Chem Geol 252:214–227

Rouxel O, Toner B, Manganini S, German C (2016) Geochemistry and iron isotope systematics of hydrothermal plume fall-out at EPR9°50'N Chem. Geol. 441:212–234

Roy M, Martin JB, Cherrier J, Cable JE, Smith CG (2010) Influence of sea level rise on iron diagenesis in an east Florida subterranean estuary. Geochim Cosmochim Acta 74:5560–5573

Roy M, Rouxel O, Martin JB, Cable JE (2012) Iron isotope fractionation in a sulfide-bearing subterranean estuary and its potential influence on oceanic Fe isotope flux. Chem Geol, 300–301:133–142

Rubie DC, Frost DJ, Mann U, Asahara Y, Nimmo F, Tsuno K, Kegler P, Holzheid A, Palme H (2011) Heterogeneous accretion, composition and core–mantle differentiation of the Earth. Earth Planet Sci Lett 301:31–42

Rudge JF, Reynolds BC, Bourdon B (2009) The double-spike toolbox. Chem Geol 265:420–431

Rustad JR, Dixon DA (2009) Prediction of iron-isotope fractionation between hematite (α–Fe_2O_3) and ferric and ferrous iron in aqueous solution from density functional theory. J Phys Chem A 113:12249–12255

Rustad JR, Yin Q-Z (2009) Iron isotope fractionation in the Earth's lower mantle. Nat Geosci 2:514–518

Saito, MA, Noble AE, Tagliabue A, Goepfert TJ, Lamborg CH, Jenkins WJ (2013) Slow-spreading submarine ridges in the South Atlantic as a significant oceanic iron source. Nat Geosci 6:775–779

Saunier G, Pokrovski GS, Poitrasson F (2011) First experimental determination of iron isotope fractionation between hematite and aqueous solution at hydrothermal conditions. Geochim Cosmochim Acta 75:6629–6654

Schauble EA (2004) Applying stable isotope fractionation theory to new systems. Rev Mineral Geochem 55:65–111

Schauble E, Rossman G, Taylor H (2001) Theoretical estimates of equilibrium Fe-isotope fractionations from vibrational spectroscopy. Geochim Cosmochim Acta 65:2487–2497

Schoenberg R, von Blanckenburg F (2005) An assessment of the accuracy of stable Fe isotope ratio measurements on samples with organic and inorganic matrices by high-resolution multicollector ICP-MS Inter J Mass Spectrom 242:257–272

Schoenberg R, von Blanckenburg F (2006) Modes of planetary-scale Fe isotope fractionation. Earth Planet Sci Lett 252:342–359

Scholz F, Severmann S, McManus J, Hensen C (2014) Beyond the Black Sea paradigm: The sedimentary fingerprint of an open-marine iron shuttle. Geochim Cosmochim Acta 127:368–380

Schuessler JA, Schoenberg R, Behrens H, von Blanckenburg F (2007) The experimental calibration of the iron isotope fractionation factor between pyrrhotite and peralkaline rhyolitic melt. Geochim Cosmochim Acta 71:417–433

Schuessler JA, Schoenberg R, Sigmarsson O (2009) Iron and lithium isotope systematics of the Hekla volcano, Iceland—evidence for Fe isotope fractionation during magma differentiation. Chem Geol 258:78–91

Schuler D, Baeuerlein E (1996) Iron-limited growth and kinetics of iron uptake in Magnetospirilum gryphiswaldense. Arch Microbiol 166:301–307

Schuth S, Hurrass J, Muenker C, Mansfeldt, T (2015) Redox-dependent fractionation of iron isotopes in suspensions of a groundwater-influenced soil. Chem Geol 392:74–86

Scott C, Lyons TW, Bekker A, Shen Y, Poulton SW, Chu X, Anbar AD (2008) Tracing the stepwise oxygenation of the Proterozoic ocean. Nature 452:456–459

Sedaghatpour F, Teng F-Z, Liu Y, Sears DW, Taylor LA (2013) Magnesium isotopic composition of the Moon. Geochim Cosmochim Acta 120:1–16

Sedwick PN, Church TM, Bowie AR, Marsay CM, Ussher SJ, Achilles KM, Lethaby PJ, Johnson RJ, Sarin MM, McGillicuddy DJ (2005) Iron in the Sargasso Sea (Bermuda Atlantic Time-series Study region) during summer: Eolian imprint, spatiotemporal variability, ecological implications. Global Biogeochem Cycles 19, doi: 10.1029/2004GB002445

Severmann S, Johnson CM, Beard BL, German CR, Edmonds HN, Chiba H, Green, DRH (2004) The effect of plume processes on the Fe isotope composition of hydrothermally derived Fe in the deep ocean as inferred from the Rainbow vent site, Mid-Atlantic Ridge, 36°14' N Earth Planet Sci Lett 225:63–76

Severmann S, Johnson CM, Beard BL, McManus, J (2006) The effect of early diagenesis on the Fe isotope compositions of porewaters and authigenic minerals in continental margin sediments. Geochim Cosmochim Acta 70:2006–2022

Severmann S, Lyons TW, Anbar A, McManus J, Gordon G (2008) Modern iron isotope perspective on the benthic iron shuttle and the redox evolution of ancient oceans. Geology 36:487–490

Severmann S, McManus J, Berelson WM, Hammond DE (2010) The continental shelf benthic iron flux and its isotope composition. Geochim Cosmochim Acta 74:3984–4004

Shahar A, Young ED, Manning CE (2008) Equilibrium high-temperature Fe isotope fractionation between fayalite and magnetite: An experimental calibration. Earth Planet Sci Lett 268:330–338

Shahar A, Hillgren V, Horan M, Mesa-Garcia J, Kaufman L, Mock T (2015) Sulfur-controlled iron isotope fractionation experiments of core formation in planetary bodies. Geochim Cosmochim Acta 150:253–264

Shahar A, Schauble EA, Caracas R, Gleason AE, Reagan MM, Xiao Y, Shu J, Mao W (2016) Pressure-dependent isotopic composition of iron alloys. Science 352:580–582

Sharma M, Polizzotto M, Anbar AD (2001) Iron isotopes in hot springs along the Juan de Fuca Ridge. Earth Planet Sci Lett 194:39–51

Siebert C, Nagler TF, von Blanckenburg F, Kramers JD (2003) Molybdenum isotope records as a potential new proxy for paleoceanography. Earth Planet Sci Lett 211:159–171

Siebert J, Badro J, Antonangeli D, Ryerson FJ (2013) Terrestrial accretion under oxidizing conditions. Science 339:1194–1197

Simmons SL, Sievert SM, Frankel RB, Bazylinski DA, Edwards KJ (2004) Spatiotemporal distribution of marine magnetotactic bacteria in a seasonally stratified coastal salt pond. Appl Environ Microbiol 70:6230–6239

Sio CKI, Dauphas N (2016) Thermal histories of magmatic bodies by Monte Carlo inversion of Mg-–Fe isotopic profiles in olivine. Geology, in press.

Sio CKI, Dauphas N, Teng F-Z, Chaussidon M, Helz RT, Roskosz M (2013) Discerning crystal growth from diffusion profiles in zoned olivine by in situ Mg–Fe isotopic analyses. Geochim Cosmochim Acta 123:302–321

Sivan O, Adler M, Pearson A, Gelman F, Bar-Or I, John SG, Eckert, W (2011) Geochemical evidence for iron-mediated anaerobic oxidation of methane. Limnol Oceanogr 56:1536–1544

Skulan JL, Beard BL, Johnson CM (2002) Kinetic and equilibrium Fe isotope fractionation between aqueous Fe (III) and hematite. Geochim Cosmochim Acta 66:2995–3015

Snow JE, Dick HJB (1995) Pervasive magnesium loss by marine weathering of peridotite. Geochim Cosmochim Acta 59:4219–4235

Sobolev AV, Hofmann AW, Kuzmin DV, Yaxley GM, Arndt NT, Chung S-L, Danyushevsky LV, Elliott T, Frey FA, Garcia MO (2007) The amount of recycled crust in sources of mantle-derived melts. Science 316:412–417

Song L, Liu C, Wang Z, Zhu X, Teng Y, Wang J, Tang, S Li J, LIANG, L (2011) Iron isotope compositions of natural river and lake samples in the karst area, Guizhou Province, Southwest China. Acta Geologica Sinica - English Edition 85:712–722

Sossi PA, Foden JD, Halverson GP (2012) Redox-controlled iron isotope fractionation during magmatic differentiation: an example from the Red Hill intrusion, S Tasmania. Contrib Mineral Petrol 164:757–772

Sossi PA, Halverson GP, Nebel O, Eggins SM (2015) Combined separation of Cu, Fe and Zn from rock matrices and improved analytical protocols for stable isotope determination. Geostand Geoanal Res 39:129–149

Sossi PA, O'Neill HSC (2016) The effect of bonding environment on iron isotope fractionation between minerals at high temperature. Geochim Cosmochim Acta, in press

Sossi PA, Nebel O, Anand M, Poitrasson F (2016) On the iron isotope composition of Mars and volatile depletion in the terrestrial planets. Earth Planet Sci Lett 449:360–371

Spring S, Amann R, Ludwig W, Schleifer K, Petersen N (1993) Dominating role of an unusual magnetotactic bacteria. System Appl Microbiol 15:116–122

Staudigel H, Hart SR (1983) Alteration of basaltic glasses: Mechanisms and significance for the oceanic crust-seawater budget. Geochim Cosmochim Acta 47:337–350

Steele RC, Elliott T, Coath CD, Regelous M (2011) Confirmation of mass-independent Ni isotopic variability in iron meteorites. Geochim Cosmochim Acta 75:7906–7925

Steinhoefel G, Horn I, von Blanckenburg F (2009a) Matrix-independent Fe isotope ratio determination in silicates using UV femtosecond laser ablation. Chem Geol 268:67–73

Steinhoefel G, Horn I, von Blanckenburg F (2009b) Micro-scale tracing of Fe and Si isotope signatures in banded iron formation using femtosecond laser ablation. Geochim Cosmochim Acta 73:5343–5360

Steinhoefel G, von Blanckenburg F, Horn I, Konhauser KO, Beukes NJ, Gutzmer J (2010) Deciphering formation processes of banded iron formations from the Transvaal and the Hamersley successions by combined Si and Fe isotope analysis using UV femtosecond laser ablation. Geochim Cosmochim Acta 74:2677–2696

Strelow F (1980) Improved separation of iron from copper and other elements by anion-exchange chromatography on a 4% cross-linked resin with high concentrations of hydrochloric acid. Talanta 27:727–732

Sturhahn W, Jackson JM (2007) Geophysical applications of nuclear resonant spectroscopy. Geol Soc Am Spec Pap 421:157–174

Sumner DY (1997) Carbonate precipitation and oxygen stratification in Late Archean seawater as deduced from facies and stratigraphy of the Gamohaan and Frisco formations, Transvaal Supergroup, South Africa. Am J Sci 297:455–487

Swanner ED, Wu WF, Schoenberg R, Byrne J, Michel FM, Pan YX, Kappler A (2015) Fractionation of Fe isotopes during Fe(II) oxidation by a marine photoferrotroph is controlled by the formation of organic Fe-complexes and colloidal Fe fractions. Geochim Cosmochim Acta 165:44–61

Syverson DD, Borrok DM, Seyfried WE (2013) Experimental determination of equilibrium Fe isotopic fractionation between pyrite and dissolved Fe under hydrothermal conditions. Geochim Cosmochim Acta 122:170–183

Syverson DD, Pester NJ, Craddock PR, Seyfried WE (2014) Fe isotope fractionation during phase separation in the NaCl–H_2O system: An experimental study with implications for seafloor hydrothermal vents. Earth Planet Sci Lett 406:223–232

Tagliabue A, Bopp L, Dutay JC, Bowie AR, Chever F, Jean-Baptiste P, Bucciarelli E, Lannuzel D, Remenyi T, Sarthou G, Aumont O (2010) Hydrothermal contribution to the oceanic dissolved iron inventory. Nat Geosci 3:252–256

Tagliabue A, Aumont O, Bopp, L (2014) The impact of different external sources of iron on the global carbon cycle. Geophys Res Lett 41:920–926

Tahata M, Sawaki Y, Yoshiya K, Nishizawa M, Komiya T, Hirata T, Yoshida N, Maruyama S, Windley BF (2015) The marine environments encompassing the Neoproterozoic glaciations: Evidence from C, Sr and Fe isotope ratios in the Hecla Hoek Supergroup in Svalbard. Precambrian Res 263:19–42

Tang H, Dauphas N (2012) Abundance, distribution, origin of ^{60}Fe in the solar protoplanetary disk. Earth Planet Sci Lett 359:248–263

Tang H, Dauphas N (2014) ^{60}Fe–^{60}Ni chronology of core formation on Mars. Earth Planet Sci Lett 390:264–274

Tang H, Dauphas N (2015) Low ^{60}Fe abundance in Semarkona and Sahara 99555. Astrophys J 802:22

Tangalos GE, Beard BL, Johnson CM, Alpers CN, Shelobolina ES, Xu H, Konishi H, Roden EE (2010) Microbial production of isotopically light iron(II) in a modern chemically precipitated sediment and implications for isotopic variations in ancient rocks. Geobiology 8:197–208

Telus M, Dauphas N, Moynier F, Tissot FL, Teng F-Z, Nabelek PI, Craddock PR, Groat LA (2012) Iron, zinc, magnesium and uranium isotopic fractionation during continental crust differentiation: The tale from migmatites, granitoids, pegmatites. Geochim Cosmochim Acta 97:247–265

Teng FZ, Dauphas N, Helz RT (2008) Iron isotope fractionation during magmatic differentiation in Kilauea Iki Lava Lake. Science 320:1620–1622

Teng F-Z, Dauphas N, Helz RT, Gao S, Huang S (2011) Diffusion-driven magnesium and iron isotope fractionation in Hawaiian olivine. Earth Planet Sci Lett 308:317–324

Teng F-Z, Dauphas N, Huang S, Marty B (2013) Iron isotopic systematics of oceanic basalts. Geochim Cosmochim Acta 107:12–26

Toner BM, Fakra SC, Manganini SJ, Santelli CM, Marcus MA, Moffett J, Rouxel O, German CR, Edwards KJ (2009) Preservation of iron(II) by carbon-rich matrices in a hydrothermal plume. Nat Geosci 2:197–201

Toner BM, Rouxel OJ, Santelli CM, Bach W, Edwards KJ (2016) Iron transformation pathways and redox micro-environments in seafloor sulfide-mineral deposits: spatially resolved Fe XAS and $\delta^{57/54}$Fe observations. Front Microbiol 7:648

Toplis M (2005) The thermodynamics of iron and magnesium partitioning between olivine and liquid: criteria for assessing and predicting equilibrium in natural and experimental systems. Contrib Mineral Petrol 149:22–39

Trappitsch R, Stephan T, Davis AM, Pellin MJ, Rost D, Savina MR, Kelly CH, Dauphas N (2016) Simultansous analysis of iron and nickel isotopes in presolar SiC grains with CHILI Lunar Planet Sci Conf 47:#3025

Tsikos H, Matthews A, Erel Y, Moore JM (2010) Iron isotopes constrain biogeochemical redox cycling of iron and manganese in a Palaeoproterozoic stratified basin. Earth Planet Sci Lett 298:125–134

Urey HC (1947) The thermodynamic properties of isotopic substances. J Chem Soc (Resumed):562–581

Urey HC, Craig H (1953) The composition of the stone meteorites and the origin of the meteorites. Geochim Cosmochim Acta 4:36–82

Van Heghe L, Engstrom E, Rodushkin I, Cloquet C, Vanhaecke F (2012) Isotopic analysis of the metabolically relevant transition metals Cu, Fe and Zn in human blood from vegetarians and omnivores using multi-collector ICP-mass spectrometry. J Anal At Spectrom 27:1327–1334

Van Heghe L, Delanghe J, Van Vlierberghe H, Vanhaecke F (2013) The relationship between the iron isotopic composition of human whole blood and iron status parameters. Metallomics 5:1503–1509

Van Heghe L, Deltombe O, Delanghe J, Depypere H, Vanhaecke F (2014) The influence of menstrual blood loss and age on the isotopic composition of Cu, Fe and Zn in human whole blood. J Anal At Spectrom 29:478–482

Vanhaecke F, Costas-Rodriguez M (2015) What's up doc?—High-precision isotopic analysis of essential metals in biofluids for medical diagnosis. Spectroscopy Europe 27:11–14

Vargas M, Kashefi K, BluntHarris EL, Lovley DR (1998) Microbiological evidence for Fe(III) reduction on early Earth. Nature 395:65–67

Völkening J, Papanastassiou D (1989) Iron isotope anomalies. Astrophys J 347:L43-L46

von Blanckenburg F, Marnberti M, Schoenberg R, Kamber BS, Webb GE (2008) The iron isotope composition of microbial carbonate. Chem Geol 249:113–128

von Blanckenburg F, von Wiren N, Guelke M, Weiss DJ, Bullen TD (2009) Fractionation of metal stable isotopes by higher plants. Elements 5:375–380

von Blanckenburg F, Noordmann J, Guelke-Stelling M (2013) The iron stable isotope fingerprint of the human diet. J Ag Food Chem 61:11893–11899

von Blanckenburg F, Oelze M, Schmid DG, van Zuilen K, Gschwind HP, Slade AJ, Stitah S, Kaufmann D, Swart P (2014) An iron stable isotope comparison between human erythrocytes and plasma. Metallomics 6:2052–2061

Von Damm KL (1988) Systematics of and postulated controls on submarine hydrothermal solution chemistry. J Geophys Res-Solid Earth and Planets 93:4551–4561

Von Damm KL, Oosting SE, Kozlowski R, Buttermore LG, Colodner DC, Edmonds HN, Edmond JM, Grebmeier JM (1995) Evolution of East Pacific Rise hydrothermal vent fluids following a volcanic eruption. Nature 375:47–50

Waeles M, Baker AR, Jickells T, Hoogewerff, J (2007) Global dust teleconnections: aerosol iron solubility and stable isotope composition. Environ Chem 4:233–237

Walczyk T, vonBlanckenburg F (2002) Natural iron isotope variations in human blood. Science 295:2065–2066

Walczyk T, von Blanckenburg F (2005) Deciphering the iron isotope message of the human body. Inter J Mass Spectrom 242:117–134

Wang J, Davis A, Clayton R, Mayeda T (1994) Kinetic isotopic fractionation during the evaporation of the iron oxide from liquid state. Lunar Planet Sci Conf 25:1459

Wang K, Moynier F, Dauphas N, Barrat J-A, Craddock P, Sio CK (2012) Iron isotope fractionation in planetary crusts. Geochim Cosmochim Acta 89:31–45

Watkins JM, DePaolo DJ, Ryerson FJ, Peterson BT (2011) Influence of liquid structure on diffusive isotope separation in molten silicates and aqueous solutions. Geochim Cosmochim Acta 75:3103–3118

Watson EB, Müller T (2009) Non-equilibrium isotopic and elemental fractionation during diffusion-controlled crystal growth under static and dynamic conditions. Chem Geol 267:111–124

Wawryk CM, Foden JD (2015) Fe-isotope fractionation in magmatic-hydrothermal mineral deposits: a case study from the Renison Sn–W deposit, Tasmania. Geochim Cosmochim Acta 150:285–298

Weis F, Troll VR, Jonsson E, Hogdahl K, Barker A, Harris C, Millet M-A, Nilsson KP (2013) Iron and oxygen isotope systematics of apatite-iron oxide ores in central Sweden. *In:* E Jonsson (Ed.) Mineral Deposit Research for a High-Tech World pp. 1675–1678

Welch SA, Beard BL, Johnson CM, Braterman PS (2003) Kinetic and equilibrium Fe isotope fractionation between aqueous Fe(II) and Fe(III). Geochim Cosmochim Acta 67:4231–4250

Weyer S, Ionov DA (2007) Partial melting and melt percolation in the mantle: The message from Fe isotopes. Earth Planet Sci Lett 259:119–133

Weyer S, Schwieters J (2003) High precision Fe isotope measurements with high mass resolution MC-ICPMS Inter J Mass Spectrom 226:355–368

Weyer S, Anbar AD, Brey GP, Münker C, Mezger K, Woodland AB (2005) Iron isotope fractionation during planetary differentiation. Earth Planet Sci Lett 240:251–264

Wheat CG, Mottl MJ (2004) Geochemical fluxes through mid-ocean ridge flanks. *In:* Hydrogeology of the Oceanic Lithosphere. Davis EE, Elderfield H, (eds). Cambridge University Press, Cambridge

Whitehouse MJ, Fedo CM (2007) Microscale heterogeneity of Fe isotopes in >3.71 Ga banded iron formation from the Isua Greenstone Belt, southwest Greenland. Geology 35:719–722

Widdel F, Schnell S, Heising S, Ehrenreich A, Assmus B, Schink B (1993) Ferrous iron oxidation by anoxygenic phototrophic bacteria. Nature 362:834–836, doi:10.1038/362834a0

Wiederhold JG, Kraemer SM, Teutsch N, Borer PM, Halliday A, Kretzschmar, R (2006) Iron isotope fractionation during proton-promoted, ligand-controlled, reductive dissolution of goethite. Environ Sci Technol 40:3787–3793

Wiederhold JG, Teutsch N, Kraemer SM, Halliday A, Kretzschmar, R (2007a) Iron isotope fractionation in oxic soils by mineral weathering and podzolization. Geochim Cosmochim Acta 71:5821–5833

Wiederhold JG, Teutsch N, Kraemer SM, Halliday A, Kretzschmar, R (2007b) Iron isotope fractionation during pedogenesis in redoximorphic soils. Soil Sci Soc Am J 71:1840–1850

Wiesli RA, Beard BL, Taylor LA, Johnson CM (2003) Space weathering processes on airless bodies: Fe isotope fractionation in the lunar regolith. Earth Planet Sci Lett 216:457–465

Wiesli RA, Beard BL, Johnson CM (2004) Experimental determination of Fe isotope fractionation between aqueous Fe (II), siderite and "green rust" in abiotic systems. Chem Geol 211:343–362

Wiesli RA, Beard BL, Braterman PS, Johnson CM, Saha SK, Sinha MP (2007) Iron isotope fractionation between liquid and vapor phases of iron pentacarbonyl. Talanta 71:90–96

Wijsman JWM, Middelburg JJ, Herman PMJ, Bottcher ME, Heip CHR (2001) Sulfur and iron speciation in surface sediments along the northwestern margin of the Black Sea. Mar Chem 74:261–278

Williams HM, Bizimis M (2014) Iron isotope tracing of mantle heterogeneity within the source regions of oceanic basalts. Earth Planet Sci Lett 404:396–407

Williams HM, McCammon CA, Peslier AH, Halliday AN, Teutsch N, Levasseur S, Burg J-P (2004) Iron isotope fractionation and the oxygen fugacity of the mantle. Science 304:1656–1659

Williams HM, Peslier AH, McCammon C, Halliday AN, Levasseur S, Teutsch N, Burg JP (2005) Systematic iron isotope variations in mantle rocks and minerals: The effects of partial melting and oxygen fugacity. Earth Planet Sci Lett 235:435–452

Williams HM, Wood BJ, Wade J, Frost DJ, Tuff J (2012) Isotopic evidence for internal oxidation of the Earth's mantle during accretion. Earth Planet Sci Lett 321:54–63

Williams KB, Krawczynski MJ, Nie NX, Dauphas N, Couvy H, Hu MY, Alp EE (2016) The role of differentiation processes in mare basalt iron isotope signatures. Lunar Planet Sci Conf 47:2779

Windom HL, Moore WS, Niencheski, LFH, Jahrike RA (2006) Submarine groundwater discharge: A large, previously unrecognized source of dissolved iron to the South Atlantic Ocean. Mar Chem 102:252–266

Wu LL, Beard BL, Roden EE, Johnson CM (2009) Influence of pH and dissolved Si on Fe isotope fractionation during dissimilatory microbial reduction of hematite. Geochim Cosmochim Acta 73:5584–5599

Wu L, Beard BL, Roden EE, Kennedy CB, Johnson CM (2010) Stable Fe isotope fractionations produced by aqueous Fe(II)–hematite surface interactions. Geochim Cosmochim Acta 74:4249–4265

Wu L, Beard BL, Roden EE, Johnson CM (2011) Stable iron isotope fractionation between aqueous Fe (II) and hydrous ferric oxide. Environ Sci Technol 45:1847–1852

Wu L, Percak-Dennett EM, Beard BL, Roden EE, Johnson CM (2012a) Stable iron isotope fractionation between aqueous Fe (II) and model Archean ocean Fe–Si coprecipitates and implications for iron isotope variations in the ancient rock record. Geochim Cosmochim Acta 84:14–28

Wu L, Druschel G, Findlay A, Beard BL, Johnson CM (2012b) Experimental determination of iron isotope fractionations among FeS_{aq}–Mackinawite at low temperatures: Implications for the rock record. Geochim Cosmochim Acta 89:46–61

Yamaguchi KE, Johnson CM, Beard BL, Ohmoto H (2005) Biogeochemical cycling of iron in the Archean-Paleoproterozoic Earth: Constraints from iron isotope variations in sedimentary rocks from the Kaapvaal and Pilbara Cratons. Chem Geol 218:135–169

Yamaguchi KE, Johnson CM, Beard BL, Beukes NJ, Gutzmer J, Ohmoto H (2007). Isotopic evidence for iron mobilization during Paleoproterozoic lateritization of the Hekpoort paleosol profile from Gaborone, Botswana. Earth Planet Sci Lett 256:577–587

Yoshiya K, Nishizawa M, Sawaki Y, Ueno Y, Komiya T, Yamada K, Yoshida N, Hirata T, Wada H, Maruyama S (2012) In situ iron isotope analyses of pyrite and organic carbon isotope ratios in the Fortescue Group: Metabolic variations of a Late Archean ecosystem. Precambrian Res 212:169–193

Young ED, Galy A, Nagahara H (2002) Kinetic and equilibrium mass-dependent isotope fractionation laws in nature and their geochemical and cosmochemical significance. Geochim Cosmochim Acta 66:1095–1104

Zambardi T, Lundstrom CC, Li X, McCurry M (2014) Fe and Si isotope variations at Cedar Butte volcano; insight into magmatic differentiation. Earth Planet Sci Lett 405:169–179

Zhang R, John SG, Zhang J, Ren, J Wu Y, Zhu Z, Liu S, Zhu X, Marsay CM, Wenger, F (2015) Transport and reaction of iron and iron stable isotopes in glacial meltwaters on Svalbard near Kongsfjorden: From rivers to estuary to ocean. Earth Planet Sci Lett 424:201–211

Zhao X, Zhang H, Zhu X, Tang S, Tang Y (2010) Iron isotope variations in spinel peridotite xenoliths from North China Craton: implications for mantle metasomatism. Contrib Mineral Petrol 160:1–14

Zhao X, Zhang H, Zhu X, Tang S, Yan B (2012) Iron isotope evidence for multistage melt–peridotite interactions in the lithospheric mantle of eastern China. Chem Geol 292:127–139

Zhu XK, O'Nions RK, Guo Y, Reynolds BC (2000) Secular variation of iron isotopes in North Atlantic Deep Water. Science 287:2000–200

Zhu D, Bao H, Liu Y (2015) Non-traditional stable isotope behaviors in immiscible silica-melts in a mafic magma chamber. Sci Rep 5:17561

Zhu B, Zhang, H-F, Zhao, X-M He, Y-S (2016) Iron isotope fractionation during skarn-type alteration: Implications for metal source in the Han-Xing iron skarn deposit. Ore Geol Rev 74:139–150